**Showcasing research from Prof. Yuichi Negishi's laboratory, Tokyo University of Science, Japan.**

Atomically precise metal nanoclusters as catalysts for electrocatalytic CO_2 reduction

Electrochemical carbon dioxide (CO_2) reduction can be used to convert CO_2 into various compounds at room temperature and ambient pressure using electricity generated from renewable energy sources. In recent years, metal nanoclusters, which are metal particles with a size of approximately 1 nm, have been reported to be capable of electrochemical CO_2 reduction with high activity and selectivity. This review summarizes the synthesis methods of atomically precise metal nanoclusters and their application in electrochemical CO_2 reduction.

ROYAL SOCIETY OF CHEMISTRY

rsc.li/greenchem

Check for updates
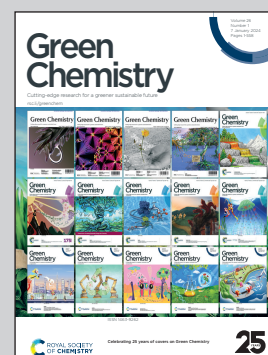
Atomically precise metal nanoclusters as catalysts for electrocatalytic CO_2 reduction

Tokuhisa Kawawaki, [ID] ⋆[a,b] Tomoshige Okada,[a] Daisuke Hirayama[a] and Yuichi Negishi [ID] ⋆[a,b]

Electrochemical carbon dioxide (CO_2) reduction can be used to convert CO_2 into various compounds at room temperature and ambient pressure using electricity generated from renewable energy sources. This technology is indispensable in establishing an environmentally responsible and sustainable society. However, further improvements in the activity and selectivity require the development of electrocatalysts that can directly serve as the actual reaction sites. In recent years, metal nanoclusters, which are metal particles with a size of approximately 1 nm, have been reported to be capable of electrochemical CO_2 reduction with high activity and selectivity, owing to their unique geometric/electronic structure. This review summarizes the synthesis methods of atomically precise metal nanoclusters and their application in electrochemical CO_2 reduction. We expect that this review will help clarify the current status of these studies and further accelerate the research on highly active and selective CO_2 reduction catalysts using metal nanoclusters.

1. Introduction

1.1 Atomically precise metal nanoclusters as catalysts

Among nano-sized materials, an aggregate of metal atoms with a size of approximately 1 nm is called a metal nanocluster (NC).[1–28] Metal NCs have different physical/chemical properties than bulk metals and relatively larger (>5 nm) metal nanoparticles (NPs), which are attributed to quantum size effects (Fig. 1A).[29–31] Furthermore, the properties and functions of NCs show a remarkable dependence on the number of constituent atoms, unlike metal NPs.[32–36] Therefore, if the number of constituent atoms can be precisely controlled in the metal NCs, it is possible to create a wide variety of properties and functions with the difference of a single atom. It has become possible not only to control the size of metal NCs but also to control heterometal doping[37,38] and geometric structures[39–42] at the atomic level. Thus, metal NCs are expected to be applied as key components in next-generation materials. In particular, for metal NCs protected by ligands, unlike gas-phase generated clusters, their geometric structures have been revealed by single-crystal X-ray diffraction (SC-XRD), and the combination of density functional theory (DFT) calculations and SC-XRD can reveal the electronic structure of metal

NCs and their origin. Because of these characteristics, metal NCs have attracted significant attention in the development of materials based on luminescence control[43–47] and chiral control,[48,49] environmental fields,[50–54] energy harvesting,[51,55–59] and biological sensor[45,60,61] and catalytic reactions.[62–64] Metal NCs are highly active catalysts because of their unique geometric/electronic structure and small size. Moreover, theoretical calculations of the adsorption/desorption energies of reacting molecules based on the geometric structure obtained by SC-XRD can help elucidate the mechanisms of various reactions.

The studies on metal NCs began after the 1950s, with efforts to synthesize metal NCs consisting of group 8–10 elements and ligands such as phosphine, halogen (X), and carbon monoxide (CO).[65] In 1994, Brust and Schiffrin *et al.* reported the synthesis of thiolate (SR)-protected gold (Au) NCs ($Au_n(SR)_m$).[66] Because these NCs have extremely high thermal and chemical stability owing to the strong bonding between Au and sulfur (S), and can be synthesized by simply mixing reagents under atmospheric conditions, research on $Au_n(SR)_m$ increased dramatically after 2000. At that time, $Au_n(SR)_m$ could only be treated as a mixture with a distribution in the number of constituent atoms; however, with the establishment of highly resolved separation techniques by Whetten *et al.* and Murray *et al.*, the chemical composition of $Au_n(SR)_m$ could be highly controlled.[67–69] In 2005, Tsukuda and Negishi were the first to systematically separate $Au_n(SR)_m$ with a well-defined chemical composition.[70–72] In 2007, Kornberg *et al.* determined the geometric structure of $Au_{102}(p\text{-MBA})_{44}$ (*p*-MBA:

*a*Department of Applied Chemistry, Faculty of Science, Tokyo University of Science, 1-3 Kagurazaka, Shinjuku-ku, Tokyo 162-8601, Japan.
E-mail: kawawaki@rs.tus.ac.jp, negishi@rs.tus.ac.jp
*b*Research Institute for Science & Technology, Tokyo University of Science, 2641 Yamazaki, Noda, Chiba 278-8510, Japan

4-mercaptobenzoic acid) by SC-XRD,[73] and since then, the chemical compositions and geometric structures have been determined for several $Au_n(SR)_m$. In addition, SR-protected silver (Ag) and copper (Cu) NCs have been synthesized in numerous studies, and the research has been extended to metal NCs capped by other ligands (Fig. 1B).

1.2 Electrochemical carbon dioxide reduction

Recently, interest in carbon dioxide (CO_2) reduction using electrocatalysts has been growing. In 1967, Manabe presented a "coupled atmosphere-ocean model" showing that CO_2 has a significant impact on long-term climate change, which bolstered global efforts to reduce CO_2 emissions.[74] In 2015, the Paris Agreement was adopted to solve the global warming problem, and "achieving carbon neutrality" is now a long-term goal shared among numerous countries.[75] Herein, carbon neutral means the reduction of the total greenhouse gases, including CO_2, to net zero. To achieve this, various efforts are being actively pursued worldwide. In particular, the transformation of CO_2 into useful organic compounds by reduction has been demonstrated as a promising method for directly decreasing CO_2 emissions.[75–77]

The most notable CO_2 reduction reaction (CRR) is the Sabatier reaction (methanation), in which hydrogen (H_2) and CO_2 are converted to methane (CH_4) and water under high temperature and high pressure using a metal catalyst. This method has been used for industrially synthesizing methane since its discovery by Sabatier and Senderens in 1902.[78,79] Additionally, the reverse water gas shift reaction that produces CO and water (H_2O) from CO_2 and H_2 is often used in industry. However, the current system produces H_2 from fossil fuels, such as natural gas reforming or coal gasification, which emit a large amount of CO_2 during the production process. Alternatively, if CO_2 can be directly reduced by electrochemical reduction using water as an electron and proton source and electricity derived from renewable energy sources, then CO_2 can be directly converted into other organic compounds without using H_2 derived from fossil fuels (Fig. 1C). Electrochemical CRR is becoming easier to industrialize because it is possible to divert the water-electrolysis hydrogen-production technology currently under development.[75,80]

Research on electrochemical CRRs began in the 1950s.[81] In 1985, Hori *et al.* quantitatively analyzed the amount of liquid- and gas-phase products produced by electrolytic reduction, which corresponded to the amount of applied electricity (*i.e.*, performed with a Faraday efficiency (FE) of 100%).[82] Furthermore, their study revealed that the products differed depending on the metal electrodes:[83–86] (1) nickel (Ni), iron (Fe), platinum (Pt), and titanium (Ti) produce H_2; (2) lead (Pb), mercury (Hg), thallium (Tl), indium (In), tin (Sn), cadmium (Cd), and bismuth (Bi) primarily produce formic acid (HCOOH); (3) Au, Ag, zinc (Zn), palladium (Pd), and gallium (Ga) mainly produce CO; and (4) Cu produces various hydrocarbons, aldehydes, and alcohols. For these metal catalysts, increases in specific surface area, crystal facet control, alloying, and support interactions for CRR catalysts have been investigated, along with advances in nanotechnology, since the 2000s.[87–89] Thereby, overvoltage suppression and improvements in product selectivity and durability have been achieved. However, further improvements in the activity, selectivity, and durability are required, and research in this area remains active. In this review, we discuss the use of atomically precise metal NCs for electrochemical CRRs. Therefore, readers interested in studying electrochemical CRRs using nanomaterials other than metal NCs (metal NPs,[89–92] single atoms,[93–97] and molecular catalysts[98–100]) are invited to read the review articles that describe them in detail. Gas-phase generated clusters are excluded from this review because there are few reports on CO_2 reduction.

Tokuhisa Kawawaki

Tokuhisa Kawawaki is a Junior Associate Professor in the Department of Applied Chemistry at Tokyo University of Science. He received his Ph.D. degree in applied chemistry from the University of Tokyo in 2015. In 2016, he worked as a Japan Society for the Promotion of Science (JSPS) postdoctoral fellow at the University of Melbourne. He then worked as a JSPS super postdoctoral fellow at Kyoto University. In 2019, he moved to his current University. His current research topics include the synthesis of ligand-protected metal nanoparticles and nanoclusters and their application in photoelectrochemistry and photocatalysis.

Tomoshige Okada

Tomoshige Okada is a masters student in the Negishi group at Tokyo University of Science. He received his B.Sc. degree in chemistry from Tokyo University of Science in 2022. His main research interest is on the development of high-performance water-splitting electrocatalysts by using atomically precise metal clusters.

1.3 Purpose and contents of this review

Metal NCs have significant potential not only for use as various thermal catalysts[51,52,54,101] and photocatalysts[102–114] but also as electrocatalysts,[101,115–117] particularly in hydrogen evolution reactions (HER),[118–123] oxygen evolution reactions (OER),[120,124–126] oxygen reduction reactions (ORR),[58,120,127–134] and alcohol and HCOOH oxidation reactions.[135–137] In addition, the application of metal NCs as electrochemical CRR catalysts[1,55,57,113–115,138–150] has been widely studied. However, CRR activity is often evaluated on accidentally synthesized metal NCs, and there are not many examples of metal NCs synthesized based on standard design principles. The reason for this is the lack of deep understanding regarding the synthetic methods and geometric/electronic structures of metal NCs and their resulting correlation with CRR activity. In this review, we summarize the synthesis methods and geometric/electronic structures of metal NCs, and the representative studies on electrochemical CRRs using these materials. Furthermore, on the basis of this knowledge, we discuss (1) the synthesis and geometric/electronic structure of metal NCs as high-performance CRR catalysts, (2) the appropriate experimental conditions (*e.g.*, support and metal NCs) for the application of high-performance CRR catalysts, and (3) the CRR mechanism of the metal NC catalysts. Through these discussions, we hope to promote the establishment of clear guidelines for the design of metal NCs that are suitable for electrochemical CRRs, thereby enhancing the development of metal NCs and electrochemical CRR catalysis.

In section 2, we first describe the synthesis methods and geometric/electronic structures of the predominant metal NCs that have been applied to CO_2 reduction in previous studies, categorized by the metal species. Then, in section 3, we discuss the catalytic activities of metal NCs in electrochemical CRRs and their mechanisms. In section 4, we summarize the conclusions of this review, and in section 5, we briefly describe the outlook for the future.

2. Synthesis of atomically precise metal nanoclusters

Metal NCs have high surface energy owing to their small size and can easily aggregate or degrade in air if not specially handled. Thus, metal NCs are often protected using organic ligands, which facilitates handling and modification. Furthermore, by controlling the ligands, metal species, and reaction rates, metal NCs with various numbers of constituent atoms, chemical compositions, and structures can be synthesized. In this section, we describe the synthesis of mainly Au, Ag, and Cu NCs, among those applied to electrochemical CRRs, which have relatively high stability and can be synthesized with atomic precision, as well as the effects of ligands and alloying. Multiple reviews have focused on the synthesis of metal NCs, and thus readers who would like to know more details should refer to those articles.[32–36]

2.1 Synthesis of gold nanocluster

$Au_n(SR)_m$ have relatively high stability and more examples have been reported at an early stage, compared with SR-protected Ag and Cu NCs.[68,71,151,152] $Au_n(SR)_m$ also possess useful physicochemical properties such as photoexcited luminescence, thermocatalysis, electrocatalysis, and magnetism, and many studies have reported on their application in electrochemical CRRs. In this section, we describe the synthesis of Au NCs, particularly those protected by SR, phosphine, alkynyl (C≡CR), and N-heterocyclic carbene (NHC).

2.1.1 Thiolate-protected gold 25 nanoclusters. Among $Au_n(SR)_m$, one of the most widely studied is $Au_{25}(PET)_{18}$ (PET = 2-phenylethanethiolate). There are two common synthetic methods: (i) two-phase synthesis and (ii) *in situ* single-phase synthesis.[153] In the two-phase synthesis, tetrachloroauric(III) acid (HAuCl$_4$·3H$_2$O) dissolved in water is mixed with tetraoctylammonium bromide (TOAB) dissolved in toluene to induce a phase transition, and then cooled to 0 °C and 2-phenylethanethiol is added while slowly stirring to reduce Au(III) to Au(I).
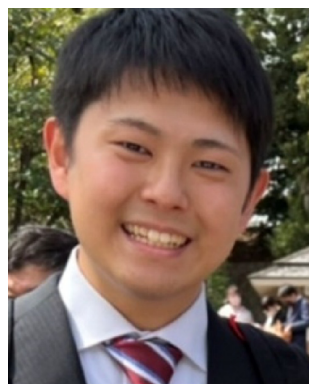
Daisuke Hirayama is a masters student in the Negishi group at Tokyo University of Science. He received his B.Sc. degree in chemistry from Tokyo University of Science in 2022. His main research interest is on the development of high-performance water-splitting photocatalysts by using atomically precise metal clusters as cocatalysts.

Daisuke Hirayama

Yuichi Negishi is a professor at the Department of Applied Chemistry at TUS. He received his Ph.D. degree in chemistry (2001) from Keio University under the supervision of Prof. Atsushi Nakajima. Before joining TUS in 2008, he was employed as an assistant professor at Keio University and the Institute for Molecular Science. His current research interests include the precise synthesis of stable and functionalized metal nano-

Yuichi Negishi

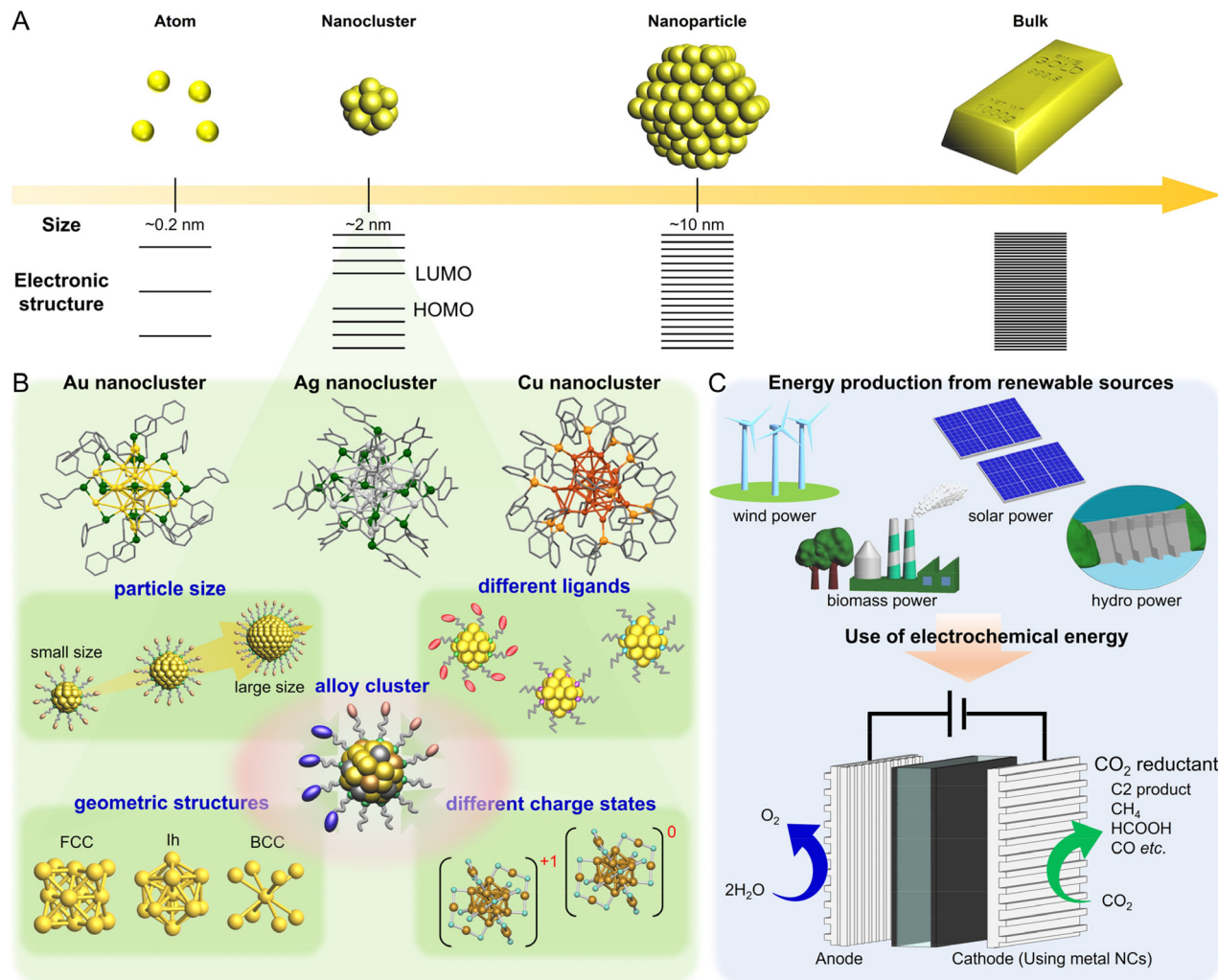*clusters, metal nanocluster-connected structures, and covalent organic frameworks.*

Fig. 1 Schematic of this review. A next-generation energy system based on electrocatalytic CO_2 reduction reaction using metal-cluster catalysts. (A) Size dependences of metals for electronic structure; (B) kinds of metal clusters and each parameter for electrocatalytic CO_2 reduction reaction; and (C) a flow reaction system for electrocatalytic CO_2 reduction using electricity from renewable energy source.

Next, sodium borohydride ($NaBH_4$) is added, and $Au_{25}(PET)_{18}$ is obtained by washing/separation.[154] For the *in situ* single-phase synthesis, $HAuCl_4 \cdot 3H_2O$ and TOAB are dissolved in tetrahydrofuran (THF) and 2-phenylethanethiol, $NaBH_4$ is added, and $Au_{25}(PET)_{18}$ is obtained by washing/separation.[155] These methods can produce $Au_{25}(PET)_{18}$ in relatively high yields. The highly stable $Au_{25}(PET)_{18}$ is essentially $Au_n(SR)_m$ with an entire −1 valence of ionic charge ($[Au_{25}(PET)_{18}]^-$). However, it is also possible to synthesize neutral or +1 valent $Au_{25}(PET)_{18}$ with the same chemical composition ($[Au_{25}(PET)_{18}]^0$ and $[Au_{25}(PET)_{18}]^+$, respectively).[156,157] Notably, there are some differences in their geometric structures. The basic $Au_{25}(PET)_{18}$ structure consists of an icosahedral Au 13 core surrounded by six SR–Au–SR–Au–SR staples with quasi-octahedral symmetry (Au–S staples) protecting the structure (Fig. 2A).[158,159] The Au–S staple structure is distorted with regard to the σ_h symmetry plane in $[Au_{25}(PET)_{18}]^-$, whereas the staples are aligned with the σ_h symmetry plane in

$[Au_{25}(PET)_{18}]^0$ (Fig. 2B). This might be caused by the presence or absence of counter ions and might be one of the reasons why metal NCs exhibit different properties depending on their valence, even if they have the same chemical composition. In addition, there are differences in the electronic structures of $[Au_{25}(PET)_{18}]^z$ ($z = −1, 0, +1$) (Fig. 2C). $[Au_{25}(PET)_{18}]^-$ is an 8-electron system corresponding to a noble gas-like $1S^2 1P^6$ superatomic electron configuration, whereas $[Au_{25}(PET)_{18}]^0$ and $[Au_{25}(PET)_{18}]^+$ have $1S^2 1P^5$ and $1S^2 1P^4$ electron configurations, respectively. This significantly affects their optical absorption spectra.[157,160,161]

Owing to its relatively stable electronic/geometric structure, $Au_{25}(SR)_{18}$ can be synthesized with a variety of SR ligands (including hydrophilic SR ligands). For example, in 2016, Li and Jin *et al.* synthesized 1-naphthalenethiolate (SNap)-protected $Au_{25}(SNap)_{18}$ using a two-step method. First, they synthesized hexanethiolate (SC_6H_{13})-protected $Au_{25}(SC_6H_{13})_{18}$, then dissolved it in toluene and reacted with naphthalene

thiol to synthesize $Au_{25}(SNap)_{18}$.[162] For the structure of $Au_{25}(SNap)_{18}$, the SC-XRD results revealed that $Au_2(SNap)_3$ is coordinated as a staple around an icosahedral Au_{13} core.
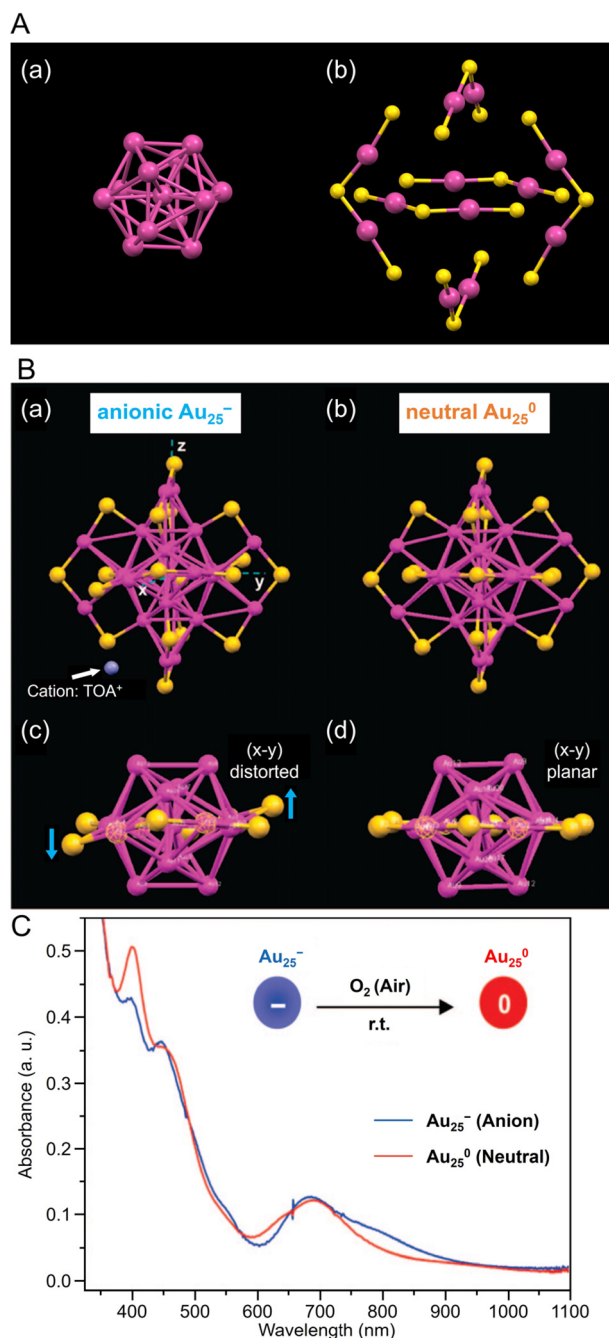
Many studies have attempted to alloy $Au_{25}(SR)_{18}$ because of its high stability.[163] As a result, many metals, such as Ag,[164–167] Cu,[168–173] Pt,[174–177] Pd,[175,178–181] Hg,[182,183] Cd,[183–185] and Ir,[186] can be doped into $Au_{25}(SR)_{18}$. In 2015, Jiang and Lee *et al.* reported the synthesis of $MAu_{24}(SC_6H_{13})_{18}$ (M = Pd or Pt) using $HAuCl_4 \cdot 3H_2O$ and hydrogen hexachloroplatinate(IV) ($H_2PtCl_6 \cdot 6H_2O$) or $Na_2PdCl_4 \cdot 6H_2O$ as precursors, and their electronic structures were elucidated (Fig. 3Aa).[187] $[MAu_{24}(SC_6H_{13})_{18}]^0$ has a 6-electron superatomic configuration ($1S^21P^4$), whereas $[MAu_{24}(SC_6H_{13})_{18}]^{2-}$ has an 8-electron

Fig. 2 (A) (a) Au_{13} core and (b) Au−S staple structure of $[Au_{25}(PET)_{18}]^-$. (B) Comparison of the crystal structures of (a, c) $[Au_{25}(PET)_{18}]^-$ and (b, d) $[Au_{25}(PET)_{18}]^0$. Both $Au_{25}(PET)_{18}$ in (A) and (B) are capped by 18 PET ligands (for clarity C and H atoms are omitted); for $[Au_{25}(PET)_{18}]^-$, the counterion is tetraoctylammonium (TOA^+; only N (in blue) is shown for clarity). (C) The optical absorption spectra of $[Au_{25}(PET)_{18}]^-$ (blue profile) and $[Au_{25}(PET)_{18}]^0$ (red profile) in solution. (B) and (C) are reproduced with permission from ref. 156. Copyright 2008 American Chemical Society.
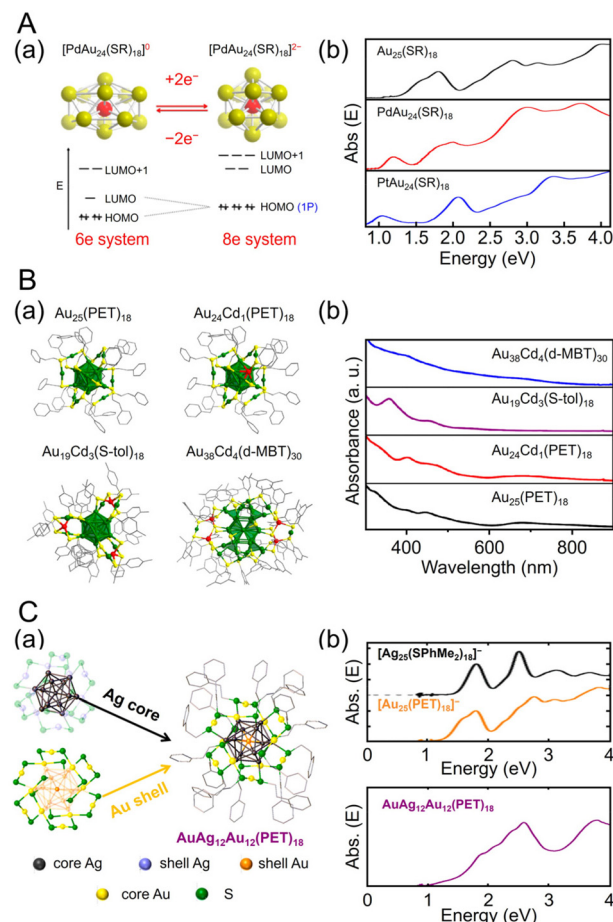

Fig. 3 (A) (a) Cartoon depicting Jahn−Teller-like distortion in the core (*e.g.*, $PdAu_{12}$) predicted for the 6-electron $[PdAu_{24}(SR)_{18}]^0$ (left), which undergoes a structural change to nearly spherical 8-electron $[PdAu_{24}(SR)_{18}]^{2-}$ upon reduction (right). The vertical compression for $[PdAu_{24}(SR)_{18}]^0$ (left) is exaggerated. (b) UV/Vis/NIR absorption spectra of $Au_{25}(SC_6H_{13})_{18}$ (black), $PdAu_{24}(SC_6H_{13})_{18}$ (red), and $PtAu_{24}(SC_6H_{13})_{18}$ (blue) in trichloroethylene. (B) (a) Total crystal structures and (b) UV/Vis absorption spectra of $Au_{25}(PET)_{18}$, $Au_{24}Cd_1(PET)_{18}$, $Au_{19}Cd_3(S\text{-tol})_{18}$, and $Au_{38}Cd_4(d\text{-MBT})_{30}$. Au, green; Cd, red; S, yellow; C, gray. H atoms are omitted for clarity. (C) (a) Schematic of active-site engineering and crystal structure of the $[Ag_xAu_{25-x}(PET)_{18}]^-$. (b) UV/vis absorption spectra of the $[Ag_{25}(SPhMe_2)_{18}]^-$, $[Au_{25}(PET)_{18}]^-$ and $[Ag_xAu_{25-x}(PET)_{18}]^-$ (x = 10−15) in dichloromethane. (A) is reproduced with permission from ref. 187. Copyright 2015 American Chemical Society. (B) is reproduced with permission from ref. 188. Copyright 2021 American Chemical Society. (C) is reproduced with permission from ref. 190. Copyright 2022 American Chemical Society.

superatomic configuration ($1S^2 1P^6$), which is similar to the trend observed in $[Au_{25}(PET)_{18}]^z$ ($z = -1, 0, +1$). Furthermore, the Jahn–Teller-like distortion of $[MAu_{24}(SC_6H_{13})_{18}]^0$ results in 1P orbital splitting, which causes strong absorption in the near-infrared region (Fig. 3Ab). These results agree well with the predicted optical absorption spectra from simulations.

Especially among $Au_n(SR)_m$ applied in CRRs, Cd doping supports high activation. In this case, $[Au_{25}(PET)_{18}]^-$ is dissolved in CH_3CN, and $Cd(NO_3)_2$ is added and stirred/extracted to synthesize $Au_{24}Cd_1(PET)_{18}$ in which one Au atom is replaced by a Cd atom (Fig. 3Ba). Significant differences can be observed in the electronic structure after doping (Fig. 3Bb). In addition, by dissolving $Au_{24}Cd_1(PET)_{18}$ in toluene as a precursor, mixing it with different SR ligands, and adding methanol and stirring, a ligand exchange reaction can be used to synthesize $Au_{24}Cd_1(TBBT)_{18}$ (TBBT = 4-*tert*-butylbenzenethiolate) and $Au_{24}Cd_1(d\text{-}MBT)_{18}$ (d-MBT = 3,5-dimethylbenzenthiolate) from $Au_{24}Cd_1(PET)_{18}$.[188] Similarly, Cd-doped $Au_n(SR)_m$, such as $Au_{19}Cd_3(S\text{-}tol)_{18}$ and $Au_{38}Cd_4(d\text{-}MBT)_{30}$ (S-tol = *p*-toluenethiolate), can be synthesized using $Au_{25}(PET)_{18}$ and $Au_{44}(d\text{-}MBT)_{28}$ as precursors, respectively.[188] In the case of $Au_{24}Cd_1(PET)_{18}$, Cd atoms are substituted for Au atoms on the surface of the Au_{13} core, but for $Au_{19}Cd_3(S\text{-}tol)_{18}$ and $Au_{38}Cd_4(d\text{-}MBT)_{30}$, Cd atoms are substituted at the outer staples of the Au_{13} and Au_{26} cores, respectively (Fig. 3Ba). These differences can significantly alter the electronic structure (Fig. 3Bb).

Ag can be doped into $[Au_{25}(SR)_{18}]^-$ with a relatively large number of substitutions.[165,166,170,189] In 2022, Kim, Yoo, and Lee *et al.*, synthesized $[Au_xAg_{12-x}@Au_{12}(PET)_{18}]^-$ ($x = 10$–15) with an $Au_{12}(PET)_{18}$ shell (Fig. 3Ca).[190] In this synthesis, they referred to the previously reported synthesis of $[Ag_{25}(SPhMe_2)_{18}]^-$ ($SPhMe_2$ = 2,4-dimethylbenzenethiolate)[191] and alloyed $[Au_{25}(PET)_{18}]^-$ by introducing silver acetate (CH_3COOAg) during the process. In $[Au_xAg_{12-x}@Au_{12}(PET)_{18}]^-$, absorption peaks were observed at 1.9, 2.6, and 3.8 eV (Fig. 3Cb), and SC-XRD revealed that the $AuAg_{12}$ core was covered by an $Au_{12}(PET)_{18}$ shell (Fig. 3Ca).

2.1.2 Thiolate-protected gold 38 nanoclusters. $Au_{38}(PET)_{24}$ is another $Au_n(SR)_m$ with many reported cases,[192] and the structural isomers Au_{38Q}[193,194] and Au_{38T}[195] can be synthesized (Fig. 4Aa). Au_{38T} is relatively unstable and converts to Au_{38Q}, a more stable structure, by heating to approximately 50 °C. Au_{38Q} is composed of two icosahedral Au_{13} cores connected by sharing an Au_3 face, and its electronic structure differs significantly from that of Au_{38T} (Fig. 4Ab). The protected shell of Au_{38Q} consists of the remaining 15 Au atoms and contains six $Au_2(SR)_3$ and three $Au(SR)_2$ staples. Furthermore, Au_{38Q} has a pair of enantiomers, also known as $Au_n(SR)_m$ with chirality.[196–198] In 2022, Zhou, Gao, and Zhu *et al.* synthesized $[Au_{38}(SCH_2Ph^tBu)_{24}]^0$ (SCH_2Ph^tBu = 4-*tert*-butylbenzylthiolate) using the ligand exchange method, in which 4-*tert*-butylbenzylthiol is added to Au_{38Q} and stirred.[199] They also synthesized $Au_{38}(SCH_2Ph^tBu)_{24}$ doped with Pt and Pd. In this synthesis, $HAuCl_4 \cdot 4H_2O$ and $H_2PtCl_6 \cdot 6H_2O$ are mixed in THF, and then TOAB is added and stirred. Next, they added 4-*tert*-butylbenzylthiol and $NaBH_4$ and reacted for 6 h.
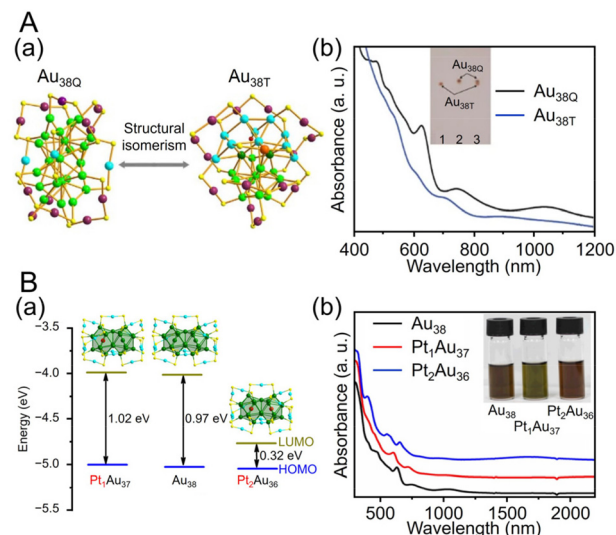

Fig. 4 (A) (a) Crystal structures and (b) UV/Vis/NIR absorption spectra of Au_{38T} (blue) and Au_{38Q} (black) in toluene (measurement temperature: 0 °C). (B) (a) Crystal structures and energy band diagrams, and (b) UV/Vis/NIR spectra of $[Au_{38}(SCH_2Ph^tBu)_{24}]^0$, $[Pt_1Au_{37}(SCH_2Ph^tBu)_{24}]^0$ and $[Pt_2Au_{36}(SCH_2Ph^tBu)_{24}]^0$. The inset is the picture of the three clusters in $CHCl_3$. (A) is reproduced with permission from ref. 195. Copyright 2015 Springer Nature. (B) is reproduced with permission from ref. 199. Copyright 2022 Wiley-VCH GmbH.

After washing and separation, $[Pt_2Au_{36}(SCH_2Ph^tBu)_{24}]^0$ and $[Pt_1Au_{37}(SCH_2Ph^tBu)_{24}]^0$ were obtained (Fig. 4Ba). Although $[Au_{38}(SR)_{24}]^0$ and $[Pt_2Au_{36}(SR)_{24}]^0$ have closed-shell electron configurations with 14- and 12-electron superatomic configurations, respectively,[200,201] $[Pt_1Au_{37}(SCH_2Ph^tBu)_{24}]^0$ has a 13-electron configuration, and electron spin resonance measurements indicate that only $[Pt_1Au_{37}(SCH_2Ph^tBu)_{24}]^0$ is magnetic. The optical peaks are blue-shifted with increasing Pt doping, compared with $[Au_{38}(SCH_2Ph^tBu)_{24}]^0$ (Fig. 4Bb).

2.1.3 Other thiolate-protected gold nanoclusters. In 2022, Yang, Yang, and Wu *et al.* successfully synthesized TBBT-protected Au–Pd alloy and Au–Ag–Pd trimetallic alloy NCs.[202] First, they dissolved TOAB in THF and then added $HAuCl_4 \cdot 4H_2O$ palladium acetate ($Pd(CH_3COO)_2$) and TBBT, and stirred. After that, they added $NaBH_4$, followed by washing and separation to obtain $Au_4Pd_6(TBBT)_{12}$. Additionally, they dissolved $Au_4Pd_6(TBBT)_{12}$ in dichloromethane, added silver nitrate ($AgNO_3$) dissolved in acetonitrile, stirred for 1 h, and performed separation to obtain $Au_3AgPd_6(TBBT)_{12}$. SC-XRD revealed that $Au_4Pd_6(TBBT)_{12}$ has a pair of enantiomers (Fig. 5A). The structure has an outer shell consisting of two $Pd_3(TBBT)_3$ and three $Au(TBBT)_2$ and a core framework with one Au atom in the center, indicating that a difference of one atom can result in distinct electronic structures (Fig. 5B).

Many studies have reported on $Au_n(SR)_m$ of different sizes, whose crystal structures are also known. For example, $Au_{18}(SR)_{14}$,[203] $Au_{20}(TBBT)_{16}$,[204] $Au_{21}(S^tBu)_{15}$,[205] $[Au_{23}(SC_6H_{11})_{16}]^-$ (SC_6H_{11} = cyclohexanethiolate),[206] $Au_{24}(TBBT)_{20}$,[207] $Au_{28}(TBBT)_{20}$,[208] $Au_{30}S(S^tBu)_{18}$,[209] $Au_{36}(SR)_{24}$,[210] $Au_{44}(TBBT)_{28}$,[211] $Au_{52}(TBBT)_{32}$,[212] $Au_{92}(TBBT)_{44}$,[213] $Au_{130}(p\text{-}MBT)_{50}$ (*p*-MBT =

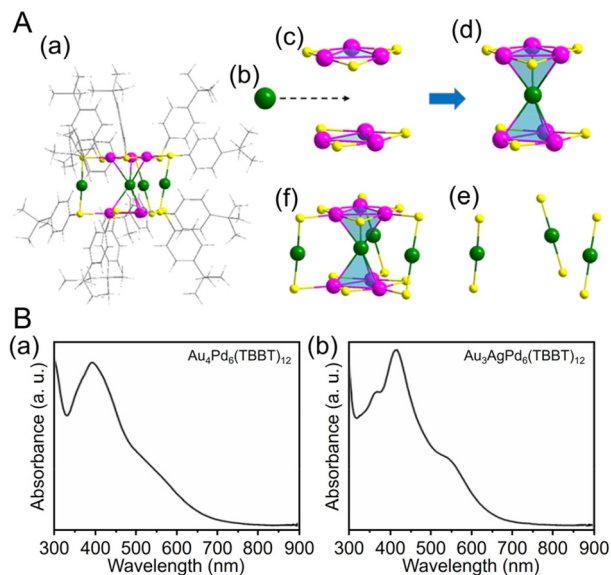**Fig. 5** (A) (a) Total structure of the $Au_4Pd_6(TBBT)_{12}$. (b) One Au kernel of Au_4Pd_6. (c) Two $Pd_3(TBBT)_3$ staple motifs. (d) $AuPd_6(TBBT)_6$. (e) Three Au $(TBBT)_2$ staple motifs. (f) $Au_4Pd_6(TBBT)_{12}$ (green, Au; purple, Pd; yellow, S; gray, C; white, H). (B) Experimental UV/Vis/NIR spectra of (a) $Au_4Pd_6(TBBT)_{12}$ and (b) $Au_3AgPd_6(TBBT)_{12}$. (A) and (B) are reproduced with permission from ref. 202. Copyright 2022 American Chemical Society.
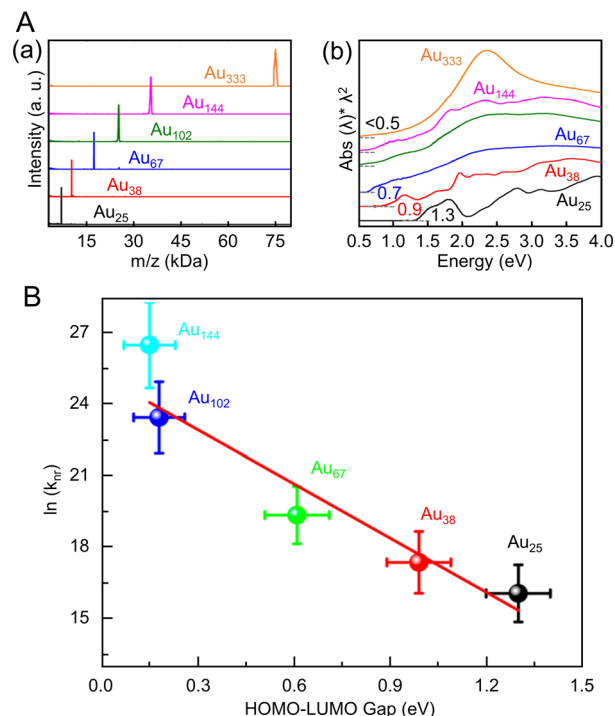

Fig. 6 (A) (a) MALDI mass spectra and (b) UV/Vis/NIR absorption spectra of Au_{25}, Au_{38}, Au_{67}, Au_{102}, Au_{144}, and Au_{333} clusters. The absorption spectra of clusters were obtained in tetrachloroethylene and were offset for clarity. (B) Plot of $\ln(k_{nr})$ versus HOMO–LUMO gap for $Au_n(SR)_m$. The solid line is the best fit straight line for data (Au_{25}–Au_{144}). (A) and (B) are reproduced with permission from ref. 217. Copyright 2017 American Chemical Society.

4-methylbenzenethiolate),[214] and $Au_{144}(SR)_{60}$ [215,216] have been reported, as well as many other $Au_n(SR)_m$. Notably, their systematic syntheses and size dependence have also been investigated.[32–36] In 2017, Ramakrishna and Lee *et al.* used SC_6H_{13} as a ligand to synthesize $Au_{25}(SC_6H_{13})_{18}$, $Au_{38}(SC_6H_{13})_{24}$, $Au_{67}(SC_6H_{13})_{35}$, $Au_{102}(SC_6H_{13})_{44}$, $Au_{144}(SC_6H_{13})_{60}$, and $Au_{333}(SC_6H_{13})_{79}$.[217] Their chemical compositions were confirmed by matrix-assisted laser desorption/ionization mass spectrometry (MALDI-MS) (Fig. 6Aa). Furthermore, these $Au_n(SR)_m$ exhibit size-dependent optical properties (Fig. 6Ab), and the optical gap of the electronic transitions decreases as the cluster size increases (Fig. 6B).

2.1.4 Phosphine-protected gold nanoclusters. In addition to the SR ligands described above, a number of phosphine-protected Au NCs have been reported.[218–222] From the late 1960s to 1980s, Malatesta *et al.*,[223] the groups at Nijimegen,[224–226] and Mingos *et al.*[227–229] synthesized phosphine-protected Au NCs and determined their geometric structures. In general, these phosphine-protected Au NCs can be synthesized by adding a reducing agent, such as $NaBH_4$, to a phosphine-gold complex dispersed in a solvent, such as dichloromethane or ethanol. In some cases, washing operations have been conducted through an etching/growth process using hydrochloric acid or other chemicals.[230] For example, in 2022, Jiang, Sun, and Wang *et al.* synthesized $Au_{11}(DPPE)_5$ (DPPE = 1,2-bis (diphenylphosphino)ethane) and $Au_{22}H_3(DPPE)_3(PPh_3)_8$ (PPh_3 = triphenylphosphine) by liquid-phase synthesis, and other phosphine-protected Au NCs.[231] In 2023, Pei and Wang *et al.* synthesized $[Au_7(PPh_3)_7H_5]^{2+}$ using a one-pot synthesis

method.[232] For this synthesis, they first added PPh_3 and cyclo-hexanethiol to a $HAuCl_4·3H_2O$ solution and stirred. After that, $NaBH_4$ was added, and the mixture was stirred for 14 h and then washed and separated to obtain $[Au_7(PPh_3)_7H_5]^{2+}$. For $[Au_7(PPh_3)_7H_5]^{2+}$, the corresponding peaks decayed after 12 minutes of irradiation with 408 nm light, and peaks at 370 and 460 nm from Ultraviolet–visible-near-infrared (UV/Vis/ NIR) spectroscopy appeared. Electrospray ionization-MS (ESI-MS) results indicated that this final product was $[Au_8(PPh_3)_7]^{2+}$, which changes its structure under light irradiation. In 2021, Wang *et al.* reported the synthesis of phosphine and SR co-protected $[Au_{55}(p\text{-}MBT)_{24}(PPh_3)_6]^{3+}$.[233] For this synthesis, gold thiolate and gold phosphine compounds, which are halide-free Au precursors, were prepared first, followed by reduction with $NaBH_4$. SC-XRD revealed that these Au NCs have a face-centered cubic (fcc) structure and an Au_{55} core with four layers stacked on top of each other, and the [111] planes are exposed, especially in the lateral direction (Fig. 7).

2.1.5 Other ligand-protected gold nanoclusters. In addition to these ligands, Au NCs protected by $C\equiv CR$,[23,234–236] NHC,[237–241] and nitrogen donor ligands[242] have been reported in recent years. In 2016, Wang and Zheng *et al.* synthesized $Au_{34}Ag_{28}(C\equiv CPh)_{34}$ by adding silver acetate (CH_3COOAg) and *tert*-butylamineborane complexes to a solution containing Au
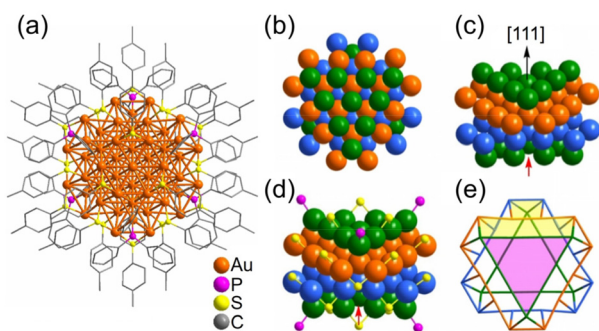
Fig. 7 (a) Anisotropic growth of the Au fcc lattice into a triangle prism in $[Au_{55}(p\text{-}MBT)_{24}(PPh_3)_6]^{3+}$. The Au atom packing of four layers (green, orange, light blue and green) stacked along the [111] direction in an A–B–C–A manner. (b) Top view; (c) side view; (d) the ligand binding positions; (e) simplified facets (Au green/orange/light-blue, S yellow, P pink). Note: the red arrow refers to the missing Au atom in the real Au_{55} cluster. These figures are reproduced with permission from ref. 233. Copyright 2021 Wiley-VCH GmbH.

precursors and phenylacetylene (HC≡CPh) while stirring. The NCs function as highly active catalysts for the hydrolytic oxidation of triethylsilanes by removing the ligands more readily at relatively low temperatures than the previously reported $Au_n(SR)_m$.[243] In 2021, Pei and Tang *et al.* synthesized an alloy cluster of Ag and Cu, $[Ag_9Cu_6(C_6H_9)_{12}]^+$, and an alloy cluster of Au and Ag, $[Au_7Ag_8(C≡C^tBu)_{12}]^+$ (HC≡C^{t}Bu = *tert*-butylacetylene), using antigalvanic reactions.[244] These two alloy clusters have body-centered cubic (bcc) structures and exhibit different optical properties (Fig. 8Aa). The differences in optical properties were attributed to slightly different structures of the M_1 kernel (M = Ag or Au), M_6 octahedron (M = Cu or Au), and Ag_8 cube. Subsequently, in 2022, Q. Tang and Z. Tang *et al.* synthesized $[Au_2Ag_8Cu_5(C≡C^tBu)_{12}]^+$, an alloy cluster composed of Au, Ag, and Cu, by adding chlorodimethylsulfide gold(I) ($(CH_3)_2SAuCl$) as an Au precursor to $[Ag_9Cu_6(C_6H_9)_{12}]^+$.[245] Although many reports have focused on the synthesis of alloy NCs,[38] $[Au_2Ag_8Cu_5(C≡C^tBu)_{12}]^+$ is the first report of a trimetal NC protected with only a C≡CR ligand. The optical absorption spectrum of $[Au_2Ag_8Cu_5(C≡C^tBu)_{12}]^+$ reveals a completely
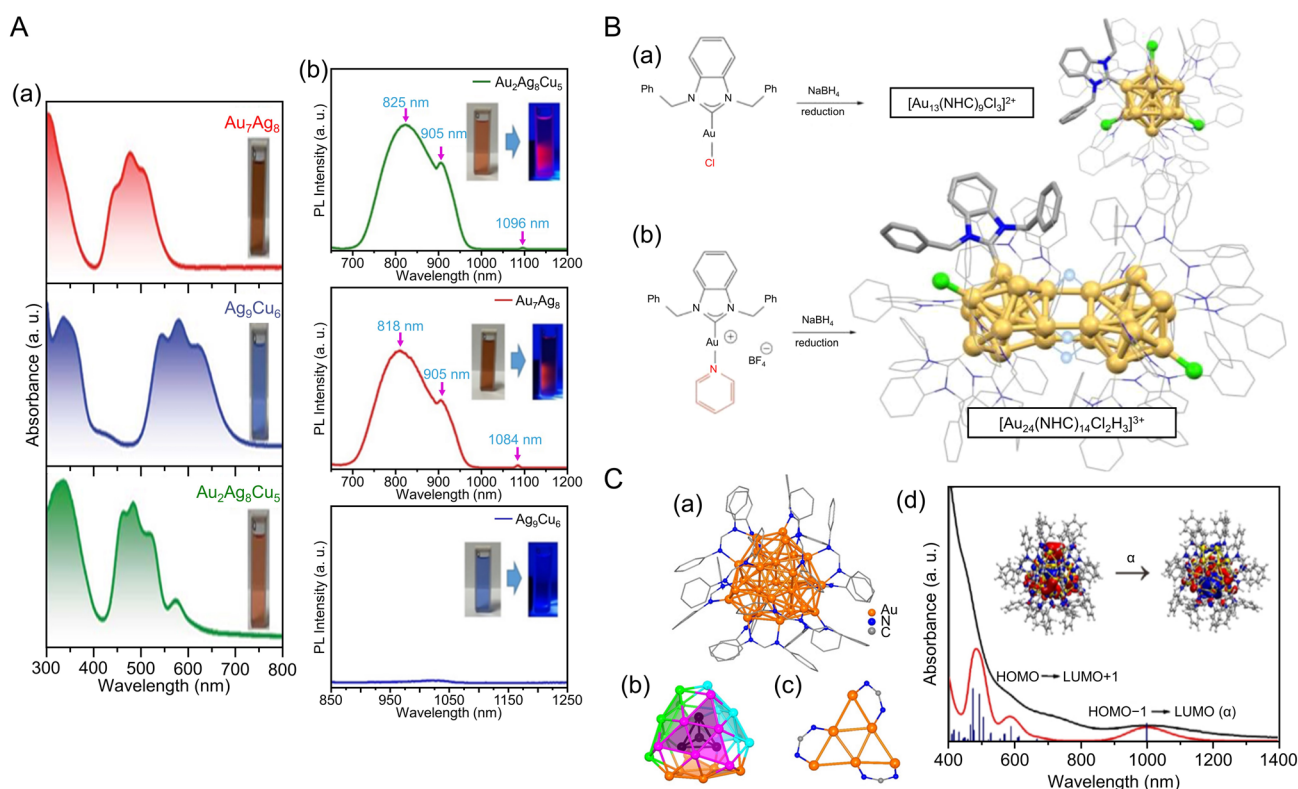
Fig. 8 (A) (a)Absorbance spectra of $[Au_7Ag_8(C≡C^tBu)_{12}]^+$, $[Ag_9Cu_6(C_6H_9)_{12}]^+$ and $[Au_2Ag_8Cu_5(C≡C^tBu)_{12}]^+$. (b) The emission spectra of $[Au_7Ag_8(C≡C^tBu)_{12}]^+$ (λ_{ex} = 482 nm), $[Ag_9Cu_6(C_6H_9)_{12}]^+$ (λ_{ex} = 580 nm) and $[Au_2Ag_8Cu_5(C≡C^tBu)_{12}]^+$ (λ_{ex} = 490 nm) in dichloromethane. Inset: photographs of the three NCs in dichloromethane under room light (left) and 365 nm UV-light (right), respectively. (B) Production of different NHC-stabilized Au clusters depending on the ancillary ligand (halide or pyridine). (a) Use of halide ligands gives typical Au_{13} clusters ($[Au_{13}(NHC)_9Cl_3]^{2+}$), while (b) labile ancillary ligand leads to hydride bridged Au_{24} clusters ($[Au_{24}(NHC)_{14}Cl_2H_3]^{3+}$). (C) (a) The overall structure of $[Au_{28}(Ph\text{-}form)_{12}]^{2+}$. (b) The T symmetrical Au_{28} kernel with concentric tetrahedral Au_4 core (black) and truncated tetrahedron Au_{24} shell divided into four {111} faces. (c) The bridge mode of formamidinate ligands; all Ph rings are omitted for clarity. (d) The experimental (black) and simulated (red) absorption spectra of Au_{28}. (Inset) The NTO picture of the first absorption peak. (A) is reproduced with permission from ref. 245. Copyright 2022 Royal Society of Chemistry. (B) is reproduced with permission from ref. 249. Copyright 2022 American Chemical Society. (C) is reproduced with permission from ref. 250. Copyright 2021 Wiley-VCH GmbH.

different electronic structure compared with those previously described for $[Ag_9Cu_6(C_6H_9)_{12}]^+$ and $[Au_7Ag_8(C{\equiv}C^tBu)_{12}]^+$ (Fig. 8A). Photoluminescence measurements showed that $[Au_2Ag_8Cu_5(C{\equiv}C^tBu)_{12}]^+$ has stronger emission than the other two NCs in the near-infrared region (Fig. 8Ab). $[Au_2Ag_8Cu_5(C{\equiv}C^tBu)_{12}]^+$ also consists of an M@M$_8$@M$_6$ metal core, similar to the other two NCs, but each NC exhibits different CRR selectivity (see section 3).

Au NCs using NHC as a ligand are generally synthesized by the reduction of precursors, such as NHC–Au(I)–X complexes (X = Cl, Br),[246,247] using NaBH$_4$. In 2022, Dinh, Tsukuda, Häkkinen, and Crudden et al. dissolved the [NHC–Au–Pyr]$^+$ complex (Pry = pyridine)[248] in toluene, added NaBH$_4$, stirred the mixture, separated the products, and then purified them by chromatography to obtain $[Au_{24}(NHC)_{14}Cl_2H_3]^{3+}$ (Fig. 8B).[249] $[Au_{24}(NHC)_{14}Cl_2H_3]^{3+}$ consists of two icosahedral Au$_{12}$ cores with distorted structures and three bridging hydride ligands, and the hydride ligands are coordinated to the Au$_{13}$ core, which has been confirmed by SC-XRD, ESI-MS, and nuclear magnetic resonance (NMR) spectroscopy.

Studies have also reported on amidinate-protected Au NCs. In 2021, Wang et al. mixed $(CH_3)_2SAuCl$, N,N′-diphenylformamidinate (Ph-form), and sodium trifluoromethanesulfonate (NaOTf) in chloroform, stirred, and then added sodium methanolate (MeONa). Next, they synthesized $[Au_{28}(Ph-form)_{12}]^{2+}$ by adding NaBH$_4$ and vigorously stirring the mixture under various temperature conditions.[250] The $[Au_{28}(Ph-form)_{12}]^{2+}$ exhibited high stability owing to its superatomic configuration of $1S^21P^62S^21D^4$, and theoretical calculations reproduced the measured electronic structure (Fig. 8C).

As mentioned above, numerous synthetic examples of Au NCs protected by organic ligands, such as SR, phosphine, C≡CR, and NHC, have been reported. Moreover, many of the Au NCs described in this section have been applied in electrochemical CRRs, which are described in detail in section 3.3.

2.2 Synthesis of silver nanocluster

Ag NCs, which are mainly composed of Ag, have been widely studied in recent years because of their relatively high quantum yields in terms of luminescence.[43] Similar to Au NCs, Ag NCs can be synthesized with atomic precision using ligands such as SR, phosphine, and C≡CR. In this section, we describe several examples.

2.2.1 Thiolate-protected silver nanoclusters. Regarding SR-protected Ag NCs (Ag$_n$(SR)$_m$), the geometry of Ag$_n$(SR)$_m$ was determined using $[Ag_{44}(SR)_{30}]^{4-}$ in 2013 for the first time.[251,252] The general synthetic method involves dissolving AgNO$_3$ in methanol or another solution, adding a thiol ligand, and generating an Ag(I)–SR complex. Then, the Ag(I)–SR complex is dissolved in solution, NaBH$_4$ is added and stirred, and Ag$_n$(SR)$_m$ is obtained by washing/separation. For example, in 2018, Zhu and Jin et al. synthesized Ag$_{146}$Br$_2$(TIBT)$_{80}$ (TIBT = 4-isopropylbenzenethiolate).[253] First, Ag(I)–TIBT was synthesized by mixing AgNO$_3$ and 4-isopropylbenzenethiol in a mortar. Next, NaBH$_4$ was added to this mixture and reacted for 72 h. Then, the mixed solution was separated, and the precipi-

tate was washed to obtain pure Ag$_{146}$Br$_2$(TIBT)$_{80}$. From SC-XRD, Ag$_{146}$Br$_2$(TIBT)$_{80}$ was found to have an Ag$_{51}$ core structure protected by a shell of Ag$_{95}$Br$_2$(TIBT)$_{80}$ (Fig. 9Aa). The optical absorption spectrum showed four peaks in the visible region, indicating an optical gap of 0.5 eV (Fig. 9Ab).

Alloy NCs based on Ag$_n$(SR)$_m$ were also reported. In 2023, Wang, Yan, and Wu et al. synthesized fcc-structured bimetallic

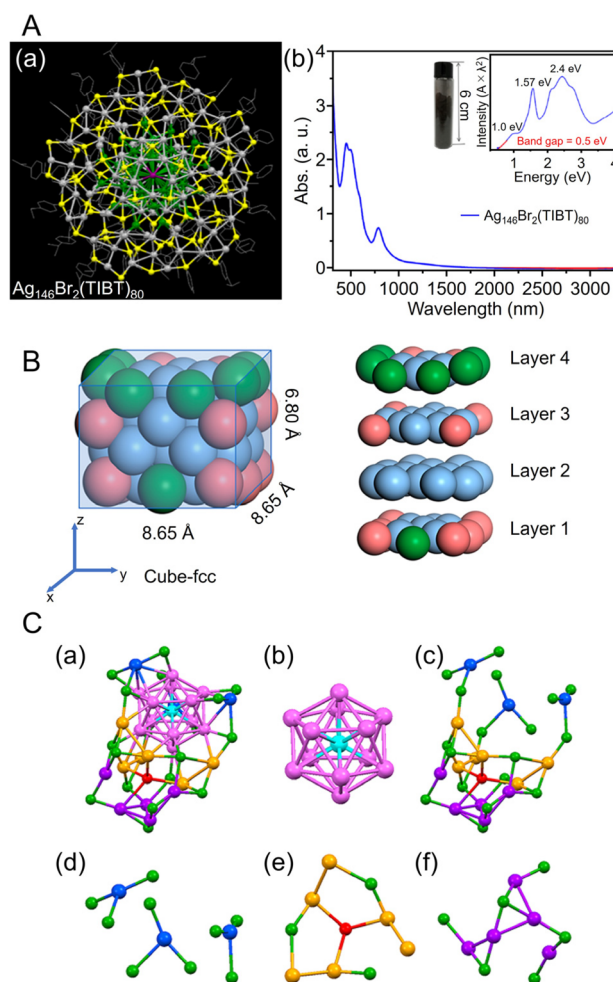**Fig. 9** (A) (a) Top views of the total structure of the Ag$_{146}$Br$_2$(TIBT)$_{80}$. Color labels: dark gray/green = Ag, yellow = S, purple = Br; the carbon tails are shown in wire-frame mode. (b) UV/Vis/NIR absorption spectra of the Ag$_{146}$Br$_2$(TIBT)$_{80}$ in CCl$_4$. Inset: Photograph of 5.08 g of Ag$_{146}$Br$_2$(TIBT)$_{80}$ in a vial, and the spectrum plotted on the photon energy scale (the y-axis is transformed from the wavelength scale spectrum by Abs × λ^2 to preserve the oscillator strength). (B) Size and slicing of the M$_{50}$ kernel in [Ag$_{39}$Cu$_{11}$(SC$_7$H$_7$O)$_{32}$]$^{2+}$. Color codes: pure blue, Ag; pink, Cu; green, Ag/Cu; yellow, S; red, O; gray, C. For clarity, all H atoms are omitted. (C) Structural analysis of [AuAg$_{26}$(S-Adm)$_{18}$S]$^-$. (a) The framework structure of AuAg$_{26}$, (b) the AuAg$_{12}$ icosahedron kernel, (c) the Ag$_{14}$(SR)$_{18}$S open shell, (d) three-AgS$_3$ motif, (e) Ag$_6$(SR)$_3$S motif, (f) Ag$_5$(SR)$_6$ motif. Color code: azure, Au; magenta/blue/orange/violet, Ag; red, single S atom; green, other S. The C and H atoms are omitted for clarity. (A) is reproduced with permission from ref. 253. Copyright 2018 American Chemical Society. (B) is reproduced with permission from ref. 254. Copyright 2023 American Chemical Society. (C) is reproduced with permission from ref. 255. Copyright 2020 American Chemical Society.

NCs ($[Ag_{41}Cu_9(SC_7H_7O)_{32}]^{2+}$) using a one-pot method and achieved surface substitution of alloy clusters with an increased Cu/Ag atomic ratio ($[Ag_{39}Cu_{11}(SC_7H_7O)_{32}]^{2+}$), without changing the reaction conditions.[254] In this synthesis, $AgNO_3$ and copper(II) acetylacetonate ($Cu(acac)_2$) were added as precursors in the appropriate ratios for the respective NCs, 3-methoxythiophenol was added and stirred, and the mixture was co-reduced with $NaBH_4$. These NCs have an fcc structure consisting of four layers, with different atoms exposed on the surface depending on the Ag/Cu ratio (Fig. 9B). In 2021, Liu and Huang *et al.* synthesized S-Adm (1-adamantanethiolate)-protected bimetallic NCs ($[AuAg_{26}(S\text{-}Adm)_{18}S]^-$) using a one-pot method.[255] For this synthesis, $AgNO_3$ and $AuCl_3$ solutions were mixed, and 1-adamantanethiol was added to the mixture. Then, PPh_3, tetraphenylphosphonium bromide (PPh_4Br), and $NaBH_4$ were added and kept to form $[AuAg_{26}(S\text{-}Adm)_{18}S]^-$, in which the Ag_{12} core covers the central Au atom and the Ag_{14} shell covers the core (Fig. 9C). These differ from common 25-mer NCs in that the outer Ag_{14} shell has a large open shell structure consisting of three different motifs.

2.2.2 Phosphine-protected silver nanoclusters. Ag NCs co-protected by SR and phosphine have also been reported. In 2022, Wang and Zang *et al.* reported the synthesis of $[Ag_{39}(PFBT)_{24}(PPh_3)_8]^{2-}$ (PFBT = pentafluorobenzenethiolate) (Fig. 10A).[256] In this synthesis, pentafluorobenzenethiol, PPh_3, and $NaBH_4$ were added to a solution of $AgNO_3$ and vigorously stirred. They also synthesized $[Ag_{37}Cu_2(PFBT)_{24}(PPh_3)_8]^{2-}$ by dissolving $AgNO_3$ and copper(I) chloride (CuCl) and then adding PFBT, PPh_3, and $NaBH_4$ while stirring. However, if trifluoroacetate copper is used as the Cu precursor instead of CuCl, the co-crystal of $[Ag_{37}Cu_2(PFBT)_{24}(PPh_3)_8]^{2-}\cdot[Ag_{14}(PFBT)_6(PPh_3)_8]$ can be obtained. In the structure of $[Ag_{39}(PFBT)_{24}(PPh_3)_8]^{2-}$ (Fig. 10Aa), the $Ag_{13}@Ag_{18}$ core is covered by $Ag_8(PFBT)_6(PPh_3)_8$, but when alloyed with Cu, the two outer Ag atoms are replaced with Cu atoms (Fig. 10Ab). In addition, the optical absorption spectra show that $[Ag_{39}(PFBT)_{24}(PPh_3)_8]^{2-}$ exhibits peaks at 426 and 524 nm, which are caused by charge transfer from the ligand to the metal or from the metal to the ligand. In addition, Cu doping shifts the peaks to the lower energy side of these peaks (Fig. 10B).

2.2.3 Other ligand-protected silver nanoclusters. Reports have also focused on the synthesis of Ag NCs protected by C≡CR ligands, similar to Au NCs. In 2017, Li and Zhang *et al.* reported the synthesis of $[Ag_{74}(C\equiv CPh)_{44}]^{2+}$.[257] In this synthesis, 1,3-bis(diphenyphosphino)propane (DPPP) and PhC≡CH were first added to a solution of dissolved $AgNO_3$ and stirred, and then $NaBH_4$ was added. In addition to C≡CPh ligands, many reports have considered the synthesis of Ag NCs protected by C≡C^{t}Bu, which is a C≡CR ligand with a *tert*-butyl group. In 2021, Tang, Jin, and Tang *et al.* reported the synthesis of C≡C^{t}Bu-protected Ag_{15} NCs ($[Ag_{15}(C\equiv C^tBu)_{12}]^+$) and their application in CRRs.[258] In this synthesis, HC≡C^{t}Bu, MeONa, and sodium cyanoborohydride ($NaBH_3CN$) are first added to a silver trifluoroacetate solution and stirred. Subsequently, $[Ag_{15}(C\equiv C^tBu)_{12}]^+$ is synthesized by

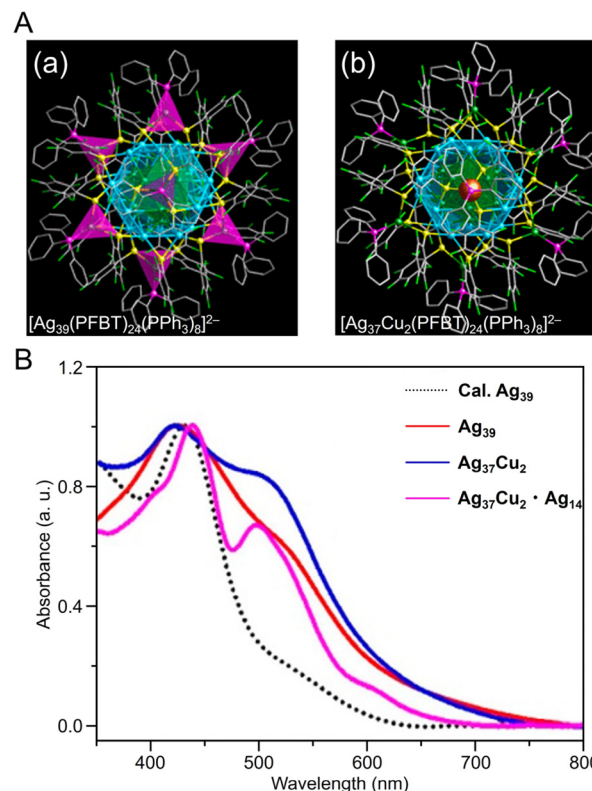**Fig. 10** (A) Overall structure of (a) $[Ag_{39}(PFBT)_{24}(PPh_3)_8]^{2-}$ and (b) $[Ag_{37}Cu_2(PFBT)_{24}(PPh_3)_8]^{2-}$. (B) UV/Vis absorbance spectra of $[Ag_{39}(PFBT)_{24}(PPh_3)_8]^{2-}$ (red), $[Ag_{37}Cu_2(PFBT)_{24}(PPh_3)_8]^{2-}$ (blue), and $[Ag_{37}Cu_2(PFBT)_{24}(PPh_3)_8]^{2-}\cdot[Ag_{14}(PFBT)_6(PPh_3)_8]$ (purple) in solution. (A) and (B) are reproduced with permission from ref. 256. Copyright 2022 American Chemical Society.

cooling and extraction with a mixture of dichloromethane and CH_3CN (Fig. 11A). The optical absorption spectrum of $[Ag_{15}(C\equiv C^tBu)_{12}]^+$ shows five peaks at 360, 480, 508, 542, and 580 nm (Fig. 11B). Additionally, $[Ag_{15}(C\equiv C^tBu)_{12}]^+$ has a core/shell structure of $Ag@Ag_8@Ag_6$, with an irregularly shaped cubic Ag8 in the second layer and an octahedron of Ag_6 in the outermost shell (Fig. 11A). In 2022, Tang, Wang and Tang *et al.* reported the synthesis of $Ag_{32}(C\equiv CPh(CF_3)_2)_{24}$ ($HC\equiv CPh(CF_3)_2$ = 3,5-bis(trifluoromethyl)phenylacetylene) based on Chen's and Tang's synthetic method[259] for $Au_{36}(C\equiv CPh)_{24}$ reported in 2020 (Fig. 12A).[260] In this synthesis, MeONa, $HC\equiv CPh(CF_3)_2$, and $NaBH_3CN$ are added to a solution of silver trifluoroacetate (CF_3COOAg) and stirred. The purple-black crystals are synthesized by centrifuging the mixed solution to remove the precipitate, followed by washing/extraction. $Ag_{32}(C\equiv CPh(CF_3)_2)_2$ has an Ag_5 core and $Ag_5@Ag_{12}$ kernel in the center, according to SC-XRD, and the surface is protected by four different ligands (Fig. 12A). The optical absorption spectra reveal peaks at 518 and 656 nm (Fig. 12B).

Many examples of Ag-based alloy NCs protected by C≡CR have also been reported. In 2021, Pei and Tang *et al.* reported the synthesis of an Ag–Cu alloy cluster ($[Ag_9Cu_6(C\equiv C^tBu)_{12}]^+$) (Fig. 13A).[244] In this synthesis, $^tBuC\equiv CAg$ was used as the

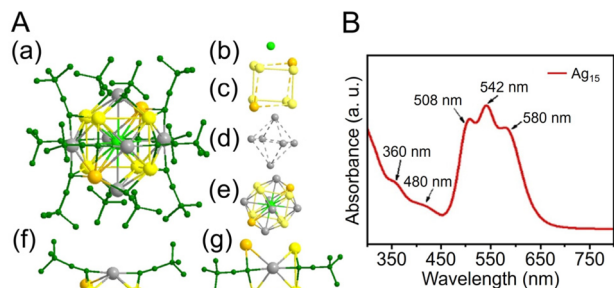**Fig. 11** (A) (a) The overall structure of $[Ag_{15}(C\equiv C^tBu)_{12}]^+$. (b)–(d) Shell-by-shell representations of the metal framework, Ag@Ag$_8$@Ag$_6$ (note that there is no bond between the orange silver atom and the adjacent three silver atoms (yellow) in the frame of the Ag$_8$ cube; similarly, the six capping Ag atoms form an octahedron with no bonds between them). (e) Metal framework of $[Ag_{15}(C\equiv C^tBu)_{12}]^+$. (f) and (g) Side and top views of the six Ag(C≡C^{t}Bu)$_2$ staple units capping a silver square of the Ag$_8$ cube. Ag gray/yellow/orange/light-green, C dark green; all hydrogen atoms are omitted for clarity. (B) UV/Vis absorbance spectrum of $[Ag_{15}(C\equiv C^tBu)_{12}]^+$. (A) and (B) are reproduced with permission from ref. 258. Copyright 2021 Wiley-VCH GmbH.

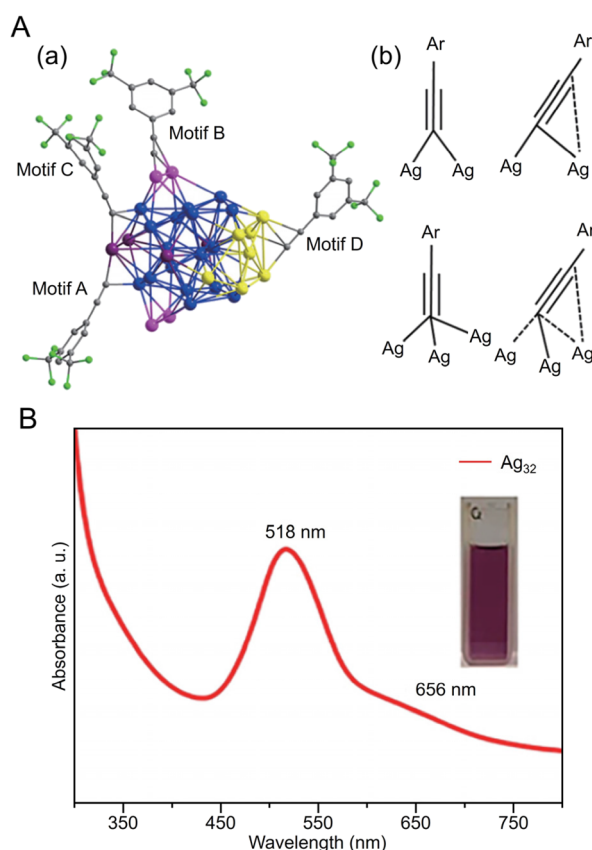**Fig. 12** (A) (a) Four types of ligand–metal bonding motifs in Ag$_{32}$(C≡CPh(CF$_3$)$_2$)$_{24}$. (b) Four motifs in Ag$_{32}$(C≡CPh(CF$_3$)$_2$)$_{24}$ coordination modes for alkynyl ligands. Color code: Ag, blue/pink/purple/yellow; C, gray; and F, green. (B) UV/Vis absorbance spectrum of Ag$_{32}$(C≡CPh(CF$_3$)$_2$)$_{24}$. Inset: photograph of the cluster in CH$_2$Cl$_2$. (A) and (B) are reproduced with permission from ref. 260. Copyright 2022 Springer Nature.

silver precursor, and bis(triphenylphosphine)copper borohydride $((PPh_3)_2CuBH_4)$ was used as the copper precursor. First, $^tBuC\equiv CAg$ was mixed with sodium hexafluoroantimonate (NaSbF$_6$), to which $(PPh_3)_2CuBH_4$ was added, and $[Ag_9Cu_6(C\equiv C^tBu)_{12}]^+$ was obtained by stirring and reducing the mixture in the dark. Notably, $[Ag_8Au_7(C\equiv C^tBu)_{12}]^+$, which has a similar geometric structure to $[Ag_9Cu_6(C\equiv C^tBu)_{12}]^+$, can also be synthesized.[261] Both NCs are composed of an M$_1$ kernel@Ag$_8$ cube@M$_6$ octahedral structure with a bcc basis (Fig. 13A), but they have slightly different geometric structures depending on the atomic diameters and argentophilic Ag–Ag interaction (Fig. 13B), which affect their optical properties and stability. In 2017, Mizuta et al. reported the synthesis of Pt$_5$Ag$_{22}$(C≡CPh)$_{32}$, obtained by mixing PhC≡CAg and H$_2$PtCl$_6$·6H$_2$O, and then adding NaBH$_4$ and stirring in the dark.[262] In 2022, Tang, Hwang and Hyeon et al. synthesized an alloy NC of Ag and Cu co-protected by C≡CPh(CF$_3$)$_2$ and DPPE $([Ag_{15}Cu_6(C\equiv CPh(CF_3)_2)_{18}(DPPE)_2]^-)$.[263] In this synthesis, a silver complex and C≡CPh(CF$_3$)$_2$ ligand were stirred with $(PPh_3)_2CuBH_4$ as a Cu precursor, then washed and extracted from the organic phase, which produced black crystals. The structure of $[Ag_{15}Cu_6(C\equiv CPh(CF_3)_2)_{18}(DPPE)_2]^-$ is composed of three layers, Ag@Ag$_8$@Ag$_2$Cu$_4$ (Fig. 13C), with a single Ag atom at the center, followed by an Ag$_8$ cube in the second layer and an Ag$_2$Cu$_4$ octahedron in the third layer, with two Ag$_2$(DPPE) capping the Ag–Cu or Ag–Ag interactions to form $[Ag_{15}Cu_6(C\equiv CPh(CF_3)_2)_{18}(DPPE)_2]^-$ (Fig. 13C).

In addition to ligand-protected Ag NCs, many reports have focused on the synthesis of Ag NCs using anions, such as halide ions, chalcogenide ions, oxoanions, and polyoxometalates (POMs), as templates.[264,265] In 2022, Liu et al. used a solvothermal reaction to synthesize POM-templated Ag NCs (Ag$_{49}$Mo$_{16}$) protected by six thiacalix[4]arenes (TC4A).[266] In this synthesis, TC4A was mixed with ^iPrSAg, CH$_3$COOAg, and ammonium molybdate tetrahydrate $((NH_4)_6Mo_7O_{24}·4H_2O)$, and then triethylamine was added dropwise. After that, light brown crystals were obtained by subjecting the mixture to heat treatment.

As mentioned above, many synthetic examples of Ag NCs protected by organic ligands, such as SR, phosphine, C≡CR, and template types, have been reported. These Ag NCs are also expected to be applied in electrochemical CRRs. In section 3.4, we describe CRRs using mainly the Ag NCs introduced in this section.

2.3 Synthesis of copper nanocluster

Cu is more abundant than Au and Ag, and thus Cu-based nanomaterials have advantages such as low environmental burden and low cost. Furthermore, Cu-based catalysts have the appropriate adsorption energy for CO$_2$ and exhibit promising CRR activity, with the ability to produce a variety of organic products from CO$_2$. Moreover, Cu NCs can be synthesized with atomic precision using ligands such as SR, phosphine, and C≡CR.[44,56,236,267–271] Here, we describe the existing synthesis methods for Cu NCs protected by the above ligands.
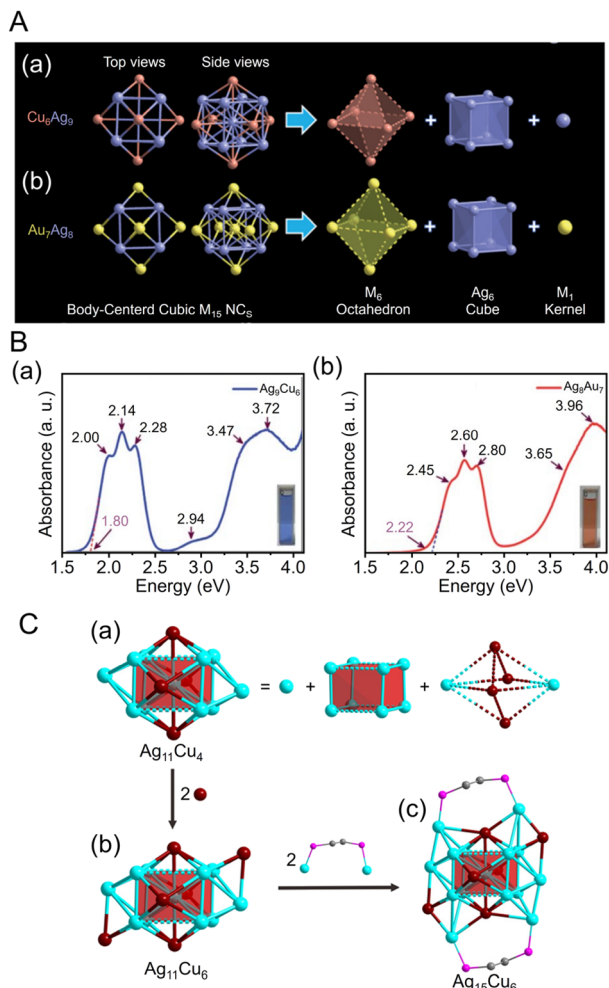
Fig. 13 (A) Anatomy of (a) $[Ag_9Cu_6(C\equiv C^tBu)_{12}]^+$ and (b) $[Ag_8Au_7(C\equiv C^tBu)_{12}]^+$. Color legend: Au, yellow; Ag, purple; Cu, orange. (B) Experimental absorbance spectra plotted in the energy axis of (a) $[Ag_9Cu_6(C\equiv C^tBu)_{12}]^+$ and (b) $[Ag_8Au_7(C\equiv C^tBu)_{12}]^+$. (C) Structure analysis of the $[Ag_{15}Cu_6(C\equiv CPh(CF_3)_2)_{18}(DPPE)_2]^-$. (a) Structure anatomy of the $Ag_{11}Cu_4$ metal core. (b) Capping of two opposite Ag_3 faces of the $Ag_{11}Cu_4$ core forms the structure of $Ag_{11}Cu_6$. (c) Stabilization of the $Ag_{11}Cu_6$ metal framework by two Ag_2DPPE motifs forms the structure of $[Ag_{15}Cu_6(C\equiv CPh(CF_3)_2)_{18}(DPPE)_2]^-$. Color legend: turquoise, Ag; dark red, Cu; pink, P; gray, C. (A) and (B) are reproduced with permission from ref. 244. Copyright 2021 Royal Society of Chemistry. (C) is reproduced with permission from ref. 263. Copyright 2022 American Chemical Society.

2.3.1 Thiolate-protected copper nanoclusters. Cu NCs partially protected by SR have been synthesized, similar to the reports for $Au_n(SR)_m$ and $Ag_n(SR)_m$. In 2009, Liu et al. synthesized $Cu_8(H)(L1)_6PF_6$ (L1 = 9H-carbazole-9-carbodithioate) by dissolving tetrakis(acetonitrile)copper(I) hexafluorophosphate ($Cu(CH_3CN)_4PF_6$) and $NH_4[S_2P(OiPr)_2]$ in acetone and stirring to remove impurities.[272] In 2022, Wang and Zang et al. synthesized three Cu NCs with the same size, namely $Cu_8(S^tBu)_4(L1)_4$ and $Cu_8(S^tBu)_4(L2)_4$ (L2 = O-ethyl carbonodithiolate), in addition to $Cu_8(H)(L1)_6PF_6$, and their CRR activities were compared.[273] The synthesis of $Cu_8(S^tBu)_4(L1)_4$ used

^tBuSCu dissolved in chloroform as the Cu precursor, and L1 dissolved in methanol was added and mixed. $Cu_8(S^tBu)_4(L2)_4$ was synthesized by the same procedure but with L2 instead of L1. Notably, $Cu_8(H)(L1)_6PF_6$ contains a slightly twisted cubic Cu_8 core, but the introduction of ^tBuS in $Cu_8(S^tBu)_4(L1)_4$ and $Cu_8(S^tBu)_4(L2)_4$ leads to the breakdown of the Cu_8 core and the formation of a tetrahedral Cu arrangement.

2.3.2 Phosphine-protected copper nanoclusters. As with Au and Ag NCs, phosphine-protected Cu NCs can also be synthesized. In 2015, Scott and Hayton et al. synthesized two Cu NCs by adding diphenyl silane (Ph_2SiH_2) to a slurry containing appropriate amounts of copper(I) acetate (Cu(OAc)), CuCl, and PPh_3 in benzene to obtain $[Cu_{25}H_{22}(PPh_3)_{12}]^+$ and $[Cu_{18}H_{17}(PPh_3)_{10}]^+$.[274] When these were extracted with benzene, only $[Cu_{18}H_{17}(PPh_3)_{10}]^+$ could be dissolved and separated by filtration. Most Cu NCs are composed of cationic Cu, but $[Cu_{25}H_{22}(PPh_3)_{12}]^+$ was found to contain partially zerovalent Cu(0). This is the first report of such metallic Cu NCs with a Cu_{13} icosahedral core and four $[Cu(PPh_3)]_3$ capping structures (Fig. 14A). In 2019, Wang and Zhu et al. reported the synthesis of $[Cu_{25}H_{22}(PPh_3)_{12}]^+$, $[AuCu_{24}H_{22}(PPh_3)_{12}]^+$, $[Cu_{25}H_{22}(P(p\text{-}FPh)_3)_{12}]^+$ (P(p-FPh)$_3$ = tris(4-fluorophenyl)phosphine), and $[AuCu_{24}H_{22}(P(p\text{-}FPh)_3)_{12}]^+$ with both ligand exchange and Au doping.[275] $[AuCu_{24}H_{22}(P(p\text{-}FPh)_3)_{12}]^+$ was synthesized by adding $Cu(acac)_2$ and $HAuCl_4 \cdot 3H_2O$ to the precursor, followed by stirring and aging with PPh_3 and $NaBH_4$ as ligands. $[Cu_{25}H_{22}(P(p\text{-}FPh)_3)_{12}]^+$ was also synthesized by adding $P(p\text{-}FPh)_3$ and $NaBH_4$ to a dissolved solution of $Cu(acac)_2$ and stirring. $AuCu_{24}H_{22}(P(p\text{-}FPh)_3)_{12}$ was synthesized by adding $HAuCl_4 \cdot 3H_2O$ at the beginning of the synthetic scheme for $Cu_{25}H_{22}(P(p\text{-}FPh)_3)_{12}$ described above. All three NCs contain distorted icosahedral MCu_{12} (M = Au or Cu) structures and are protected by four Cu_3P_3 shells (Fig. 14A). UV/Vis measurements of these materials also showed that $[Cu_{25}H_{22}(PPh_3)_{12}]^+$ and $[Cu_{25}H_{22}(P(p\text{-}FPh)_3)_{12}]^+$ have absorption at 459 and 635 nm, whereas $[AuCu_{24}H_{22}(PPh_3)_{12}]^+$ and $[AuCu_{24}H_{22}(P(p\text{-}FPh)_3)_{12}]^+$ are more blue shifted than the undoped ones. This indicates that the electronic structures of NCs can be changed by an inactive metal doping of Au heteroatoms (Fig. 14B).

2.3.3 Other ligand-protected copper nanoclusters. In addition to SR and phosphine protection, many reports have focused on the synthesis of Cu NCs protected with $C\equiv CR$ and fluoroacetic acid. In 2020, Aikens and Sun et al. synthesized $[Cu_{23}(C\equiv C^tBu)_{13}(CF_3COO)_6]^0$ containing Cu(0) using various reducing agents.[276] First, copper(II) trifluoroacetate ($Cu(CF_3COO)_2$), Cu powder, and $^tBuC\equiv CH$ were mixed and stirred in dichloromethane and methanol, and when the solution turned pale yellow, Ph_2SiH_2 was added. After aging, the crystals were filtered and purified at room temperature to give $[Cu_{23}(C\equiv C^tBu)_{13}(CF_3COO)_6]^0$. The Cu NCs consist of a Cu_{19} outer shell and Cu_4 tetrahedral core (Fig. 15A). Furthermore, UV/Vis measurements of the solid using diffuse reflection spectroscopy revealed that the band gap of $[Cu_{23}(C\equiv C^tBu)_{13}(CF_3COO)_6]^0$ is approximately 1.45 eV, which is consistent with the value calculated based on DFT calculations.
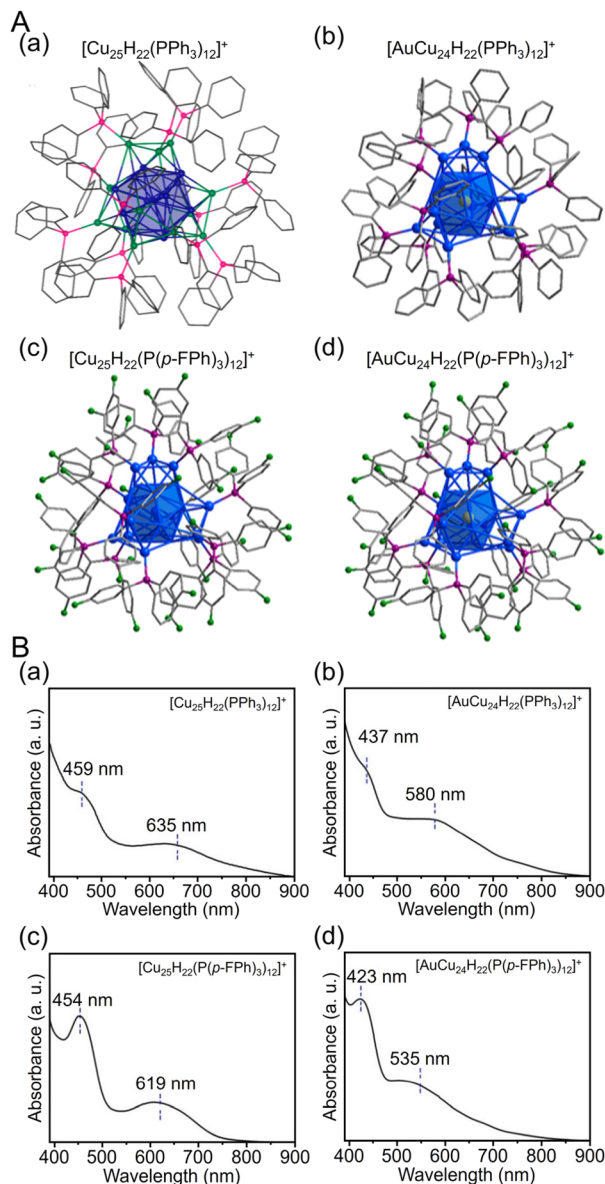
Fig. 14 (A) Total structures and (B) UV/Vis spectra of (a) $[Cu_{25}H_{22}(PPh_3)_{12}]^+$, (b) $[AuCu_{24}H_{22}(PPh_3)_{12}]^+$, (c) $[Cu_{25}H_{22}(P(p\text{-}FPh)_3)_{12}]^+$ and (d) $[AuCu_{24}H_{22}(P(p\text{-}FPh)_3)_{12}]^+$. Color labels: gold = Au; blue = Cu; green = F; purple = P; gray = C. All H atoms are omitted for clarity. (A) (a) is reproduced with permission from ref. 274. Copyright 2015 American Chemical Society. (A) (b–d) and (B) are reproduced with permission from ref. 275. Copyright 2019 American Chemical Society.

Fig. 15 (A) (a) Total structure and (b) metal framework of the $[Cu_{23}(C\equiv C^tBu)_{13}(CF_3COO)_6]^0$. Color labels: Orange, Cu; green, F; gray, C; red, O. (B) Molecular structure of (a) $[Au_{19}Cu_{30}(C\equiv C\text{-}3\text{-}SC_4H_3)_{22}(PPh_3)_6Cl_2]^{3+}$ and (b) $[Au_{19}Cu_{30}(C\equiv CPh)_{22}(PPh_3)_6Cl_2]^{3+}$. Anatomy of $Au_{19}Cu_{30}$ kernel structure in $Au_{19}Cu_{30}$ clusters. (c) Centered icosahedron $Au@Au_{12}$. (d) Cu_{30} icosidodecahedron. (e) $Au@Au_{12}@Cu_{30}$ multi shelled structure. (f) Six outmost Au atoms highlighted in green. (A) is reproduced with permission from ref. 276. Copyright 2020 American Chemical Society. (B) is reproduced with permission from ref. 277. Copyright 2017 American Chemical Society.

Cases of Cu-based alloy NCs protected by C≡CR ligands have also been reported. In 2017, Jiang and Wang *et al.* reported the synthesis of two types of Au–Cu alloy clusters protected by 3-ethynylthiophene ($H_3C_4S\text{-}3\text{-}C\equiv CH$) or PhC≡CH.[277] First, a mixture of the $H_3C_4S\text{-}3\text{-}C\equiv CAuPPh_3$ precursor, chloro (triphenylphosphine)gold(I) (PPh_3AuCl), and copper(II) nitrate ($Cu(NO_3)_2$) was reduced by adding $NaBH_4$. Then, the reaction proceeded in the dark, and the resulting solid was washed to obtain $[Au_{19}Cu_{30}(C\equiv C\text{-}3\text{-}SC_4H_3)_{22}(PPh_3)_6Cl_2]^{3+}$. They also synthesized $[Au_{19}Cu_{30}(C\equiv CPh)_{22}(PPh_3)_6Cl_2]^{3+}$ protected with

PhC≡C by adding PhC≡CAuPPh$_3$ as the Au precursor and CuCl and $Cu(NO_3)_2$ as the Cu precursors in the above synthetic scheme. The NCs have identical internal structures (Fig. 15B). At the center is an Au_{13} core, followed by a Cu_{30} icosahedral shell, which has a characteristic structure of six Au atoms bonded to this shell portion (Fig. 15B).

As described above, many synthetic examples of Cu NCs protected by various organic ligands, such as SR, phosphine, and C≡CR, have been reported. These Cu NCs are expected to be applied in electrochemical CRRs, as described in section 3.5.

3. Electrochemical CO_2 reduction reactions of atomically precise metal nanoclusters

3.1 Atomically precise metal nanoclusters as electrocatalysts

As the depletion of fossil resources and the problem of global warming become more serious, there is a growing desire to diversify the industrial sources of energy and reduce greenhouse gases. Electrocatalysts, which induce chemical reactions using electrical energy, have been attracting attention as a means of addressing these problems. Electricity can be produced cleanly using natural energy sources (*i.e.*, without also producing CO_2), and electrocatalysts can be used to convert the unused surplus of those sources into chemical energy. Doing so would reduce the loss of electricity in the transmission and storage processes, promoting a cleaner and more sustainable society. Among the various electrocatalytic reactions, in water electrolysis, fuel cells, and electrochemical CO_2 reduction are the most widely studied.

In recent years, there has been a focus on the development of electrocatalysts that reduce the activation energy of these electrocatalytic reactions and allow them to proceed with less power consumption. In general, an efficient electrocatalyst has many active sites with high reaction rates. The number of active sites is an important factor related to the specific surface area of the catalyst, and the reaction rate is largely related to the adsorption energy of the reacting molecules on the catalyst surface. Chemical reactions at the catalyst surface exhibit the highest activity based on the Sabatier principle, only occurring when the Gibbs energy of adsorption between the catalyst and the reactant is appropriate.[278] The reaction cannot occur if there is no adsorption of the reactant on the electrode surface, but if the adsorption is too strong, the reaction cannot proceed. Therefore, depending on the metal species of the electrocatalyst and the adsorption energy of the reactants, the reaction efficiency follows a mountainous trend, called a volcano plot.[279]

The metal NCs described in section 2 generally have high catalytic activities in a variety of heterogeneous systems based on their large specific surface areas and unique geometric/electronic structures. Recently, many groups have studied the application of metal NCs to electrocatalysts, considering that metal NCs have the potential to outperform conventional materials. Furthermore, the geometric structure of many metal NCs can be revealed by SC-XRD, and the adsorption and reaction processes between the metal NCs as an active site, and reactants can be estimated using theoretical calculations.[158,280–287] Therefore, metal NCs have been widely studied as model catalysts to elucidate the reaction mechanisms. If we can clarify the correlation between the electronic/geometric structure of metal NCs and their electrocatalytic activity, we may find new ways to enhance the catalytic activity.

Here, we summarize the application of ligand-protected metal NCs in electrochemical CRRs, with a focus on electrocatalysts using ligand-protected metal NCs obtained by liquid-phase reduction, which can be easily synthesized in large quantities. Particularly, we describe the use of metal NCs that have a well-defined geometric structure.

3.2 Electrocatalytic CO_2 reduction reactions using atomically precise metal nanoclusters

Electrochemical CRRs provide a variety of useful reduction products depending on the number of electrons involved in the reaction.[279] For example, 2-electron transfer reduction produces CO or HCOOH, 8-electron transfer reduction produces CH_4, 16-electron transfer reduction produces ethylene (C_2H_4), and reduction by more electrons is also possible (eqn (1)–(7)).[89,288] First, CO_2 is adsorbed on the surface of the metal catalyst and then interacts with the transferred electrons or protons to form an intermediate. Next, these intermediates undergo various reactions and finally desorb from the catalyst surface. There are various theories, but (i) *COOH and (ii) *OCHO are the primary intermediates in most cases. Among these, (i) *COOH is the first intermediate in the formation of CO and various hydrocarbons, and (ii) *OCHO is most likely an intermediate in the formation of HCOOH. (iii) *COCHO, produced by C–C coupling of *CHO and CO, has been reported as an important intermediate in the formation of C_2 compounds. Therefore, different metal species also have different binding energies to these intermediates, and these differences change the main products (Fig. 16). For example, using bulk metals as catalysts, (i) CO is obtained as a product for Au or Ag; (ii) HCOOH is obtained for Pb, Sn, and In; and (iii) a variety of organic products, such as aldehydes, alcohols, and C_2 compounds, are obtained for Cu. However, certain metals, such as Pt, Ni, and Pd, which are highly active in HER, are less useful catalysts in CRR because the adsorption of *H prevents the formation of carbon products.[289,290] Additionally, the specific geometric/electronic structures of metal NCs affect the selectivity. As described in section 2, many metal NCs can be synthesized under atmospheric conditions with atomic accu-
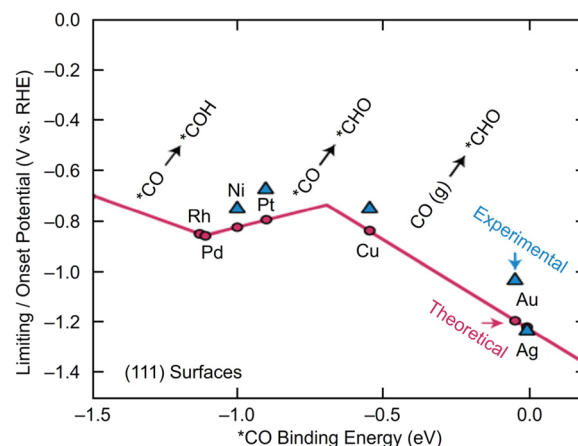

Fig. 16 A volcano plot of CO_2 reduction reactions for (111) bulk metals. This figure is reproduced with permission from ref. 279. Copyright 2017 AAAS.

racy, mainly for group 11 metals (Ag, Au, and Cu). Therefore, most applications of electrochemical CRRs have been based on these metal NCs. In this section, we mainly discuss the relationship between the structure of metal NCs and electrochemical CRR activity in terms of (1) size effects, (2) structure effects, (3) ligand effects, and (4) heterometallic doping effects, with respect to the application of Ag, Au, and Cu NCs in electrochemical CRRs.

3.3 Electrocatalytic CO_2 reduction reactions using gold nanoclusters

Many studies of electrochemical CRRs with Au NCs have been reported since 2012 (Tables 1–5). Kauffman et al. reported the first study on electrochemical CRRs using $Au_n(SR)_m$. They prepared the catalyst ink by sonicating a solution containing $[Au_{25}(PET)_{18}]^-$ (Fig. 2AB) dissolved in acetone, carbon black (CB), Nafion, and methanol. Then, the prepared catalyst ink was loaded on a glassy carbon electrode (GCE) and dried naturally to form the working electrode. Evaluation of the CRR activity showed that the current curves were different after saturation with nitrogen (N_2) and CO_2 when the potentials were traced to negative. The onset potential for CO formation was found to be −0.193 V vs. RHE, according to the potential-dependent product analysis (Fig. 17A). Compared with the

ideal CO_2 to CO redox potential (−0.103 V vs. RHE), the overvoltage of bulk Au was 200–300 mV, whereas that of $[Au_{25}(PET)_{18}]^-$ was only 90 mV (Fig. 17B). The FE of CO formation (FE_{CO}) was approximately 100% at −1.0 V vs. RHE. This was 7–700 times higher than Au NPs with 2–5 nm particle sizes and bulk Au. Furthermore, the FE_{CO} for $[Au_{25}(PET)_{18}]^-$ was stable at a relatively high selectivity of 80.8–99.6%, compared with 26.9–92.9% for bulk Au and 71.0–96.9% for Au NPs. The turnover frequency of CO (TOF_{CO}) was calculated to be 87 molecules per site per s. In addition, the absorption spectrum of $[Au_{25}(PET)_{18}]^-$ was maintained after electrochemical measurements, further indicating its stability.[291] The adsorption of CO_2 was also predicted using a simplified model of $[Au_{25}(SCH_3)_{18}]^-$ for the DFT calculation (Fig. 17C). As a result, the binding energy is 0.13 eV in the stable structure, where the oxygen atom of CO_2 interacts with the three S atoms located in the shell of Au_{25} (Fig. 17C). These small perturbations in the internal structure of the molecule were consistent with the physisorption of CO_2. CRRs were also investigated using $[Au_{25}(PET)_{18}]^z$ (z = −1, 0, and +1).[292] $[Au_{25}(PET)_{18}]^-$ exhibited higher activity for CO_2 reduction to CO than $[Au_{25}(PET)_{18}]^z$ (z = 0 and +1). From DFT calculations, they speculated that this is due to the stronger binding energy for CO_2 and H^+ co-adsorption.

Table 1 Representative references on CRR activity using Au NCs (section 3.3.1 Size effects)

Nanocluster/ nanoparticle	Electrolytes	Electrolyzer	Main product	Selectivity (@V vs. RHE)	Current density (mA cm^{-2} @V vs. RHE)	Stability (@V vs. RHE)	Ref.
$[Au_{25}(PET)_{18}]^-$	0.1 M KHCO$_3$ aq.	H-cell	CO	~100%@−1.0	N/A	N/A	291 [d]
Au 2 nm NPs				97%@−1.0	N/A	N/A	
Au 5 nm NPs				74%@−1.0	N/A	N/A	
Bulk Au NPs				27%@−1.0	N/A	N/A	
$[Au_{25}(PET)_{18}]^-$	0.1 M KHCO$_3$ aq.	H-cell	CO	99%@−1.0	N/A	N/A	292 [d]
$[Au_{25}(PET)_{18}]^0$				82%@−1.0	N/A	N/A	
$[Au_{25}(PET)_{18}]^+$				81%@−1.0	N/A	N/A	
$Au_{25}(SC_6H_{13})_{18}$	1.0 M KOH aq. or 3.0 M KOH aq.	Flow cell	CO	~90%@−0.56	59@−0.56	100 h@−1.16	295 [e]
$Au_{38}(SC_6H_{13})_{24}$				~90%@−0.56	100@−0.56	25 h@−1.16	
$Au_{144}(SC_6H_{13})_{60}$				~92%@−0.56	230@−0.56	25 h@−1.16	
$Au_{137}(PET)_{56}$	0.1 M NBu$_4$PF$_6$ in DMF	3 neck flask	N/A	N/A	N/A	N/A	294
$Au_{25}(PET)_{18}$	0.1 M KHCO$_3$ aq.	N/A	CO	~90%@−1.0	N/A	36 h@−1.0	293 [f]
$Au_{38}(PET)_{24}$ [b]	0.5 M KHCO$_3$ aq.	H-cell	CO	~100%@−0.77	32@−0.87	N/A	296 [f]
$Au_{38}(PET)_{24}$ [c]				~100%@−0.77	23@−0.87	N/A	
$Au_{144}(PET)_{60}$				~100%@−0.77	26@−0.87	N/A	
$Au_{333}(PET)_{79}$				~95%@−0.77	23@−0.87	N/A	
$Au_{28}(TBBT)_{20}$				~100%@−0.77	28@−0.87	N/A	
$Au_{36}(TBBT)_{24}$				~100%@−0.77	26@−0.87	N/A	
$Au_{279}(TBBT)_{84}$				~90%@−0.77	18@−0.87	N/A	
$Au_4(PPh_3)_4I_2$	0.5 M KHCO$_3$ aq.	H-cell	CO	~55%@−0.9	~3@−0.9	N/A	298 [g]
			H$_2$	~45%@−0.9	~3@−0.9	N/A	
$Au_{11}(PPh_3)_7I_3$			CO	~77%@−0.9	~5@−0.9	N/A	
			H$_2$	~23%@−0.9	~2@−0.9	N/A	
$[Au_6(DPPP)_4]^{2+}$	0.2 M KHCO$_3$ aq.	Flow cell	CO	~80%@−1.5[a]	−3.3@−1.5[a]	4 h@−1.5[a]	297 [h]
			H$_2$	~15%@−1.5[a]	N/A	N/A	
$[Au_9(PPh_3)_8]^{3+}$			CO	~83%@−1.5[a]	−3.1@−1.5[a]	N/A	
			H$_2$	~17%@−1.5[a]	N/A	N/A	
$[Au_{13}(DPPE)_5Cl_2]^{3+}$			CO	~90%@−1.5[a]	−3.3@−1.5[a]	N/A	
			H$_2$	~15%@−1.5[a]	N/A	N/A	
$Au_{101}(PPh_3)_{21}Cl_5$			CO	~76%@−1.5[a]	−6.6@−1.5[a]	N/A	
			H$_2$	~20%@−1.5[a]	N/A	N/A	

PET = phenylethanethiolate, PPh$_3$ = triphenylphosphine, TBBT = 4-tert-butylbenzenethiolate, SC$_6$H$_{13}$ = 1-hexanethiolate, DPPE = 1,2-bis(diphenylphosphino)ethane, DPPP = 1,3-bis(diphenylphosphino)propane. [a] vs. Ag/AgCl. [b] Au$_{38}$Q. [c] Au$_{38}$T. [d] Vulcan XC-72R. [e] Vulcan XC-72. [f] Carbon black. [g] Multi-walled carbon nanotube. [h] Carbon paper.

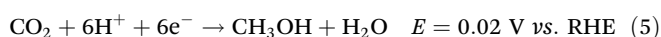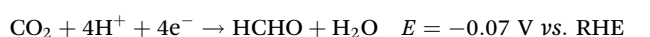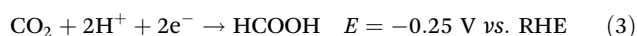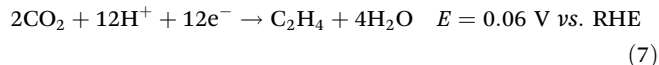**Table 2** Representative references on CRR activity using Au NCs (section 3.3.2 Structure effects)

Nanocluster/nanoparticle	Electrolytes	Electrolyzer	Main product	Selectivity (@V vs. RHE)	Current density (mA cm^{-2}@V vs. RHE)	Stability (@V vs. RHE)	Ref.
$[Au_{25}(PET)_{18}]^-$	0.5 M KHCO$_3$ aq.	H-cell	CO	73.5%@−1.07	N/A	N/A	299[c]
			H$_2$	24.9%@−1.07	N/A	N/A	
$[Au_{25}(PPh_3)_{10}(PET)_5Cl_2]^{2+}$			CO	~55%@−1.07	N/A	N/A	
			H$_2$	41.2%@−1.07	N/A	N/A	
$Au_{38}(PET)_{24}$[a]	0.5 M KHCO$_3$ aq.	H-cell	CO	~100%@−0.77	32@−0.87	N/A	296[d]
$Au_{38}(PET)_{24}$[b]				~100%@−0.77	23@−0.87	N/A	
$Au_{44}(TBBT)_{24}$	0.5 M KHCO$_3$ aq.	H-cell	CO	83%@−0.57	1.9@−0.57	N/A	300[e]
			H$_2$	~17%@−0.57	N/A		
$Au_{44}(PPh_3)(TBBT)_{26}$			CO	97%@−0.57	3.8@−0.57	60 h@−0.57	
			H$_2$	2.7%@−0.57	N/A		
$Au_{44}(PPh_3)_2(TBBT)_{24}$			CO	90%@−0.57	3.1@−0.57	N/A	
			H$_2$	~10%@−0.57	N/A		

PET = phenylethanethiolate, PPh$_3$ = triphenylphosphine, TBBT = 4-*tert*-butylbenzenethiolate. [a] Au$_{38}$Q. [b] Au$_{38}$T. [c] Vulcan XC-72R. [d] Carbon black. [e] Vulcan XC-72.

Table 3 Representative references on CRR activity using Au NCs (section 3.3.3 Ligand effects)
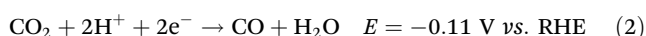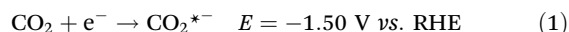
Nanocluster/nanoparticle	Electrolytes	Electrolyzer	Main product	Selectivity (@V vs. RHE)	Current density (mA cm^{-2}@V vs. RHE)	Stability (@V vs. RHE)	Ref.
$[Au_7(PPh_3)_7H_5]^{2+}$	0.5 M KHCO$_3$ aq.	H-cell	H$_2$	10%@−0.67	~6@−0.97	5 h@−0.77	232[d]
			CO	~90%@−0.67	~0@−0.97		
$[Au_8(PPh_3)_7]^{2+}$			H$_2$	~26%@−0.67	~1@−0.97	5 h@−0.77	
			CO	73.5%@−0.77	6.47@−0.97		
$[Au_{11}(PPh_3)_7(NHC^{Me})Cl_2]^+$	0.1 M KHCO$_3$ aq.	H-cell	CO	80%@−1.0	N/A	N/A	238[e]
$[Au_{11}(PPh_3)_8Cl_2]^+$				80%@−1.0	N/A	N/A	
$[Au_{11}(PPh_3)_7(NHC^{iPr})Cl_2]^+$				~30%@−1.0	N/A	N/A	
$[Au_{11}(DPPE)_5]^{3+}$	0.5 M KHCO$_3$ aq.	H-cell	CO	70.6%@−0.6	1.5@−0.6	N/A	231[f]
$[Au_{22}H_3(DPPE)_3(PPh_3)_8]^{3+}$				92.7%@−0.6	3.5@−0.6	10 h@−0.6	
$[Au_{24}(NHC^{Bn})_{14}Cl_2H_3]^{3+}$	0.1 M KHCO$_3$ aq.	MEA-cell	CO	N/A	10@2.4[a]	100 h@3.2[a,b]	249[g]
$[Au_{13}(NHC^{Bn})_9Cl_3]^{2+}$				N/A	10@2.5[a]	N/A	
Ag NPs				N/A	10@2.8[a]	N/A	
$[Au_{25}(PET)_{18}]^-$	0.5 M KHCO$_3$ aq.	H-cell	CO	~100%@−0.8	22@−0.8	N/A	301[h]
$[Au_{25}(SNap)_{18}]^-$				~95%@−0.8	20@−0.8		
$[Au_{25}(SePh)_{18}]^-$				~80%@−0.8	15@−0.8		
Au$_{25}$(PET)$_{18}$ (Electrochemical)[b]	0.1 M KHCO$_3$ aq.	H-cell	CO	82%@−0.59	N/A	3 h@−0.5	305[i]
Au$_{25}$(PET)$_{18}$(Thermal)[c]				64%@−0.59		3 h@−0.5	
$[Au_{28}(C_2B_{10}H_{11}S)_{12}(THT)_4]^{4+}$	0.5 M KHCO$_3$ aq.	H-cell	CO	98.5%@−0.9	~8@−0.9	5.5 h @−0.9	303[h]
$[Au_{28}(C_4B_{10}H_{11})_{12}(THT)_8]^{3+}$				~70%@−0.9	~4@−0.9	5.5 h @−0.9	
$[Au_{28}(Ph\text{-}form)_{12}]^{2+}$	0.5 M KHCO$_3$ aq.	H-cell	CO	96.5%@−0.57	N/A	40 h@−0.69	250[d]
PVP-coated Au NPs				~25%@−0.57	N/A	N/A	
$[Au_{55}(p\text{-}MBT)_{24}(PPh_3)_6]^{3+}$	0.1 M KHCO$_3$ aq.	H-cell	CO	94.1%@−0.6	~410@−0.9	4 h@−0.6	233[j]
$[Au_{25}(p\text{-}MBT)_5(PPh_3)_{10}Cl_2]^{2+}$				75.1%@−0.6	N/A	N/A	

PET = phenylethanethiolate, PPh$_3$ = triphenylphosphine, SNap = 1-naphthalenethiolate, SePh = phenylselenolate, NHC^{Me} = 1,3-dihydro-1,3-dimethyl-2*H*-benzimidazol-2-ylidene, NHC^{iPr} = 1,3-dihydro-1,3-diisopropyl-2*H*-benzimidazol-2-ylidene, Ph-form = *N*,*N*′-diphenylformamidinate, PVP = polyvinylpyrrolidone, *p*-MBT = 4-methylbenzenethiolate, NHC^{Bn} = 1,3-dibenzyl-1*H*-benzo[*d*]imidazol-2-ylidene, DPPE = 1,2-bis(diphenylphosphino)ethane, MEA = membrane electrode assembly. [a] vs. MEA-cell potential. [b] The ligand-removed Au$_{25}$(PET)$_{18}$ by electrochemical pretreatment. [c] The ligand-removed Au$_{25}$(PET)$_{18}$ by thermal pretreatment. [d] Multi-walled carbon nanotube. [e] Carbon paper. [f] Ketjen black (EC300J). [g] Carbon gas diffusion layer (TGP-H-060). [h] Vulcan XC-72R. [i] Sulfur-doped graphene. [j] Carbon.

$$CO_2 + e^- \rightarrow CO_2^{*-} \quad E = -1.50 \text{ V } vs. \text{ RHE} \quad (1)$$

$$CO_2 + 2H^+ + 2e^- \rightarrow CO + H_2O \quad E = -0.11 \text{ V } vs. \text{ RHE} \quad (2)$$

$$CO_2 + 2H^+ + 2e^- \rightarrow HCOOH \quad E = -0.25 \text{ V } vs. \text{ RHE} \quad (3)$$

$$CO_2 + 4H^+ + 4e^- \rightarrow HCHO + H_2O \quad E = -0.07 \text{ V } vs. \text{ RHE} \quad (4)$$

$$CO_2 + 6H^+ + 6e^- \rightarrow CH_3OH + H_2O \quad E = 0.02 \text{ V } vs. \text{ RHE} \quad (5)$$

$$CO_2 + 8H^+ + 8e^- \rightarrow CH_4 + 2H_2O \quad E = 0.17 \text{ V } vs. \text{ RHE} \quad (6)$$

$$2CO_2 + 12H^+ + 12e^- \rightarrow C_2H_4 + 4H_2O \quad E = 0.06 \text{ V } vs. \text{ RHE} \quad (7)$$

Next, the researchers investigated practical applications.[293] Specifically, they evaluated the relationship between the amount of $[Au_{25}(PET)_{18}]^-$ loaded per electrode area (using CB as the support) and their resulting particle size, which was determined by transmission electron microscopy (TEM) (Fig. 18A). As a result, the size of $[Au_{25}(PET)_{18}]^-$ was 1.4 ±

Table 4 Representative references on CRR activity using Au NCs (section 3.3.4 Doping effects)

Nanocluster/nanoparticle	Electrolytes	Electrolyzer	Main product	Selectivity (@V vs. RHE)	Partial current density (mA cm^{-2}@V vs. RHE)	Stability (@V vs. RHE)	Ref.
$[Au_{19}Cd_2(SC_6H_{11})_{16}]^-$	0.5 M KHCO$_3$ aq.	H-cell	CO	~95%@~−0.67	42@−0.9	N/A	308 [b]
$[Au_{23}(SC_6H_{11})_{16}]^-$				~65%@~−0.67	18@−0.9	N/A	
Au$_{25}$(PET)$_{18}$	1.0 M KHCO$_3$ aq.	H-cell	CO	~80%@−0.4	8@−0.8	25 h@−0.7	188 [c]
			HCOOH	~10%@−0.4			
Au$_{24}$Cd(PET)$_{18}$			CO	~90%@−0.4	35@−0.8	25 h@−0.7	
			HCOOH	~8%@−0.4			
Au$_{19}$Cd$_3$(S-tol)$_{18}$			CO	~60%@−0.4	5@−0.8	25 h@−0.7	
			HCOOH	0%@−0.4			
Au$_{38}$Cd$_4$(d-MBT)$_{30}$			CO	~60%@−0.4	12@−0.8	25 h@−0.7	
			HCOOH	~10%@−0.4			
Au$_{47}$Cd$_2$(TBBT)$_{31}$	0.5 M KHCO$_3$ aq.	H-cell	CO	96%@−0.57	3.2@−0.57	20 h@−0.57	306 [b]
Au$_{44}$(TBBT)$_{28}$				83%@−0.57	1.6@−0.57	20 h@−0.57	
1.5 nm Au NPs				76%@−0.67	1.0@−0.57	20 h@−0.67	
Au$_{25}$(SC$_6$H$_{13}$)$_{18}$	0.1 M KHCO$_3$ aq. + 0.4 M KCl	H-cell	H$_2$	~6%@−0.5	12@−1.0	N/A	309 [b]
			CO	~90%@−0.5			
PtAu$_{24}$(SC$_6$H$_{13}$)$_{18}$			H$_2$	~80%@−0.5	20@−1.0	N/A	
			CO	~20%@−0.5			
Au$_{38}$(SCH$_2$Ph^{t}Bu)$_{24}$	0.5 M KHCO$_3$ aq.	H-cell	CO	~70%@−0.6	7.5@−0.9	N/A	199 [d]
PtAu$_{37}$(SCH$_2$Ph^{t}Bu)$_{24}$				~80%@−0.6	7.5@−0.9	N/A	
Pt$_2$Au$_{36}$(SCH$_2$Ph^{t}Bu)$_{24}$				~60%@−0.6	14@−0.9	N/A	
Ag$_{4+x}$Au$_{40-x}$(C≡CPh(CH$_3$)$_2$)$_{28}$	0.5 M KHCO$_3$ aq.	H-cell	CO	~98%@−0.5	18@−0.8	10 h@−0.6	310 [d]
Au$_{44}$(C≡CPh(CH$_3$)$_2$)$_{28}$				~75%@−0.5	6@−0.8	10 h@−0.6	
Au$_{44}$(d-MBT)$_{28}$				~80%@−0.5	8@−0.8	10 h@−0.6	
$[Au_{25}(PET)_{18}]^-$	1.0 M KOH aq.	Flow cell or zero-gap cell	CO	~100%@−0.2	~40@−0.2	N/A	190
$[Ag_{25}(SPhMe_2)_{18}]^-$				~95%@−0.6	~50@−0.6	N/A	
$[AuAg_{12}@Au_{12}(PET)_{18}]^-$				~90%@−0.2	~30@−0.2	24 h@−0.5^a	
$[Au_4Pd_6(TBBT)_{12}]^-$	0.5 M KHCO$_3$ aq.	H-cell	CO	88.1%@−0.57	~11@−0.9	65 h@−0.57	202 [b]
$[Au_3AgPd_6(TBBT)_{12}]^-$				94.1%@−0.57	~15@−0.9	65 h@−0.57	
$[Au_{24}Pd(PET)_{18}]^0$	0.1 M KHCO$_3$ aq.	H-cell	CO	~100%@−1.1	35@−1.25	6 h@−0.8	311 [b]
$[Au_{25}(PET)_{18}]^0$				~70%@−1.1	20.3@−1.1	N/A	

PET = phenylethanethiolate, TBBT = 4-*tert*-butylbenzenethiolate, SC$_6$H$_{11}$ = cyclohexanethiolate, SC$_6$H$_{13}$ = 1-hexanethiolate, S-tol = *p*-toluenethiolate, d-MBT = 3,5-dimethylbenzenethiolate, SCH$_2$Ph^{t}Bu = 4-*tert*-butylbenzylthiolate, SPhMe$_2$ = 2,4-dimethylbenzenethiolate. ^{a} *vs.* cell potential. ^{b} Vulcan XC-72R. ^{c} Carbon paper. ^{d} Carbon paper (Toray TGP-H090).

Table 5 Representative references on CRR activity using Au NCs (section 3.3.5 Other effects)

Nanocluster/ nanoparticle	Electrolytes	Electrolyzer	Main product	Selectivity (@V vs. RHE)	Current density (mA cm^{-2}@V vs. RHE)	Stability (@V vs. RHE)	Ref.
$[Au_{25}(PET)_{18}]^-$/Nafion	0.1 M KHCO$_3$ aq.	Two compartment cells	CO	~90%@−0.8	N/A	N/A	312 [a]
$[Au_{25}(PET)_{18}]^-$/PVDF				~55%@−0.8			
Au foil				~4.6%@−0.8			
$[Au_{25}(SC_6H_{13})_{18}]^-$	KOH aq. (1–5 M) or 0.5 M PBS + 0.5 M KCl aq. (pH 8–13)	Flow cell	CO	~95%@−0.4	~100@−0.4	12 h@−1.16	313 [a]

PET = phenylethanethiolate, PVDF = poly vinylidene fluoride. ^{a} Vulcan XC-72R.

0.4 nm when the loading amount was 0.96 μg$_{Au}$ cm$_{geo}^{-2}$, indicating that the initial particle size was approximately maintained. However, aggregates were observed when loading was increased to 15 μg$_{Au}$ cm$_{geo}^{-2}$. With an $[Au_{25}(PET)_{18}]^-$ loading of 0.96 μg$_{Au}$ cm$_{geo}^{-2}$, CO$_2$ flow rate of 50 mL min^{-1}, and applied potential of −1.0 V *vs.* RHE, electrolytic CO$_2$ reduction for 1 h produced 810 ± 11 L g$_{Au}^{-1}$ h^{-1} of CO (FE$_{CO}$ > 90%). Even after 36 h of continuous CO$_2$ reduction by electrolysis, CO production of 7450 ± 59 L g$_{Au}^{-1}$ h^{-1} and an FE$_{CO}$ of approximately 86% was maintained (Fig. 18B). In addition, 1–4 × 10^6 mol$_{CO_2}$ mol$_{catalyst}^{-1}$ of turnover (TON) was obtained after

12 h of CO$_2$ reduction by electrolysis in combination with a 1.5 W, 6 V solar cell or a 6 V solar rechargeable battery.

3.3.1 Size effects in gold nanoclusters. Studies on the size dependence of Au NCs used in electrochemical CRRs are summarized in Table 1. Dass *et al.* evaluated CRR activity by dissolving Au$_{137}$(PET)$_{56}$ in *N,N*-dimethylmethanamide (DMF) containing 0.1 M tetrabutylammonium hexafluorophosphate (Bu$_4$NPF$_6$).[294] They observed a rise in current from ~0.55 V *vs.* NHE, and the overvoltage of CO$_2$ reduction to CO for Au$_{137}$(PET)$_{56}$ was approximately 200 mV lower than that observed for $[Au_{25}(PET)_{18}]^-$.
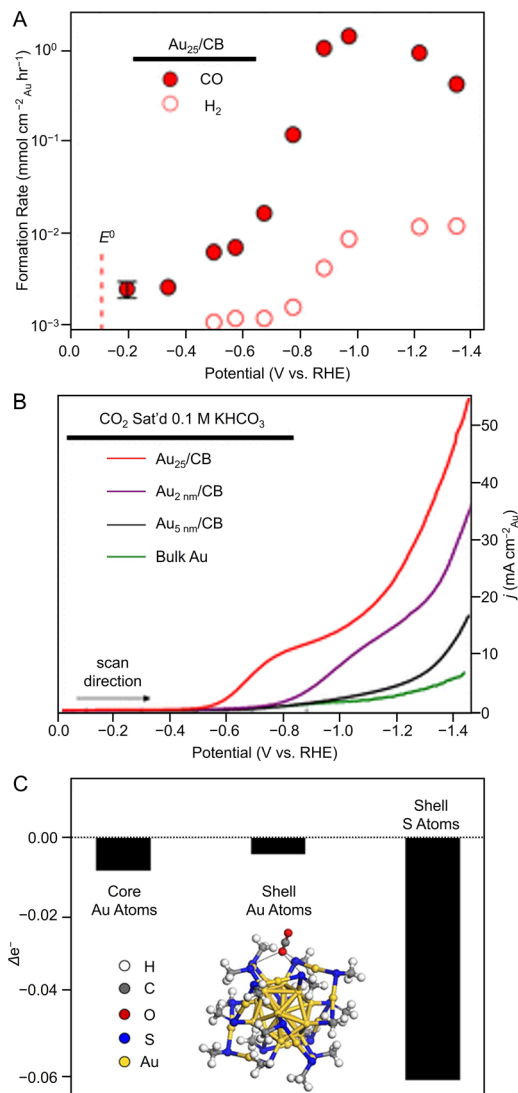
Fig. 17 (A) Potential-dependent H_2 and CO formation rates for Au_{25}/CB. (B) LSVs of various Au catalysts in quiescent CO_2 saturated 0.1 M $KHCO_3$ (pH = 7). (C) DFT model of stable CO_2 adsorption where an O atom of CO_2 interacts with three S atoms in the shell and Bader charge analysis showing the change in Au_{25} valence electrons upon CO_2 adsorption. Panels (A)–(C) are reproduced with permission from ref. 291. Copyright 2012 American Chemical Society.

Fig. 18 (A) TEM images of carbon-supported Au_{25} at low and high loadings. Isolated 1.4 ± 0.4 nm Au NC were observed on the carbon black support at low loadings. (B) Day-to-day (a) product formation rates, (b) cumulative TON (mol of CO/(mol of Au_{25})). Panels (A) and (B) are reproduced with permission from ref. 293. Copyright 2015 American Chemical Society.

In 2021, Lee and Yoo *et al.* evaluated CRR activity using three different core sizes of $Au_n(SR)_m$ (*i.e.*, $[Au_{25}(SC_6H_{13})_{18}]^-$, $[Au_{38}(SC_6H_{13})_{24}]^0$ and $[Au_{144}(SC_6H_{13})_{60}]^0$).[295] As a result, CRR activity increased with decreasing $Au_n(SR)_m$ size, showing much higher CO production current density (j_{CO}) and selectivity (FE_{CO} > 90%) than Au NPs (25 ± 4 nm particle size). Electrochemical measurements, X-ray photoelectron spectroscopy (XPS), and DFT calculations indicated that the application of applied potential in $Au_n(SR)_m$ (n = 25, 38, 144) leads to a progressive de-thiolation and the appearance of an active Au site, which is converted to a more active and stable geometry. Furthermore, it was suggested that Au sites de-thiolated at the staple motif promote CRRs by stabilizing the *COOH intermediate.
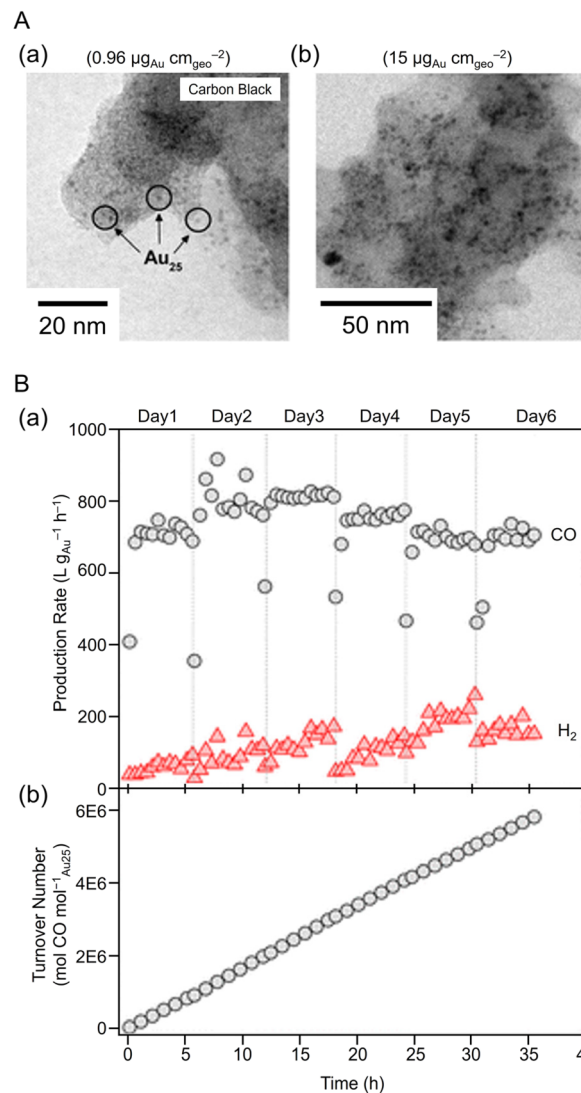
In 2022, Kauffman, Mpourmpakis, and Jin *et al.* used two different $Au_n(SR)_m$ with a series of sizes ($[Au_{38}(PET)_{24}]^0$, $[Au_{144}(PET)_{60}]^0$, $Au_{333}(PET)_{79}$, $[Au_{28}(TBBT)_{20}]^0$, $[Au_{36}(TBBT)_{24}]^0$, and $Au_{279}(TBBT)_{84}$) to evaluate CRR activity.[296] A catalyst ink of each $Au_n(SR)_m$ loaded at 10 wt% in isopropyl alcohol and 0.2 wt% Nafion on CB was placed on GCE, and CRR measurements were performed in 0.5 M potassium hydrogen carbonate ($KHCO_3$) aq. As a result, only CO and H_2 were produced, and the PET-protected $Au_n(SR)_m$ ($[Au_{38}(PET)_{24}]^0$ and $[Au_{144}(PET)_{60}]^0$) and TBBT-protected $Au_n(SR)_m$ ($[Au_{28}(TBBT)_{20}]^0$ and $[Au_{36}(TBBT)_{24}]^0$) showed almost 100% FE_{CO} at potentials more positive than −0.8 V *vs.* RHE and −0.77 V *vs.* RHE, respectively (Fig. 19A). Furthermore, $Au_{333}(PET)_{79}$ and $Au_{279}(TBBT)_{84}$ with larger core sizes showed lower FE_{CO} and j_{co}
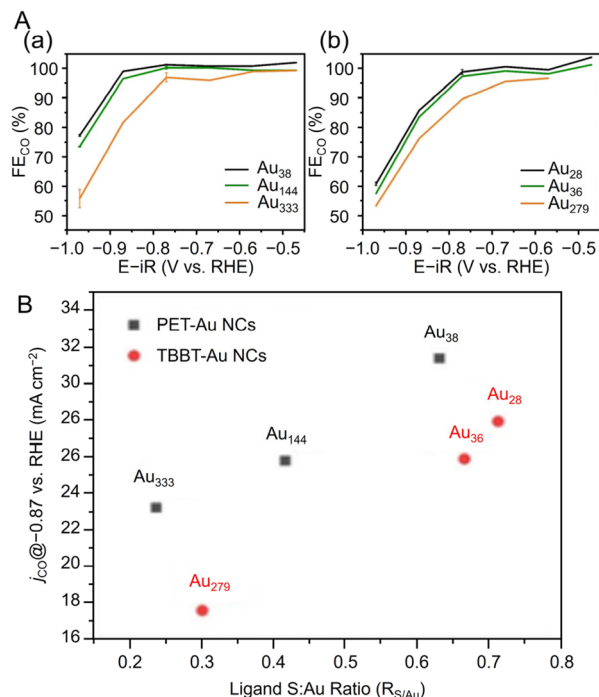
Fig. 19 (A) FE_{CO} of (a) PET-protected Au_{38}, Au_{144} and Au_{333} and (b) TBBT-protected Au_{28}, Au_{36} and Au_{279} NCs. (B) Electrochemical performance: j_{CO} (at −0.87 V vs. RHE) vs. S : Au ratio of Au_{38}, Au_{144}, Au_{333} and Au_{28}, Au_{36}, Au_{279} series of NCs (A) and (B) are reproduced with permission from ref. 296. Copyright 2022 Wiley-VCH GmbH.

values than $Au_n(SR)_m$ with smaller core sizes (Fig. 19A). This size dependence may have been observed because the S atom of the ligand is the CRR active site and the ratio of S atoms to Au atoms ($R_{S/Au}$) is larger for $Au_n(SR)_m$ with a smaller core size (Fig. 19B). The authors also attribute the higher activity of PET-protected $Au_n(SR)_m$ to the difference in ligand conductivity and ligand removal energies compared with TBBT-protected $Au_n(SR)_m$.

In 2023, Sharma, Golovko, and Marshall et al. also reported on the size dependence in CRRs using phosphine-protected Au NCs.[297] The CRR activities of $[Au_6(DPPP)_4](NO_3)_2$, $[Au_9(PPh_3)_8](NO_3)_3$, $[Au_{13}(DPPE)_5Cl_2]Cl_3$, and $[Au_{101}(PPh_3)_{21}]Cl_5$ were measured and showed high selectivity for CO formation (FE_{CO} = 75–90%), and $[Au_{13}(DPPE)_5Cl_2]Cl_3$ showed slightly higher CO selectivity compared with other NCs. Additionally, the calcination process for ligand removal was found to cause aggregation of the Au NCs, thus decreasing the CO selectivity. It was also reported that Au4 clusters ($Au_4(PPh_3)_4I_2$) stabilized by phosphine and iodide (I) show higher CO selectivity (FE_{CO} = >60%) than $Au_{11}(PPh_3)_7I_3$ (FE_{CO} = <60%).[298]

From these reports, the size reduction of Au NCs contributes to the improvement of CRR activity and selectivity. This is probably due to the increase in active sites to increase in specific surface area and the change in the electronic state of metal NCs, which is advantageous for CO_2 adsorption.

3.3.2 Structure effects in gold nanoclusters. Studies on the structure dependence of electrochemical CRRs using Au NCs

are summarized in Table 2. The geometric structure of metal NCs can have a significant effect on CRR activity. Mpourmpakis and Jin et al. evaluated the CRR activity of $[Au_{25}(PET)_{18}]^-$, a spherical form, and $[Au_{25}(PPh_3)_{10}(PET)_5Cl_2]^{2+}$, a rod form (Fig. 20A).[299] $Au_n(SR)_m$ loaded at 10 wt% on CB was dropped on GCE (Fig. 20B) and electrochemical measurements were performed in 0.5 M $KHCO_3$ aq. saturated with CO_2. The FE_{CO} of $[Au_{25}(PET)_{18}]^-$ was 73.7% at −0.57 V vs. RHE, 1.63 times higher than that of $[Au_{25}(PPh_3)_{10}(PET)_5Cl_2]^{2+}$ (FE_{CO} = ~28.0%) (Fig. 20C). The FE_{CO} of $[Au_{25}(PET)_{18}]^-$ was also high, 73.5% at −1.07 V vs. RHE, indicating that H_2 formation is suppressed. From the DFT calculations, they speculated that this high selectivity is due to the energetically advantageous ligand desorption that exposes the active site, and the negatively charged $[Au_{25}(PET)_{18}]^-$ is presumed to be favorable for stabilization of the adsorbed intermediate COOH (Fig. 20D). Although these NCs cannot be directly compared because they have different
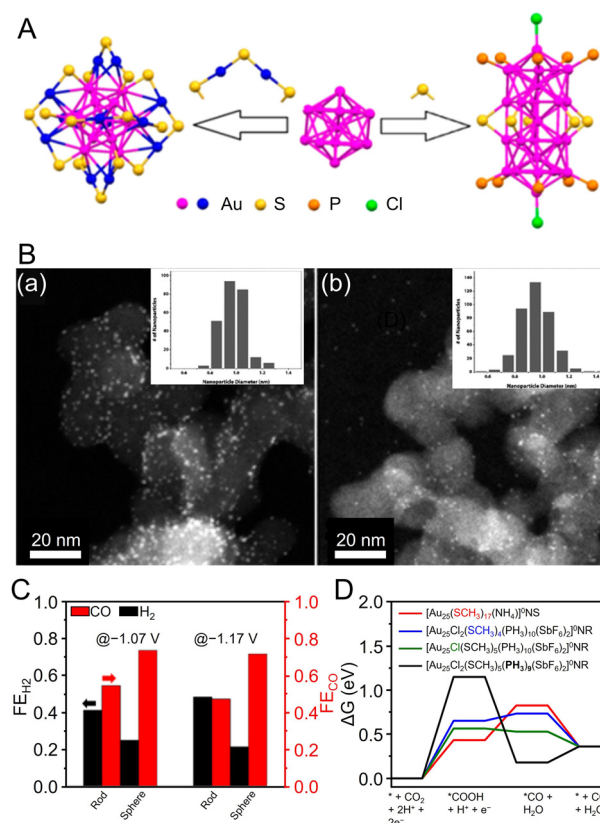

Fig. 20 (A) Atom packing structures of Au_{25} nanosphere ($[Au_{25}(PET)_{18}]^-$) and nanorod ($[Au_{25}(PPh_3)_{10}(PET)_5Cl_2]^{2+}$). (B) STEM images and particle size histograms of (a) Au_{25} nanosphere and (b) nanorod supported on carbon black. (C) FE_{CO} and FE_{H_2} at the potential of −1.07 and −1.17 V over Au_{25} nanosphere and nanorod, respectively. (D) Free energy diagrams (ΔG) for CO_2 reduction to CO on the ligand-removed NCs at 0 V vs. RHE. The black, blue, green, and red lines represent CO_2 reduction to CO on the nanorod with PH_3 removed, the nanorod with $-SCH_3$ removed, the nanorod with $-Cl$ removed, and on the nanosphere with $-SCH_3$ removed, respectively. Panels (A)–(D) are reproduced with permission from ref. 299. Copyright 2018 American Chemical Society.

ligands, the results demonstrated that the structure of the active site where the substrate is adsorbed is important.

In 2022, Kauffman, Mpourmpakis, and Jin *et al.* evaluated CRR activity using two structural isomers of Au$_{38}$(PET)$_{24}$ (Fig. 4A; Au$_{38}$Q and Au$_{38}$T).[296] Au$_{38}$Q exhibited an FE$_{CO}$ of 87% at −0.97 V *vs.* RHE, and Au$_{38}$T exhibited a lower FE$_{CO}$ than Au$_{38}$Q, especially at more negative potentials (67% at −0.97 V *vs.* RHE). Thus, they investigated the differences in these activities based on DFT calculations. As a result, the average thermodynamic barrier to ligand removal (exposed active site) was similar for the two Au$_{38}$(PET)$_{24}$. However, there are significant differences in the average *COOH formation energies, indicating a linear trend between the *COOH formation energy and the ligand removal energy. Specifically, the average *COOH production energy at the two S sites for Au$_{38}$Q is 0.17 eV, compared with 0.31 eV for Au$_{38}$T. This indicates that the differences in CRR activity between the two isomers may be due to differences in the ease of *COOH formation. Overall, two Au$_{38}$(PET)$_{24}$ with the same size, composition, and number of ligands can have substantially different catalytic selectivity and activities if their underlying structures are different, which can affect the formation energies.

Asymmetric structural defects of metal NCs can induce enhanced activity. Using Au$_{44}$(PPh$_3$)(TBBT)$_{26}$ and Au$_{44}$(PPh$_3$)$_2$(TBBT)$_{24}$ with fcc metal cores co-protected by PPh$_3$ and TBBT, and Au$_{44}$(TBBT)$_{28}$, changes in CRR activity due to ligand defects have also been reported. Au$_{44}$(PPh$_3$)(TBBT)$_{26}$ with a single Au atom at the bottom of the fcc lattice exhibited high CO selectivity. DFT calculations showed that this active site promotes the electrochemical reduction of CO$_2$ to CO by lowering the free energy of *COOH formation.[300]

From this report, even in Au NCs composed of the same chemical composition, the adsorption energy with the CRR intermediate changes due to the difference in the geometric structure, and Au NCs with different geometries showed different CRR activities.

3.3.3 Ligand effects in gold nanoclusters.
Studies on the ligand dependence of electrochemical CRRs with Au NCs are summarized in Table 3. Kauffman, Mpourmpakis, and Jin *et al.* compared the activity of CRRs using [Au$_{25}$(SR)$_{18}$]$^−$ protected by three different ligands (PET, SNap, and benzeneselenolate (SePh)).[301] They found that changes in the carbon tail do not significantly affect catalytic selectivity, but the anchoring atom of the ligand binding to Au (X = S/Se) has a strong effect on both selectivity and activity. As a result, [Au$_{25}$(SR)$_{18}$]$^−$ exhibited higher CO selectivity than [Au$_{25}$(SeR)$_{18}$]$^−$. According to DFT calculations, they ascribed the higher selectivity of [Au$_{25}$(SR)$_{18}$]$^−$ to the enhanced electronic interaction between the reaction intermediates and the exposed S active site compared with the Se site. This was interpreted as an increase in the electron density of the S site in [Au$_{25}$(SR)$_{18}$]$^−$, changing the bonding properties of the reaction intermediates and decreasing the energy penalty between COOH and CO.

In 2022, Wang, Zang, and Mak *et al.* studied the effect of the protective ligand on the CRR activity using [Au$_{28}$(C$_2$B$_{10}$H$_{11}$S)$_{12}$(THT)$_4$Cl$_4$]^0 (THT = tetrahydrothiophe)

(Au$_{28}$–S) and [Au$_{28}$(C$_4$B$_{10}$H$_{11}$)$_{12}$(THT)$_8$]$^{3+}$ (Au$_{28}$–C),[302] which have the same metal core but different ligand shells.[303] As shown in Fig. 21A, Au$_{28}$–S and Au$_{28}$–C have almost the same Au core structure, but the ligand group of the carborane ligand changes from a C≡CR group (σ–π donor) to an SR group (σ donor), and the four THT ligands in Au$_{28}$–C are replaced by four Cl ions in Au$_{28}$–S. As a result, the total numbers of valence electrons in Au$_{28}$–C and Au$_{28}$–S are 12e$^−$ and 13e$^−$, respectively. As shown in Fig. 21B, Au$_{28}$–S exhibited higher CRR catalytic activity than Au$_{28}$–C. Au$_{28}$–S exhibited a maximum FE$_{CO}$ of 98.5% at −0.9 V *vs.* RHE, approximately 1.4 times that of Au$_{28}$–C. Furthermore, time-resolved *in situ* Fourier transform infrared (FT-IR) spectroscopy showed that the vibrational peak V(C–O) at 1362 cm^{-1} and the C≡O stretch at 1636 cm^{-1} of the *COOH intermediate in Au$_{28}$–S is stronger than that of Au$_{28}$–C, confirming that Au$_{28}$–S exhibits higher electrocatalytic activity. In addition, they used DFT calculations to determine the active sites. The Au atom in the linear C$_2$B$_{10}$H$_{11}$C≡C–Au–C≡CC$_2$B$_{10}$H$_{11}$ staple of Au$_{28}$–C has enough space between the two C≡CR groups to access the CO$_2$ molecule, but in Au$_{28}$–S, the Cl atom of the surface ligand is
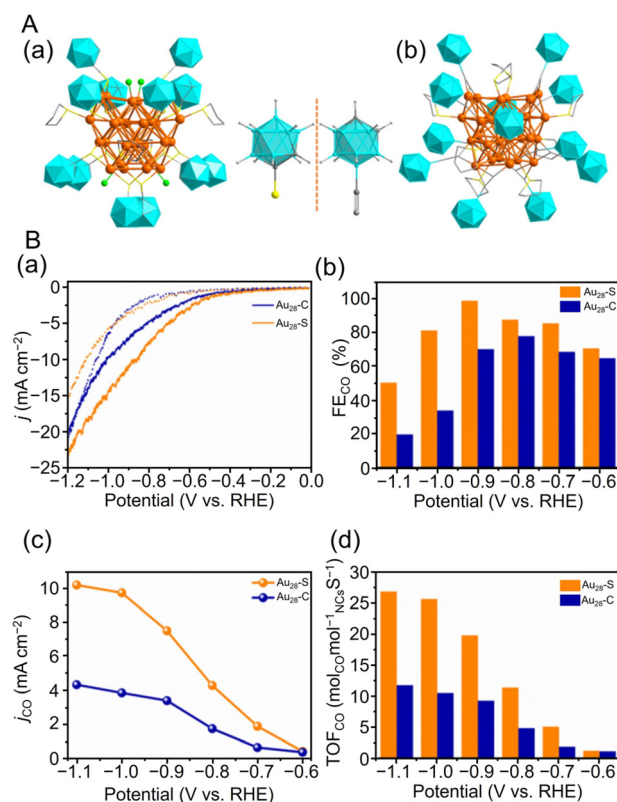
Fig. 21 (A) The total crystal structures of (a) Au$_{28}$–S and (b) Au$_{28}$–C. (B) (a) Linear sweep voltammetry (LSV) curves of Au$_{28}$–S and Au$_{28}$–C in a N$_2$-saturated (dotted line) and a CO$_2$-saturated (full line) 0.5 M KHCO$_3$ solution. (b) FE$_{CO}$ at various applied potentials over two NCs. (c) The j_{CO} and (d) TOF$_{CO}$ at the potential of −0.6 to −1.1 V *vs.* RHE of two NCs. Color codes: orange, green and blue = gold turquoise icosahedrons = carborane; yellow = sulfur; gray = carbon; bright green = chloride. Hydrogen atoms are omitted for clarity. (A) and (B) are reproduced with permission from ref. 303. Copyright 2022 Wiley-VCH GmbH.

removed, and the CO_2 molecule is not accessible until the Au atom is exposed. The Gibbs free energy calculations of the CRRs for Au_{28}–S and Au_{28}–C and the time-resolved *in situ* FT-IR results indicate that the pathway of CO_2 reduction to CO is $CO_2(g) \rightarrow *CO_2^- \rightarrow *COOH \rightarrow *CO \rightarrow CO(g)$, with the rate-limiting step being *COOH formation. Notably, Au_{28}–S is energetically more favorable for CO formation than Au_{28}–C.

Häkkinen, Tsukuda, and Crudden *et al.* reported on the electrocatalytic activity for CO_2 reduction using NHC-co-ordinated Au_{11} clusters.[238] Specifically, $[Au_{11}(PPh_3)_7(NHC^{Me})Cl_2]Cl$ (NHC^{Me} = 1,3-dihydro-1,3-dimethyl-$2H$-benzimidazol-2-ylidene) showed higher stability and CRR mass activity than $[Au_{11}(PPh_3)_8Cl_2]Cl$. The activity was greatly enhanced when the PPh_3 ligand was removed by heating the catalyst at 180 °C for 2 h during catalyst preparation. In 2022, Häkkinen, Tsukuda, and Crudden *et al.* also reported on the electrocatalytic activity of CRRs with NHC-protected Au_{24} clusters.[249] Fig. 22A shows the ESI-MS spectrum of $[Au_{24}(NHC^{Bn})_{14}Cl_2H_3][TFA]_3$ (TFA = tri-fluoroacetate; NHC^{Bn} = 1,3-dibenzyl-$1H$-benzo[d]imidazol-2-ylidene) and its geometric structure. $[Au_{24}(NHC^{Bn})_{14}Cl_2H_3]^{3+}$

Fig. 22 (A) (a) ESI-MS spectra and (b) molecular structure of $[Au_{24}(NHC^{Bn})_{14}Cl_2H_3][TFA]_3$ as determined by SC-XRD with hydrogen atoms and TFA anions omitted for clarity. (B) (a) FE_{CO} and FE_{H_2} at different current densities. (b) Cell voltage *vs.* current density. (C) Stability of FE_{CO} and FE_{H_2}, and cell voltage *vs.* time at an operating current density of 100 mA cm^{-2} with the Au_{24} catalyst. Color codes: yellow = gold; green = chloride; grey = carbon; and blue = nitrogen. (A)–(C) are reproduced with permission from ref. 249. Copyright 2022 American Chemical Society.

exhibited a high FE_{CO} of >90% in the current density range of 10 to 50 mA cm^{-2} and higher CO selectivity than commercial Ag NP catalysts and $[Au_{13}(NHC^{Bn})_9Cl_3]^{2+}$ NCs[304] (Fig. 22B). The CRR evaluation at a steady current density of 100 mA cm^{-2} showed that the FE_{CO} and full cell voltage remained stable at approximately 90% and 3.2 V, respectively, even after 100 h, demonstrating the high stability of $[Au_{24}(NHC^{Bn})_{14}Cl_2H_3]^{3+}$ (Fig. 22C).

In 2021, Wang *et al.* synthesized the first all-amidinate-protected Au NC, $[Au_{28}(Ph\text{-}form)_{12}]^{2+}$, and evaluated its CRR activity.[250] The crystal structure of $[Au_{28}(Ph\text{-}form)_{12}]^{2+}$ has a core–shell Au_{28} kernel consisting of a tetrahedral Au_4 core and a twisted truncated tetrahedral Au_{24} shell (Fig. 8C). Unlike Au NCs protected by SR and C≡CR, $[Au_{28}(Ph\text{-}form)_{12}]^{2+}$ does not have a staple. After loading $[Au_{28}(Ph\text{-}form)_{12}]^{2+}$ at 10 wt% on multiwalled carbon nanotubes (CNTs), the CRR activity was evaluated, and the highest FE_{CO} was 96.5% at −0.57 V *vs.* RHE. These values were higher than those observed for Ph-form Au/CNT and polyvinylpyrrolidone (PVP)-coated Au NPs. In addition, stable potentials at approximately −0.69 V *vs.* RHE and an FE_{CO} of >90% were maintained for 40 h in the long-term activity evaluation at −3.5 mA cm^{-2}. The high stability is attributed to the strong bonding between Au and amidinate ligands, indicating that Au NCs protected by N-containing ligands, such as NHCs and amidinates, can be used as highly stable and active CRR catalysts.

In 2021, Wang *et al.* synthesized $[Au_{55}(p\text{-}MBT)_{24}(PPh_3)_6]^{3+}$, which is co-protected with SR and phosphine and has the fcc structure, and evaluated its CRR activity.[233] As a result, $[Au_{55}(p\text{-}MBT)_{24}(PPh_3)_6]^{3+}$ showed the highest FE_{CO} of 94.1% at −0.6 V *vs.* RHE. The Au_{55} core in $[Au_{55}(p\text{-}MBT)_{24}(PPh_3)_6]^{3+}$ is fcc aligned and consists of four layers stacked in ABCA order along the [111] direction. Moreover, $[Au_{55}(p\text{-}MBT)_{24}(PPh_3)_6]^{3+}$ may have shown higher CRR activity than the Au NPs with an fcc structure because of the protection of the HER-active corner by the p-MBT, which is a hydrophobic ligand. Thus, CRR activity may be controlled by the appropriate selection of surface ligands.

In 2022, Wang *et al.* investigated the effect of uncoordi-nated metal sites in CRRs using $[Au_{11}(DPPE)_5]^{3+}$ and a hydride-coordinated Au NC ($[Au_{22}H_3(DPPE)_3(PPh_3)_8]^{3+}$).[231] They presume that $[Au_{11}(DPPE)_5]^{3+}$ is completely capped with a diphosphine ligand, whereas $[Au_{22}H_3(DPPE)_3(PPh_3)_8]^{3+}$ has three H atoms bridging six uncoordinated Au sites, and the remaining 14 surface Au atoms are protected with PPh_3 ligands. They evaluated the CRR activities and found that compared with $[Au_{11}(DPPE)_5]^{3+}$, $[Au_{22}H_3(DPPE)_3(PPh_3)_8]^{3+}$ exhibited higher FE_{CO} (92.7% at −0.6 V *vs.* RHE), TOF_{CO} (488 h^{-1}), and mass activity (134 A g_{Au}^{-1}). Furthermore, $[Au_{22}H_3(DPPE)_3(PPh_3)_8]^{3+}$ was found to have high stability, with little change in j_{CO} and FE_{CO} after more than 10 h of reaction at −0.6 V *vs.* RHE. The results of DFT calculations suggest that the hydride-coordinated Au atoms in $[Au_{22}H_3(DPPE)_3(PPh_3)_8]^{3+}$ are the active sites, and the bridge H atoms directly hydrogenate CO_2 to adsorbed *COOH. Moreover, it was estimated that the H voids are easily recovered
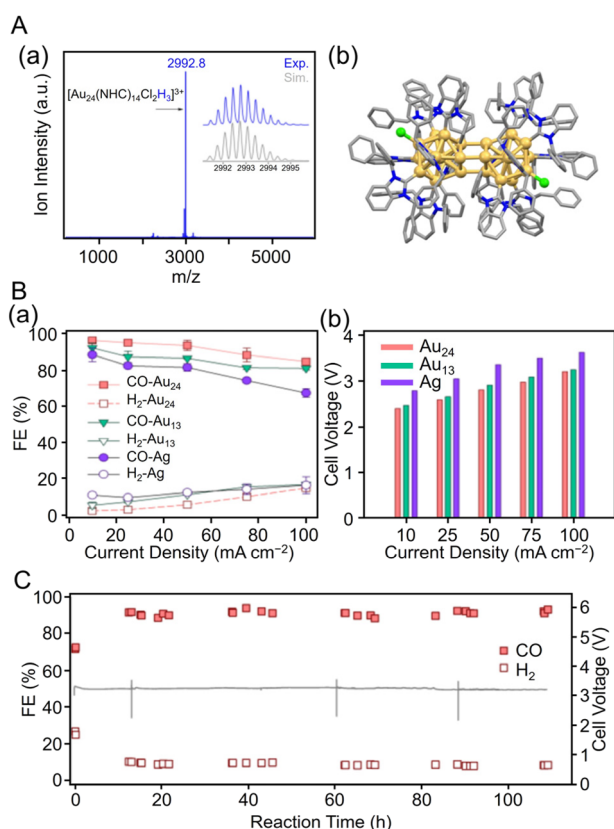
by proton reduction, thus completing the catalytic cycle. These findings suggest that Au–H bonds can improve the stability and CRR catalytic activity of Au NCs.

Pei and Wang *et al.* evaluated the CRR activity for $[Au_7(PPh_3)_7H_5]^{2+}$ with hydride ligands and $[Au_8(PPh_3)_7]^{2+}$ synthesized by degrading $[Au_7(PPh_3)_7H_5]^{2+}$ using light (300–450 nm) irradiation.[232] As a result, $[Au_7(PPh_3)_7H_5]^{2+}$ showed high selectivity for HER (max FE_{H_2} = 98.2% at −0.67 V *vs.* RHE; FE_{H_2} = FE of H_2 generation), whereas $[Au_8(PPh_3)_7]^{2+}$ was highly selective for CRR (FE_{CO} = 73.5% at −0.77 V *vs.* RHE). UV/Vis and ESI-MS measurements of $[Au_7(PPh_3)_7H_5]^{2+}$ and $[Au_8(PPh_3)_7]^{2+}$ before and after CRRs did not change significantly, indicating their stability. In addition, isotope labeling experiments with deuterium indicated that all the constituent hydrogen atoms of H_2 released during the CO_2 reduction process came from the aqueous solution (H_3O^+) and not from hydrides in the NC. Notably, $[Au_{22}H_3(DPPE)_3(PPh_3)]^{3+}$,[231] protected by hydride ligands, showed high CO selectivity, unlike $[Au_7(PPh_3)_7H_5]^{2+}$, indicating that the reactions between these NCs proceeded *via* different mechanisms. Therefore, assuming that all the hydrogen atoms come from the aqueous solution and not from the hydride ligands, DFT calculations showed that the values of ΔG of the *COOH formation for $[Au_7(PPh_3)_7H_5]^{2+}$ and $[Au_8(PPh_3)_7]^{2+}$ are 1.68 and 0.58 eV, respectively. The small potential barrier to COOH* formation might be responsible for the high CO selectivity of $[Au_8(PPh_3)_7]^{2+}$.

In 2021, Yang *et al.* investigated the process of ligand removal by thermal and electrochemical treatment of $Au_{25}(PET)_{18}$ and its effect on the electrolytic reduction of CO_2 to CO.[305] Under-potential deposition (UPD) measurements of Cu, Au L_3 edge X-ray absorption fine structure (EXAFS) spectroscopy, and XPS measurements were used to determine the extent of ligand removal. Increasing the annealing temperature during the thermal treatment and the bias voltage in the electrochemical treatment increased the surface area on the catalyst, indicating that the Au–S bonds were broken, and the surface Au atoms became metallic. In particular, when the reducing potential was applied by electrochemical treatment, there was no change in the Au–S bond strength measured by Cu UPD and FT-EXAFS measurements up to −0.30 V *vs.* RHE, but from −0.35 V *vs.* RHE ligand, removal was observed, and the aggregation of $Au_{25}(PET)_{18}$ was observed in the TEM images after applying a higher reducing potential. For the electrochemical evaluation of CRR activity, S-doped graphene (S–G)-loaded $Au_{25}(PET)_{18}$ ($Au_{25}(PET)_{18}$/S–G) annealed at 150 °C (Au_{25}/S–G(Thermal)), and electrochemically pretreated $Au_{25}(PET)_{18}$/S–G at −0.8 V *vs.* RHE (Au_{25}/S–G(Electrochemical)) were used. Au_{25}/S–G(Electrochemical) exhibited a higher FE_{CO} (82% at −0.59 V *vs.* RHE) than Au_{25}/S–G(Thermal). This suggests that ligand removal by thermal and electrochemical pretreatment exposed Au atoms as active sites and improved the CRR catalytic activity.

From these papers, regarding the influence of ligands, it was revealed that (1) the CRR activity changes greatly depending on the element that directly coordinates with the metal

(electron-withdrawing or donating ligands), (2) high CRR stability by using ligands with strong binding energy with metals, (3) the hydride contained in the ligand also affects the CRR activity, and (4) elimination of some ligands promotes the CRR activity.

3.3.4 Doping effects in gold nanoclusters. In Table 4, we summarized the studies on electrochemical CRR using heterometal-doped Au NCs. In 2019, Yang and Wu *et al.* reported on CRRs using $Au_{47}Cd_2(TBBT)_{31}$ and $Au_{44}(TBBT)_{28}$.[211,306] Fig. 23A (inset) shows the structure of $Au_{47}Cd_2(TBBT)_{31}$, which consists of an Au_{29} kernel, two $Cd(S–Au–S)_3$, three $Au_2(TBBT)_3$, one $Au_3(TBBT)_4$, and three $Au(TBBT)_2$ staple motifs in the shell structure. $Au_{47}Cd_2(TBBT)_{31}$, $Au_{44}(TBBT)_{28}$, or Au NPs were loaded on GCE and examined by linear sweep voltammetry (LSV) in 0.5 M $KHCO_3$ aq. saturated with Ar or CO_2. All catalysts exhibited higher current densities in a CO_2 atmosphere
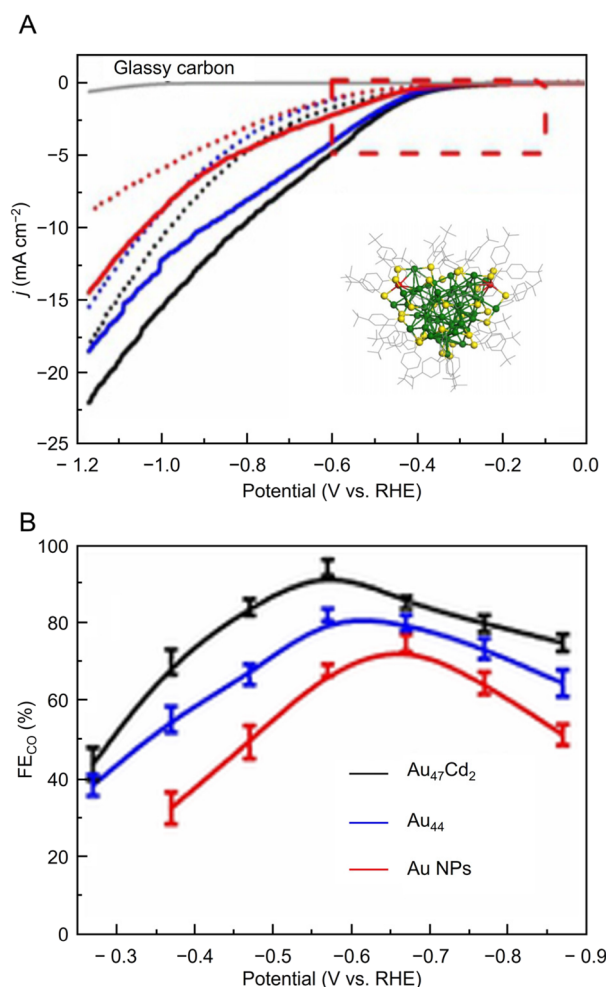

Fig. 23 (A) LSV curves of $Au_{47}Cd_2(TBBT)_{31}$, $Au_{44}(TBBT)_{28}$ and the *ca.* 1.5 nm Au NPs in an Ar-saturated (dotted line) and a CO_2-saturated (full line) 0.5 M $KHCO_3$ solution; inset: total structure of the $Au_{47}Cd_2(TBBT)_{31}$. Color labels: yellow = S; gray = C; red = Cd, others = Au. (B). FE_{CO} for the catalysts examined with different applied potentials. Panels (A) and (B) are reproduced with permission from ref. 306. Copyright 2019 Wiley-VCH Verlag GmbH & Co. KGaA, Weinheim.

than in an Ar atmosphere, indicating that electrocatalytic CRRs occurred (Fig. 23A). Notably, $Au_{47}Cd_2(TBBT)_{31}$ exhibited the highest current density. The maximum values of FE_{CO} at -0.57 V *vs.* RHE were 96% and 83% for $Au_{47}Cd_2(TBBT)_{31}$ and $Au_{44}(TBBT)_{28}$, respectively. In comparison, 1.5 nm Au NPs exhibited a maximum FE_{CO} of 76% at -0.67 V *vs.* RHE (Fig. 23B). At a constant applied voltage (-0.57 V *vs.* RHE), the j_{CO} reached -3.2 mA cm^{-2} for $Au_{47}Cd_2(TBBT)_{31}$, which was higher than that of $Au_{44}(TBBT)_{28}$ (-1.6 mA cm^{-2}). In $Au_{47}Cd_2(TBBT)_{31}$, the FE_{H2} in HER was 3.8% at -0.57 V *vs.* RHE, indicating that the HER was effectively suppressed. Furthermore, the Tafel slope was lower for $Au_{47}Cd_2(TBBT)_{31}$ at 151 mV per decade, compared with $Au_{44}(TBBT)_{28}$ (166 mV per decade) and Au NPs (203 mV per decade). These results indicated that $Au_{47}Cd_2(TBBT)_{31}$ favored the formation of the *COOH species by the first electron transfer. Subsequently, they used DFT calculations to examine the reaction mechanism. Cd prefers to bond with oxygen (O) atoms, forming Cd–O–C(OH)–Au to stabilize the intermediate *COOH. As a result, the formation of *COOH in $Au_{44}(TBBT)_{28}$ and Au NPs causes an increase in free energy, whereas the formation of COOH* in $Au_{47}Cd_2(TBBT)_{31}$ causes the release of free energy (0.39 eV), which favors the formation of intermediates. The DFT calculations also revealed that the release of H_2 in $Au_{47}Cd_2(TBBT)_{31}$ was the most difficult of the three systems. Overall, the doped NC, $Au_{47}Cd_2(TBBT)_{31}$, exhibited enhanced CRR activity.

Kauffman, Mpourmpakis, and Jin *et al.* used $[Au_{19}Cd_2(SC_6H_{11})_{16}]^-$ and $[Au_{23}(SC_6H_{11})_{16}]^-$ (ref. 206 and 307) to compare CRR activity.[308] For $[Au_{19}Cd_2(SC_6H_{11})_{16}]^-$, the CO selectivity of the CRR was ~90–95% at applied potentials of -0.5 to -0.9 V *vs.* RHE, approximately twice that of $[Au_{23}(SC_6H_{11})_{16}]^-$. From the DFT calculations, similar to the previous study,[16] it is thermodynamically preferable to remove the –R group from the NCs, compared with the –SR group. Therefore, they simplified the ligand to SCH_3 and calculated the reaction free energy pathways using the two NCs, but with one ligand's R site removed ($[Au_{19}Cd_2S(SCH_3)_{15}]^-$ and $[Au_{23}S(SCH_3)_{15}]^-$). The thermodynamic energy barrier for CO formation was 0.74 eV lower for $[Au_{19}Cd_2S(SCH_3)_{15}]^-$ compared with $[Au_{23}S(SCH_3)_{15}]^-$. In addition, comparing the thermodynamic limiting steps of CRR and HER, the calculated results were consistent with the experimental data showing that $[Au_{19}Cd_2S(SCH_3)_{15}]^-$ has a higher CRR selectivity. The effect of solvation was also examined, and it was found that the solvent (water) only had a minimal effect on the reaction energy. These results showed that modifying both the NC surface morphology and electronic structure by Cd doping can significantly enhance CRR activity.

In 2021, Zhu and Chen *et al.* synthesized $Au_{25}(PET)_{18}$, $Au_{24}Cd(PET)_{18}$, $Au_{19}Cd_3(S\text{-tol})_{18}$, and $Au_{38}Cd_4(d\text{-MBT})_{30}$ and investigated the effect of different substitution positions of Cd doping on the catalytic CRR activity.[188] As shown in Fig. 3Ba,
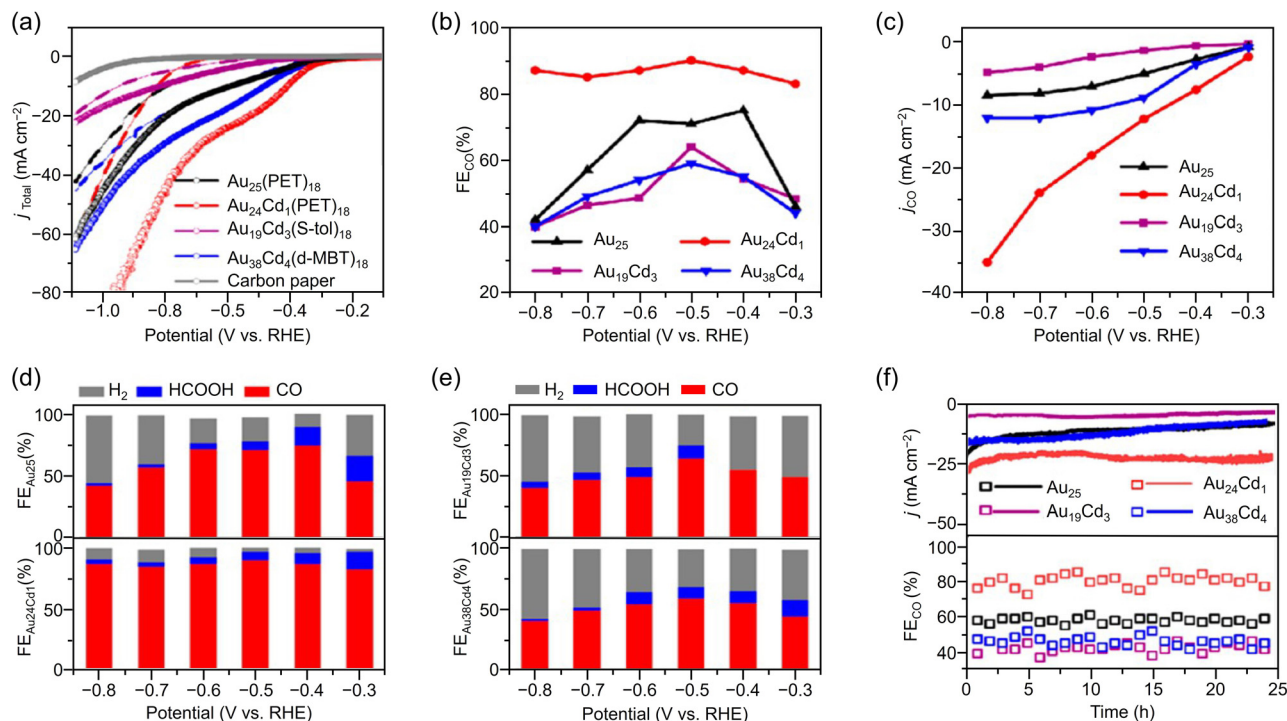

Fig. 24 (a) LSV curves of $Au_{25}(PET)_{18}$, $Au_{24}Cd_1(PET)_{18}$, $Au_{19}Cd_3(S\text{-tol})_{18}$ and $Au_{38}Cd_4(d\text{-MBT})_{30}$ under an Ar-saturated (dotted line) and a CO_2-saturated (full line) in 1.0 M $KHCO_3$ solution. (b) FE_{CO} for the catalysts examined with different applied potentials. (c) The corresponding j_{CO}. (d) FEs for various CRR products obtained on $Au_{25}(PET)_{18}$ and $Au_{24}Cd_1(PET)_{18}$ catalysts. (e) FEs for various CRR products obtained on $Au_{19}Cd_3(S\text{-tol})_{18}$ and $Au_{38}Cd_4(d\text{-MBT})_{30}$ catalysts. (f) The stability test conducted at -0.7 V *vs.* RHE for $Au_{25}(PET)_{18}$, $Au_{24}Cd_1(PET)_{18}$, $Au_{19}Cd_3(S\text{-tol})_{18}$ and $Au_{38}Cd_4(d\text{-MBT})_{30}$ catalysts. These figures are reproduced with permission from ref. 188. Copyright 2021 American Chemical Society.

the Cd atoms in $Au_{24}Cd(PET)_{18}$ replaced the Au atoms located in the core–shell layer, and the Cd atoms in $Au_{19}Cd_3$(S-tol)$_{18}$ and $Au_{38}Cd_4$(d-MBT)$_{30}$ substituted the Au atoms on the shell staples. Among these four NCs, $Au_{24}Cd(PET)_{18}$ showed the highest current density, FE_{CO}, and j_{CO}, whereas $Au_{19}Cd_3$(S-tol)$_{18}$ showed the lowest CRR activity (Fig. 24a–c). Fig. 24d and e shows that a small amount of HCOOH was detected in addition to the main product of CO, for all NCs. Furthermore, the stability measurements in Fig. 24f show that $Au_{24}Cd$(PET)$_{18}$ and $Au_{19}Cd_3$(S-tol)$_{18}$ were highly stable, with no significant change in current density after 24 h. DFT calculations showed that removing the carbon chain on the NC surface (S–C cleavage) was advantageous for CRR, as observed in previous studies,[16] and exposing the Au site by Au–S cleavage was advantageous for HER. From these results, it was speculated that only S–C cleavage occurs in $Au_{24}Cd(PET)_{18}$ and that the HER was suppressed by avoiding Cd–S cleavage, resulting in a high FE_{CO}. These results showed that the CRR activity can be enhanced by controlling the surface state through doping to different sites.

In 2021, Lim, Yoo, and Lee et al. investigated the effect of Pt doping on CRR activity using $[Au_{25}(SC_6H_{13})_{18}]^-$ and $[PtAu_{24}(SC_6H_{13})_{18}]^0$.[309] $[PtAu_{24}(SC_6H_{13})_{18}]^0$ has a central atom of $[Au_{25}(SC_6H_{13})_{18}]^-$ replaced by Pt, but otherwise, the overall structures are very similar (Fig. 3A). Comparing the electrocatalytic performance, $[PtAu_{24}(SC_6H_{13})_{18}]^0$ was found to promote HER more than CRR, compared with $[Au_{25}(SC_6H_{13})_{18}]^-$ (Fig. 25a and b). As shown in Fig. 25c and d, in the 0.3–0.6 V vs. RHE range where CO formation is not controlled by the solubility of CO_2, the FE_{CO} of $[Au_{25}(SC_6H_{13})_{18}]^-$ was >95%, but $[PtAu_{24}(SC_6H_{13})_{18}]^0$ showed FE_{H_2} = ~80% at 0.4 V vs. the RHE. They also obtained a synthesis gas with a controlled H_2/CO molar ratio of 1 to 4 by mixing $[Au_{25}(SC_6H_{13})_{18}]^-$ and $[PtAu_{24}(SC_6H_{13})_{18}]^0$ on the gas diffusion electrode (GDE) with an appropriate mass ratio (Fig. 25e). Additionally, DFT calculations for the CRR and HER processes were performed with SC_6H_{13} replaced by SCH_3 for simplicity. As a result, the HER with $[PtAu_{24}(SCH_3)_{18}]^0$ was found to have an almost ideal *H bonding energy, which is favorable for HER. For $[Au_{25}(SCH_3)_{18}]^-$, the reaction is more active for the CRR because the limiting potential of the CRR (0.09 eV) is higher than that of the HER (0.32 eV). Therefore, it was revealed that the CRR is more likely to proceed for $[Au_{25}(SC_6H_{13})_{18}]^-$ and the HER is more likely for $[PtAu_{24}(SC_6H_{13})_{18}]^0$.

In 2022, Zhou, Gao, and Zhu et al. synthesized $[Au_{38}(SCH_2Ph^tBu)_{24}]^0$, $[PtAu_{37}(SCH_2Ph^tBu)_{24}]^0$, and $[Pt_2Au_{36}(SCH_2Ph^tBu)_{24}]^0$ with Pt doping of one or two atoms and investigated the effect of the Pt atomic position and number on the CRR catalytic activity.[199] SC-XRD analysis revealed that $[Au_{38}(SCH_2Ph^tBu)_{24}]^0$ consists of a 23-atom kernel composed of two 13-atom icosahedra sharing one triangular plane, three Au(SR)$_2$ staples around the icosahedra, and six Au_2(SR)$_3$ staples (Fig. 4B and 26A). In addition, theoretical calculations and X-ray absorption fine structure analysis suggested that the position of Pt in $[PtAu_{37}(SCH_2Ph^tBu)_{24}]^0$ and $[Pt_2Au_{36}(SCH_2Ph^tBu)_{24}]^0$ is at the center of the icosahe-
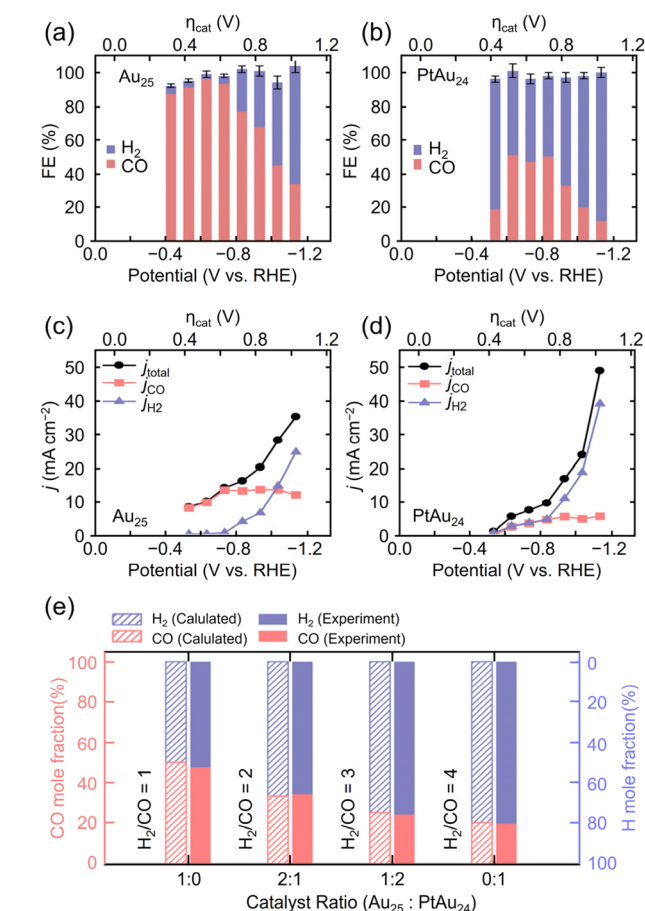
Fig. 25 Results of FE_{CO} and FE_{H_2} measured on the (a) Au_{25}/C/GDE and (b) $PtAu_{24}$/C/GDE in the CO_2-saturated solution of 0.1 M KHCO$_3$ and 0.4 M KCl at various applied potentials. The corresponding j_{total}, j_{CO}, and j_{H_2} obtained on the (c) Au_{25}/C/GDE and (d) $PtAu_{24}$/C/GDE at various potentials. (e) Calculated (shaded) and experimentally determined (filled) H_2/CO ratio on formulated Au_{25} and $PtAu_{24}$ catalysts. These figures are reproduced with permission from ref. 309. Copyright 2021 AIP Publishing.

dron. From time-dependent DFT (TDDFT) calculations, $[PtAu_{37}(SH)_{24}]^0$ has one less total electron than $[Au_{38}(SH)_{24}]^0$, and the highest occupied molecular orbital (HOMO) energy increases. In contrast, in $[Pt_2Au_{36}(SH)_{24}]^0$, the total number of electrons is decreased by two compared with $[Au_{38}(SH)_{24}]^0$, and the HOMO of $[Pt_2Au_{36}(SH)_{24}]^0$ changes to an orbital corresponding to the HOMO−1 of $[Au_{38}(SH)_{24}]^0$, which results in a narrower HOMO-lowest unoccupied molecular orbital (LUMO) gap. This result suggests that $[PtAu_{37}(SH)_{24}]^0$ is more likely to give electrons to reactants and $[Pt_2Au_{36}(SH)_{24}]^0$ is less likely to give electrons to reactants compared with $[Au_{38}(SH)_{24}]^0$ in the reduction process. Evaluation of CRR activity with these NCs showed that $[PtAu_{37}(SCH_2Ph^tBu)_{24}]^0$ had the highest j_{CO} and FE_{CO} (80% at −0.6 V vs. RHE) (Fig. 26B).

In 2022, Zhu et al. synthesized $Ag_{4+x}Au_{40-x}$(C≡CPh(CH$_3$)$_2$)$_{28}$ (HC≡CPh(CH$_3$)$_2$ = 1-ethynyl-2,4-dimethylbenzene), and they investigated the effect of Ag doping in CRRs using Au_{44}(C≡CPh(CH$_3$)$_2$)$_{28}$, Au_{44}(d-MBT)$_{28}$, and $Ag_{4+x}Au_{40-x}$(C≡CPh

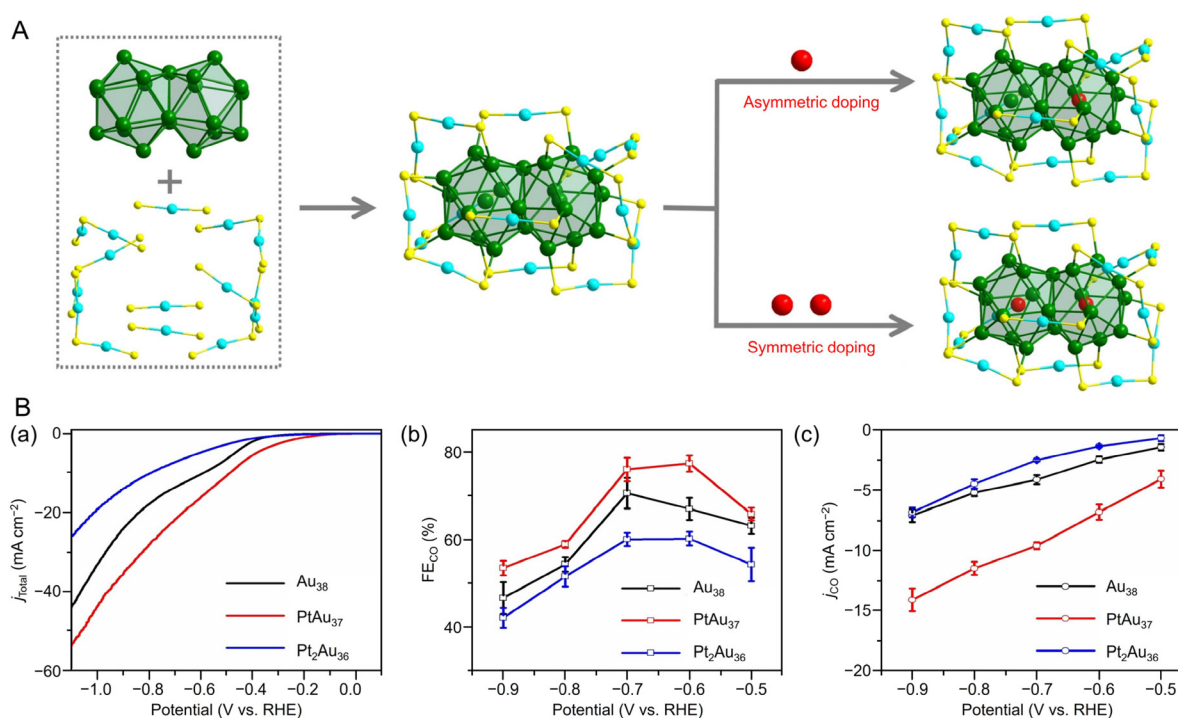**Fig. 26** (A) Structural anatomy of $[Au_{38}(SR)_{24}]^0$, asymmetrical $[Pt_1Au_{37}(SR)_{24}]^0$ and symmetrical $[Pt_2Au_{36}(SR)_{24}]^0$. Color labels: green/blue = Au, red = Pt, yellow = S. The C and H are omitted for clarify. (B) (a) LSV profiles of $[Au_{38}(SCH_2Ph^tBu)_{24}]^0$, $[PtAu_{37}(SCH_2Ph^tBu)_{24}]^0$ and $[Pt_2Au_{36}(SCH_2Ph^tBu)_{24}]^0$ catalysts in a 0.5 M KHCO$_3$ solution. (b) FE$_{CO}$ and (c) j_{CO} for $[Au_{38}(SCH_2Ph^tBu)_{24}]^0$, $[PtAu_{37}(SCH_2Ph^tBu)_{24}]^0$ and $[Pt_2Au_{36}(SCH_2Ph^tBu)_{24}]^0$ catalysts at different applied potentials. Error bars correspond to the deviations from several independent experiments. (A) and (B) are reproduced with permission from ref. 199. Copyright 2022 Wiley-VCH GmbH.

$(CH_3)_2)_{28}$.[310] When electrolytic reduction was performed in a 0.5 M KHCO$_3$ solution saturated with CO$_2$, the main products of the three NCs were CO and a small amount of H$_2$. In particular, $Ag_{4+x}Au_{40-x}(C\equiv CPh(CH_3)_2)_{28}$ exhibited the highest current density, and the FE$_{CO}$ reached approximately 98% (-0.5 V vs. RHE). They also measured electrochemical impedance and electrochemical surface area to determine the reason for the differences in their catalytic performance. It was suggested that Ag doping decreased the charge transfer resistance and increased the number of active sites, thereby enhancing CRR activity.

In 2022, Kim, Yoo, and Lee et al. used $[Au_{25}(PET)_{18}]^-$, $[Ag_{25}(SPhMe_2)_{18}]^-$, and bimetallic $[AuAg_{12}@Au_{12}(PET)_{18}]^-$ with a core–shell structure for CRR activity.[190] Comparing the CRR and HER activities of $[Au_{25}(PET)_{18}]^-$ and $[Ag_{25}(SPhMe_2)_{18}]^-$ activated by de-thiolation, the j_{CO} was found to be higher than j_{H_2} for both NCs. To investigate the origin of the CRR activity, DFT calculations were conducted (ligands were replaced with SCH$_3$ for simplicity). As a result, the partially de-thiolated sites, the bridging core metal, and the SR ligand in both NCs were determined to be the CRR active sites. The CRR limiting potential of $[Au_{25}(PET)_{18}]^-$ (0.14 V) is lower than that of $[Ag_{25}(SPhMe_2)_{18}]^-$ (0.24 V). The reason for the superior CRR activity of $[Au_{25}(PET)_{18}]^-$ might be that the stabilization of *COOH promoted more activation of CO$_2$. Therefore, they replaced the $Ag_{12}(SR)_{18}$ shell, the active site in $[Ag_{25}(SPhMe_2)_{18}]^-$, with the more active $Au_{12}(SR)_{18}$ shell to

improve the CRR activity. After optimizing the synthesis conditions, they obtained $[AuAg_{12}@Au_{12}(PET)_{18}]^-$ consisting of an AuAg$_{12}$ core and an Au$_{12}(PET)_{18}$ protective shell (Fig. 3C). Then, the CRR activity was evaluated using the alloy NCs activated by de-thiolation. The j_{CO} of $[AuAg_{12}@Au_{12}(PET)_{18}]^-$ was found to be similar to that of $[Au_{25}(PET)_{18}]^-$, and the FE$_{CO}$ was slightly lower than that of $[Au_{25}(PET)_{18}]^-$. Furthermore, the long-term stability of $[AuAg_{12}@Au_{12}(PET)_{18}]^-$ was confirmed using a zero-gap CO$_2$ electrolyzer. When galvanostatic electrolysis was performed at a current density of 200 mA cm^{-2}, the full cell potential of the electrolyzer maintained 2.13 ± 0.03 V and 57% FE$_{CO}$ for 24 h for $[AuAg_{12}@Au_{12}(PET)_{18}]^-$.

In 2022, Yang, Yang, and Wu et al. reported Au–Pd–Ag trimetallic alloy NCs. They showed the effect of Ag doping in CRRs using similar structures protected with TBBT (Fig. 5), namely $Au_4Pd_6(TBBT)_{12}$ and $Au_3AgPd_6(TBBT)_{12}$.[202] The LSV curves indicated that $Au_3AgPd_6(TBBT)_{12}$ exhibits a higher current density than $Au_4Pd_6(TBBT)_{12}$, suggesting that Ag doping enhances the catalytic CRR activity. The maximum FE$_{CO}$ of $Au_3AgPd_6(TBBT)_{12}$ was 94.1% (at -0.57 V vs. RHE), which was higher than that of $Au_4Pd_6(TBBT)_{12}$ (88.1% at -0.67 V vs. RHE). Furthermore, $Au_3AgPd_6(TBBT)_{12}$ showed high long-term stability, and no decrease in current density or selectivity was observed after 65 h of electrolysis (-0.57 V vs. RHE). They used DFT calculations to investigate the effect of Ag doping on the reaction mechanism. Notably, the increase in the free

energy of CO desorption was smaller for $Au_3AgPd_6(SCH_3)_{11}$ than for $Au_4Pd_6(SCH_3)_{11}$, which suggests that Ag doping into $Au_4Pd_6(SCH_3)_{11}$ weakens the binding energy of *CO on the active site and promotes CO desorption, thereby improving the reduction to CO. This may be attributed to the electronic effects caused by the substitution of Ag atoms. From the XPS spectra, the binding energies of Au 4f and Pd 3d of $Au_3AgPd_6(TBBT)_{12}$ were significantly higher than those of $Au_4Pd_6(TBBT)_{12}$, which explained why the *CO adsorption on the active site of $Au_3AgPd_6(SCH_3)_{11}$ was weaker. Furthermore, this electronic effect might suppress the competitive HER. Therefore, $Au_3AgPd_6(SCH_3)_{11}$ showed high selectivity as an electrocatalyst for the reduction of CO_2 to CO owing to the more difficult desorption of H*. These results demonstrated that Ag doping can affect the electronic structure of NCs and enhance CRR activity.

In 2020, Kauffman, Mpourmpakis, and Jin *et al.* evaluated the electrocatalytic activity of CRRs using $[Au_{24}Pd(PET)_{18}]^0$ and $[Au_{25}(PET)_{18}]^0$ (Fig. 27A).[311] $[Au_{25}(PET)_{18}]^0$ showed an FE_{CO} of ~100% below −0.9 V *vs.* RHE. However, at more negative potentials, the FE_{CO} began to decrease (approximately 60% at −1.2 V *vs.* RHE; Fig. 27A). In contrast, $[Au_{24}Pd(PET)_{18}]^0$ maintained ~100% FE_{CO} over a much wider potential range and showed almost complete HER suppression up to −1.2 V *vs.* RHE. The j_{CO} and mass activity of CO showed that $[Au_{24}Pd(PET)_{18}]^0$ was more active than $[Au_{25}(PET)_{18}]^0$ at all potentials. The mass activity of $[Au_{24}Pd(PET)_{18}]^0$ (~1770 mA mg^{-1}) was approximately twice as high as $[Au_{25}(PET)_{18}]^0$ (~980 mA mg^{-1}) at −1.2 V *vs.* RHE. Considering that only one Au atom is replaced by a Pd atom, the above results indicate that the doping effect of different elements plays an important role in CO production. No change in absorption spectrum was observed in $[Au_{24}Pd(PET)_{18}]^0$, even after 6 h of electrolysis at −0.8 V *vs.* RHE, demonstrating its stability. From the DFT calculations, the thermodynamic limiting potentials (U_L) in CRRs and HERs for $[Au_{24}Pd(SCH_3)_{18}]^0$ and $[Au_{25}(SCH_3)_{18}]^0$ were calculated (Fig. 27B). Fully ligand-protected NCs were electrochemically inactive and had relatively large U_L (CRR) values. However, the NCs were activated when some Au and S atom sites were exposed, such that the Au_{13} core can act as an electron reservoir. From the calculated ΔU_L, $Au_{24}PdS(SCH_3)_{17}$ with the active site at the S atom was predicted to show the most selective activity for the CRR.

From these reports, it became clear that (1) Ag, Cd, and Pd doping to Au NCs tends to improve CRR activity and selectivity, and (2) Pt doping may improve HER selectivity. Such a doping effect is considered to depend also on the geometric/electronic structure of the Au NCs.

3.3.5 Other effects of gold nanoclusters. Other studies on electrochemical CRRs using Au NCs are summarized in Table 5. Flake *et al.* evaluated CRR activity by changing the binder used in electrode fabrication from non-sulfonate-containing poly(vinylidene fluoride) (PVDF) to sulfonate-containing Nafion using $[Au_{25}(PET)_{18}]^−$.[312] The onset potential for CO_2 reduction to CO was shifted ~170 mV toward the anode side when Nafion was used compared with that when PVDF was
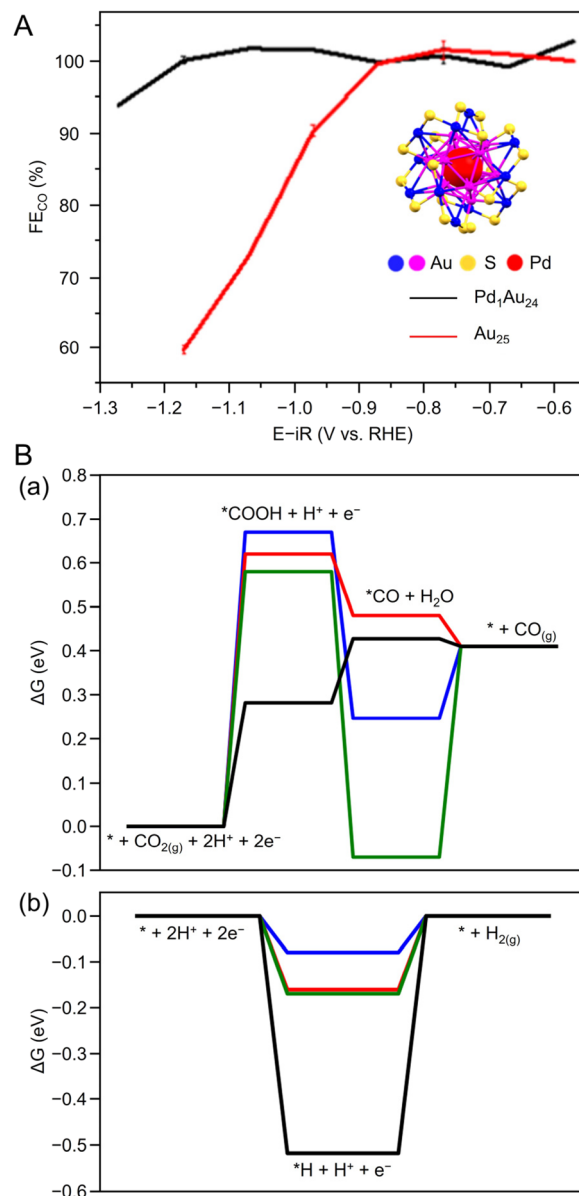

Fig. 27 (A) Electrocatalytic CO_2 reduction performance (FE_{CO}) of $[Au_{25}(PET)_{18}]^0$ and $[Au_{24}Pd(PET)_{18}]^0$; inset: atom packing structures of $[Au_{24}Pd(PET)_{18}]^0$ (−R groups omitted for clarity). (B) Free-energy diagrams for electrochemical (a) CRR and (b) HER at $U = 0$ V *vs.* RHE of $[Au_{24}Pd(SCH_3)_{18}]^0$ and $[Au_{25}(SCH_3)_{18}]^0$. Panels (A) and (B) are reproduced with permission from ref. 311. Copyright 2020 American Chemical Society.

used. Thus, the environment surrounding $Au_n(SR)_m$ plays an important role in CRR activity. Lee and Oh *et al.* reported on a practical photoelectrochemical cell using GDE-based electrodes for flow electrolysis, which was expected to achieve high current densities by removing the mass diffusion limit of gaseous CO_2 in water.[313] They constructed a combined system using a NiFe reverse opal anode for the OER catalyst, an Au_{25}-loaded GDE cathode for the CRR catalyst, and 3 M potassium hydroxide (KOH) as an electrolyte in combination with $Ga_{0.5}In_{0.5}P/GaAs$ tandem solar cells. Solar-to-CO (STC) conver-

sion efficiencies of 18.0% were achieved over 12 h under CO_2 gas flow (concentration: 100%), and STC efficiencies of 15.9% were achieved using typical CO_2 concentrations (10% of CO_2) in the flue gas. The STC efficiency was greatly improved considering that previous reports using solar-powered Au_{25} cluster-based CO_2 reactors had STC efficiencies of less than 1%.[293]

3.4 Electrocatalytic CO_2 reduction reactions using silver nanoclusters

Among the precious metals, Ag is relatively inexpensive and abundant. Furthermore, it has attracted attention in CRRs because of its high selectivity for CO formation.[202,314] The reported cases of Ag-based NCs used in CRRs are summarized in Table 6.

In 2021, Tang, Jin, and Tang et al. evaluated CRR activity using $[Ag_{15}(C\equiv C^tBu)_{12}]^+$ as an electrocatalyst.[258] Fig. 28A shows the ESI-MS spectrum and geometric structure of $[Ag_{15}(C\equiv C^tBu)_{12}]^+$, which comprises a bcc structure with a metal core configuration of $Ag@Ag_8@Ag_6$. $[Ag_{15}(C\equiv C^tBu)_{12}]^+$

was first mixed with the conductive support, CB, in a 2 : 1 ratio before the CRR evaluation. As shown in Fig. 28B(a), the main product of CRRs was CO in the applied voltage range from −0.5 to −1.1 V vs. RHE. FE_{CO} remained above 90% over the potential range of −0.6 to −0.9 V vs. RHE and reached approximately 95% at −0.6 V vs. RHE. The partial current densities of CO and H_2 increased with overvoltage, and the maximum TOF value was 6.37 s^{-1} at −1.1 V vs. RHE. Furthermore, constant potential measurements showed that the current density of the $[Ag_{15}(C\equiv C^tBu)_{12}]^+$ catalyst decreased only slightly after 10 h of continuous operation at −0.75 V vs. RHE, indicating high long-term stability (Fig. 28Bb). Next, to elucidate the electrocatalytic mechanism, the optimal catalytic site on $[Ag_{15}(C\equiv CCH_3)_{12}]^+$ was determined by DFT calculations, and the selectivities of the reduction products were compared. As a result, the formation of *COOH was the rate-limiting step in $[Ag_{15}(C\equiv CCH_3)_{12}]^+$, and the formation of H_2 was energetically favorable (Fig. 28Ca). However, with one ligand removed ($[Ag_{15}(C\equiv CCH_3)_{11}]^+$), the appearance of an Ag active site is

---

Table 6 Representative references on CRR activity using Ag NCs (section 3.4)

Nanocluster/nanoparticle	Electrolytes	Electrolyzer	Main product	Selectivity (@V vs. RHE)	Current density (mA cm^{-2}@V vs. RHE)	Stability (@V vs. RHE)	Ref.
$[Ag_{15}(C\equiv C^tBu)_{12}]^+$	0.5 M $KHCO_3$ aq.	H-cell	CO	~95%@−0.6	13.0@−0.9	10 h@−0.75	258[b]
$Ag_{32}(C\equiv CPh(CF_3)_2)_{24}$	0.5 M $NaHCO_3$ aq.	H-cell	CO	96.44%@−0.8	9.05@−1.0	15 h	260[c]
$[Ag_{32}(DPPE)_5(SC_6H_4CF_3)_{24}]^{2-}$				56.67%@−1.0	N/A	15 h	
$(Mo_6O_{22})@H_3Ag_{49}(MO_3)_9(MoO_4)$– $(TC4A)_6(^iPrS)_{18}(CH_3CN)_2(H_2O)$	0.5 M $KHCO_3$ aq.	H-cell	H_2	~54%@−0.8	N/A	5 h@−0.8	266[d]
			CO	44.75%@−0.8	4@−0.8		
$[Au_7Ag_8(C\equiv C^tBu)_{12}]^+$	1.0 M KOH aq.	Flow cell	CO	~90%@−0.19	~160@−0.19	10 h @−0.49	245[c]
			HCOOH	0%@−1.19	0@−0.19		
$[Ag_9Cu_6(C\equiv C^tBu)_{12}]^+$			CO	~25%@−1.19	~30@−0.19	10 h @−1.19	
			HCOOH	~47%@−1.19	~50@−0.19		
$[Au_2Ag_8Cu_5(C\equiv C^tBu)_{12}]^+$			CO	~25%@−1.19	~30@−0.19	10 h @−0.99	
			HCOOH	~20%@−1.19	~25@−0.19		
$[Ag_{15}Cu_6(C\equiv CPh(CF_3)_2)_{18}(DPPE)_2]^-$	0.1 M $KHCO_3$ aq.	H-cell MEA-cell	CO	91.3%@−0.81	−60@−3.25[a]	145 h@−3.25[a]	263[e]
$[Ag_9Cu_6(C\equiv C^tBu)_{12}]^+$				48.5%@−0.89	N/A	N/A	
$[AuAg_{26}(S-Adm)_{18}S]^-$	EMIM-BF_4/H_2O (v/v = 7 : 1) + 0.5 M H_2SO_4	H-cell	CO	98.4%@−0.97	8@−0.97	11 h @−0.97	255[c]
$[Ag_{25}(SPhMe_2)_{18}]^-$				~60%@−0.97	3@−0.97	N/A	
$Au_{21}(S-Adm)_{16}$				~5.0% @−0.97	1@−0.97	N/A	
$Ag_{40.63}Cu_{9.37}(SC_7H_7O)_{32}$	2 M KOH aq.	Flow cell	C_1 product	~58%@−0.57	~3.0@−0.57	N/A	254[f]
			C_2 product	29.5%@−0.57	−2.24@−0.57		
$Ag_{36.14}Cu_{13.86}(SC_7H_7O)_{32}$			C_1 product	~40%@−0.57	~2.1@−0.57	14 h@−0.57	
			C_2 product	47.5%@−0.57	−3.04@−0.57		
~5 nm Ag NP			N/A	N/A	N/A	N/A	
$Au_{24}Ag_{20}(C\equiv C^tBu)_{24}Cl_2$	0.5 M $KHCO_3$ aq.	H-cell	CO	~90%@−0.5	25@−0.8	N/A	315[g]
$Au_{24}Ag_{20}(C\equiv CPhC)_{24}Cl_2$				~90%@−0.5	17.5@−0.8	N/A	
$[Au_{43}Ag_{38}(C\equiv C^tBu)_{36}Cl_{12}]^+$				~80%@−0.5	7.5@−0.8	N/A	
$[Au_{43}Ag_{38}(C\equiv CPhC)_{36}Cl_9]^+$				~70%@−0.5	5@−0.8	N/A	
$[Au_8Ag_{55}(DPPP)_4(SC_6H_{11})_{34}]^{2+}$	0.5 M $KHCO_3$ aq.	H-cell	CO	~67%@−0.8	~14@−0.8	9 h@−0.8	316[h]
			H_2	~25%@−0.8	N/A		
$[Au_8Ag_{57}(DPPP)_4(SC_6H_{11})_{32}Cl_2]^+$			CO	~62%@−0.8	~8@−0.8	N/A	
			H_2	~25%@−0.8	N/A		
$[Au_{12}Ag_{60}(DPPP)_6(SC_6H_{11})_{31}Br_9]^{2+}$			CO	~46%@−0.8	~5@−0.8	N/A	
			H_2	~45%@−0.8	N/A		

^{i}Pr = isopropyl, EMIM-BF_4 = 1-ethyl-3-methylimidazolium tetrafluoroborate, S-Adm = 1-adamantanethiolate, $SPhMe_2$ = 2,4-dimethylbenzenethiolate, DPPE = 1,2-bis(diphenylphosphino)ethane, TC4A = thiacalix[4]arene, DPPP = 1,3-bis(diphenylphosphino)propane, MEA = membrane electrode assembly. [a] vs. MEA-cell potential. [b] Vulcan XC-72R. [c] Multi-walled carbon nanotube. [d] Acetylene black. [e] Ketjen black (EC-600JD). [f] Hydrophobic carbon paper. [g] Carbon paper (Toray TGP-H-090). [h] Carbon paper.
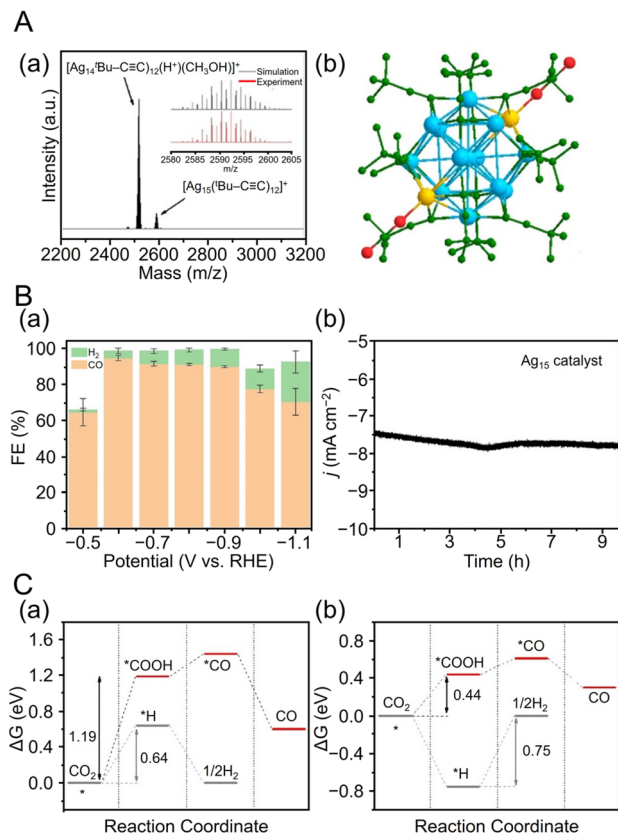
Fig. 28 (A) (a) the ESI-MS spectra and (b) the overall structure of $[Ag_{15}(C\equiv C^tBu)_{12}]^+$. (B) (a) Faradaic efficiency at various applied potentials over $[Ag_{15}(C\equiv C^tBu)_{12}]^+$ in aqueous solution of 0.5 M KHCO$_3$. (b) Stability of $[Ag_{15}(C\equiv C^tBu)_{12}]^+$ for CO$_2$ reduction at -0.75 V vs. RHE. (C) Comparison of ΔG of electroreduction of CO$_2$ to CO vs. HER on (a) $[Ag_{15}(C\equiv CCH_3)_{12}]^+$, (b) $[Ag_{15}(C\equiv CCH_3)_{11}]^+$. (A)–(C) are reproduced with permission from ref. 258. Copyright 2021 Wiley-VCH GmbH.

favorable for the formation of *COOH and significantly lowers the energy barrier for the formation of *COOH and promotes CRR activity (Fig. 28Cb).

3.4.1 Structure effects in silver nanoclusters. In 2022, Pei and Zhu et al. evaluated CRR activity using monomeric compounds, such as $Au_{24}Ag_{20}(C\equiv C^tBu)_{24}Cl_2$ ($Au_{24}Ag_{20}$-1) and $Au_{24}Ag_{20}(C\equiv CPhC)_{24}Cl_2$ ($Au_{24}Ag_{20}$-2; HC$\equiv$CPhC = 2-methylphenylacetylene), and two dimeric compounds, such as $Au_{43}Ag_{38}(C\equiv C^tBu)_{36}Cl_{12}$ ($Au_{43}Ag_{38}$-1) and $Au_{43}Ag_{38}(C\equiv CPhC)_{36}Cl_9$ ($Au_{43}Ag_{38}$-2).[315] The monomer NCs ($Au_{24}Ag_{20}$-1 and 2) have a similar core structure containing icosahedral Ag$_{12}$ surrounded by Ag$_{20}$. These two $Au_{24}Ag_{20}$ monomers self-assemble in different growth modes to form two different dimers: $Au_{43}Ag_{38}$-1 and $Au_{43}Ag_{38}$-2. The catalytic ability of these monomers and dimers for CRRs was examined, with the $Au_{24}Ag_{20}$ monomer exhibiting higher j_{CO} and FE$_{CO}$ than the $Au_{43}Ag_{38}$ dimer. Among all four species, $Au_{24}Ag_{20}$-1 showed the highest CRR activity, and $Au_{43}Ag_{38}$-2 showed the lowest CRR activity. Electrochemical impedance measurements suggest that the $Au_{24}Ag_{20}$ monomer has faster charge transfer than the $Au_{43}Ag_{38}$ dimer. Structural effects have also been investigated

using metal NCs with different chemical compositions. Although $[Au_8Ag_{55}(DPPP)_4(SC_6H_{11})_{34}](BPh_4)_2$, $[Au_8Ag_{57}(DPPP)_4$ $(SC_6H_{11})_{32}Cl_2]Cl$, $[Au_{12}Ag_{60}(DPPP)_6(SC_6H_{11})_{31}Br_9]Br_2$ are similar in size and structure, their different assembly structures lead to significantly different CRR catalytic performances. Among the three NCs, $[Au_8Ag_{55}(DPPP)_4(SC_6H_{11})_{34}]$ were found to have strong CO$_2$ adsorption capacity and exhibit the best CRR performance due to charge segregation placing Ag atoms on the outer side of Au$_8$.[316]

3.4.2 Ligand effects in silver nanoclusters. C$\equiv$CR ligands have been used by Wang et al. for the semihydrogenation of alkyne[317] and by Tsukuda et al. for the HER[318] to enhance the activity of these reactions, and similar enhancements have also been expected for CRRs. In 2022, Tang, Wang, and Tang et al. compared the effect of ligands in CRRs using $Ag_{32}(C\equiv CPh$ $(CF_3)_2)_{24}$ and $[Ag_{32}(DPPE)_5(SC_6H_4CF_3)_{24}]^{2-}$.[260] In this case, $Ag_{32}(C\equiv CPh(CF_3)_2)_{24}$ is composed of an Ag$_{17}$ kernel. $[Ag_{32}(DPPE)_5(SC_6H_4CF_3)_{24}]^{2-}$ also has an Ag$_{17}$ kernel, although the overall geometric structure and the number of ligands are different. When catalysts were prepared by mixing both NCs with CNTs in the ratio of 2 : 1, respectively, and evaluated for CRR activity, CO and H$_2$ were the main products. The FE$_{CO}$ was 96.44% at -0.8 V vs. RHE for $Ag_{32}(C\equiv CPh(CF_3)_2)_{24}$, but it was only 56.67% at -1.0 V vs. RHE for $[Ag_{32}(DPPE)_5(SC_6H_4CF_3)_{24}]^{2-}$ (Fig. 29A(a and b)). Furthermore, as shown in Fig. 29A(c and d), the overall CO and H$_2$ partial current densities in both NCs showed gradually increasing trends when the potential was more negative. DFT calculations were performed to clarify how the CRR activity was affected by different ligands (C$\equiv$CCH$_3$, P$_2$C$_2$H$_6$, and SCH$_3$ were used as ligands to simplify the calculations). As a result, $Ag_{32}(C\equiv CCH_3)_{24}$ and $[Ag_{32}(P_2C_2H_6)_5(SCH_3)_{24}]^{2-}$ have large free energy barriers (1.28 and 1.23 eV, respectively), but when one C$\equiv$CCH$_3$ or SCH$_3$ is removed, the thermodynamic barrier to *COOH formation is decreased (0.40 and 0.50 eV, respectively) and CRR activity is enhanced (Fig. 29B and C). $Ag_{32}(C\equiv CCH_3)_{23}$ also has a higher thermodynamic barrier to H* for H$_2$ formation than $[Ag_{32}(P_2C_2H_6)_5(SCH_3)_{23}]^{2-}$. This HER suppression suggests that $Ag_{32}(C\equiv CPh(CF_3)_2)_{24}$ has a high selectivity for CO$_2$ to CO.

In 2023, Liu et al. synthesized a polymolybdate-templated Ag NC, $[(Mo_6O_{22})@H_3Ag_{49}(MO_3)_9(MoO_4)-(TC4A)_6(^iPrS)_{18}(CH_3CN)_2$ $(H_2O)]$ (Ag$_{49}$Mo$_{16}$ NC), by a solvothermal method and evaluated its CRR activity.[266] As a result, the polymolybdate-templated Ag$_{49}$Mo$_{16}$ NC exhibited higher TOF values and j_{CO} than $(NH_4)_6Mo_7O_{24}$, indicating that the Ag site is the active center of the CRR. The highest FE$_{CO}$ was 44.75% at -0.8 V vs. RHE.

3.4.3 Doping effects in silver nanoclusters. Ag-based alloy NCs have also been used in electrochemical CRRs. In 2021, Liu and Huang et al. used $[Ag_{25}(SPhMe_2)_{18}]^-$, $Au_{21}(S-Adm)_{16}$, and $[AuAg_{26}(S-Adm)_{18}S]^-$ as electrocatalysts to evaluate CRR activity.[255] $[AuAg_{26}(S-Adm)_{18}S]^-$ is composed of an AuAg$_{12}$ icosahedral kernel and an Ag$_{14}$(SR)$_{18}$S shell, where the four triangular facets of the icosahedral kernel are exposed without protection by SR. Electrochemical measurements in an ionic liquid (1-ethyl-3-methylimidazolium tetrafluoroborate/H$_2$O, v/v

= 7 : 1) containing water saturated with CO_2 showed that the main CO_2 reduction products were CO and H_2. Particularly, $[AuAg_{26}(S\text{-}Adm)_{18}S]^-$ showed the highest CO selectivity in the potential range from −0.82 to −1.12 V vs. RHE. The maximum FE_{CO} of $[AuAg_{26}(S\text{-}Adm)_{18}S]^-$ at −0.97 V vs. RHE was 98.4%, approximately 1.8 and 24 times higher than that of $[Ag_{25}(SPhMe_2)_{18}]^-$ and $Au_{21}(S\text{-}Adm)_{16}$, respectively. The electrochemical stability of $[AuAg_{26}(S\text{-}Adm)_{18}S]^-$ was evaluated by chronopotentiometry at −0.97 V vs. RHE, which showed the highest CO selectivity, and the current density remained high with almost no decrease after 11 h of operation. In addition, they investigated the mechanism of catalytic selectivity by performing DFT calculations using SCH_3 as a ligand. The *COOH

formation energy barrier of $[AuAg_{26}(SCH_3)_{18}S]^-$ (1.06 eV) was lower than that of $[Ag_{25}(SCH_3)_{18}]^-$ (1.26 eV), $Au_{21}(SCH_3)_{16}$ (1.83 eV), and $[Ag_{27}(SCH_3)_{18}S]^-$ (1.11 eV). This suggested that Au doping of Ag NCs and the exposed core structure of $[AuAg_{26}(S\text{-}Adm)_{18}S]^-$ promoted CRR activity.

In 2023, Bootharaju, Tang, Hwang, and Hyeon et al. evaluated CRR activity using $[Ag_{15}Cu_6(C\equiv CPh(CF_3)_2)_{18}(DPPE)_2]^-$ as an electrocatalyst.[263] $Ag_{15}Cu_6$ has a bcc-based structure with a core of $Ag@Ag_8@Ag_2Cu_4$, as shown in Fig. 13C. For comparison, $[Ag_9Cu_6(C\equiv C^tBu)_{12}]^+$ (Ag_9Cu_6) and $Ag_{15}Cu_6$, which also have bcc structures and are similarly protected by $C\equiv CR$, were loaded on Ketjen black ($Ag_{15}Cu_6/C$ and Ag_9Cu_6/C, respectively) and evaluated for CRR catalytic activity. As a result, $Ag_{15}Cu_6/C$ showed high FE_{CO} (>85%) in the potential range of −0.72 to −0.87 V vs. RHE, with the highest FE_{CO} of 91.3% at −0.81 V vs. RHE. In contrast, Ag_9Cu_6/C showed the highest FE_{CO} of 48.5% at −0.89 V vs. RHE. Moreover, a membrane electrode assembly (MEA) cell was used to evaluate CRR activity. FE_{CO} remained at
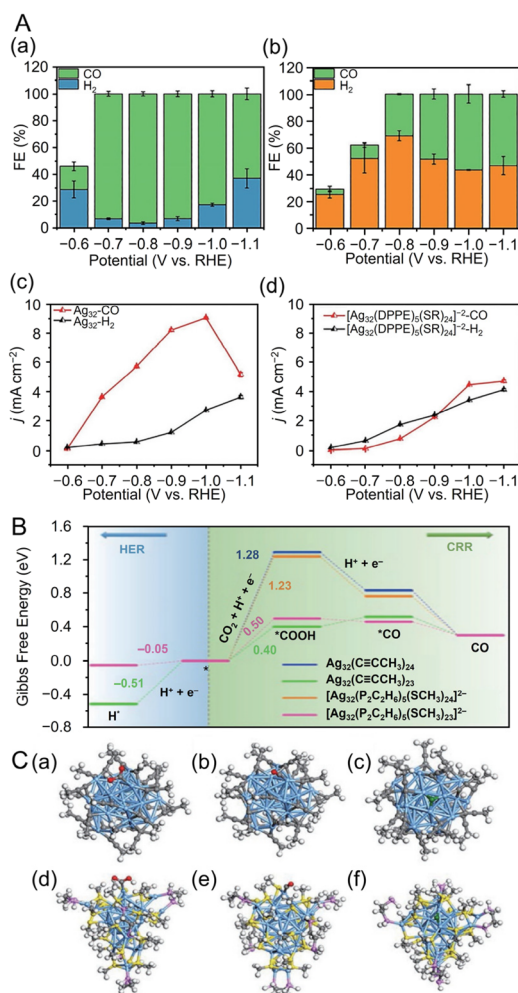

Fig. 29 (A) Faradaic efficiency of CO and H_2 for (a) $Ag_{32}(C\equiv CPh(CF_3)_2)_{24}$ and (b) $[Ag_{32}(DPPE)_5(SC_6H_4CF_3)_{24}]^{2-}$ at different applied voltages. Partial current densities of CO and H_2 for (c) $Ag_{32}(C\equiv CPh(CF_3)_2)_{24}$ and (d) $[Ag_{32}(DPPE)_5(SC_6H_4CF_3)_{24}]^{2-}$ at different applied voltages (electrolyte: 0.5 M $NaHCO_3$ aq.). (B) Change of reaction free energy (ΔG) at each fundamental step of CRR and HER for two NCs and stripping of one intact ligand. (C) Adsorption structure of COOH*, CO*, and H* intermediates on (a–c) $[Ag_{32}(C\equiv CCH_3)_{23}]^+$ and (d–f) $[Ag_{32}(P_2C_2H_6)_5(SCH_3)_{23}]^-$. Colour code: Ag, blue; C, gray; O, red; S, yellow; P, pin; H*, green and other H, white. (A)–(C) are reproduced with permission from ref. 260. Copyright 2022 Springer Nature.
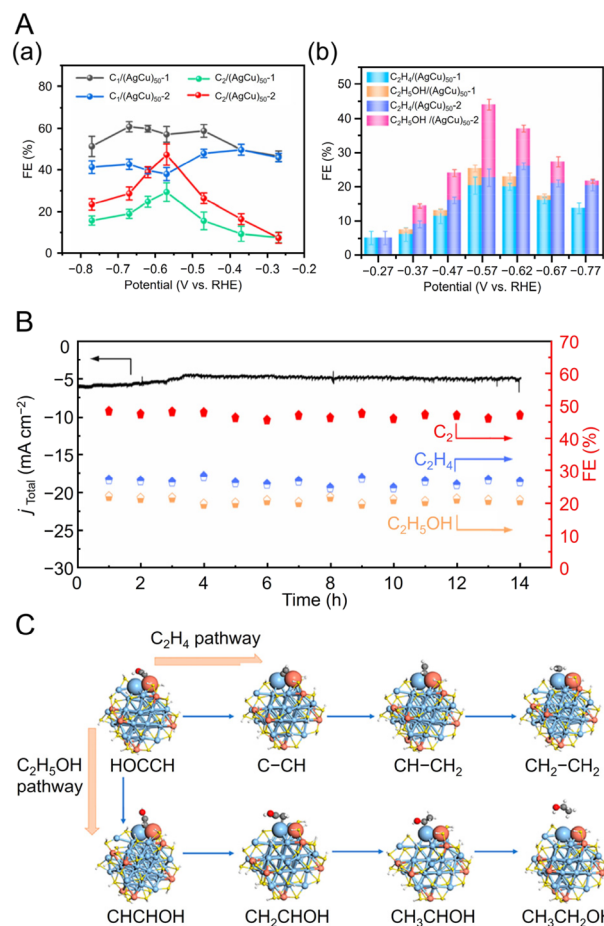

Fig. 30 (A) CRR performance in a flow cell reactor. (a) C_1 and C_2 products FE on $(AgCu)_{50}$-1 and $(AgCu)_{50}$-2 at different potentials. (b) C_2H_4 and C_2H_5OH FE on $(AgCu)_{50}$-1 or $(AgCu)_{50}$-2 at different potentials. (B) Stability test of $(AgCu)_{50}$-2 over 14 h of CO_2 electrolysis in 2 M KOH at −0.57 V vs. RHE (the arrows indicate the corresponding axes). (C) Reaction pathway diagrams of $Ag_{42}Cu_8$ for the production of ethylene and ethanol at site 2 for DFT calculations. (A)–(C) are reproduced with permission from ref. 254. Copyright 2023 American Chemical Society.

~90% and j_{CO} was −60 mA cm^{-2} during the 145 h electrolytic reaction, indicating that Ag$_9$Cu$_6$/C has high stability. From DFT calculations, it was revealed that the removal of one C≡CCH$_3$ exposes the ligand-deficient AgCu dual site and the thermodynamic barrier to *COOH formation was reduced. As a result, Ag$_{15}$Cu$_6$ with one desorbed C≡CCH$_3$ can proceed with a low energy barrier of 0.34 eV, associated with the desorption of *CO to CO. For the competing HER, the higher energy barrier of the H* desorption step (0.61 eV) to H$_2$ evolution activity was also considered to enhance CO activity and selectivity.

In 2023, Wang, Yan, and Wu et al. evaluated CRR activity using Ag$_{40.63}$Cu$_{9.37}$(SC$_7$H$_7$O)$_{32}$ [(AgCu)$_{50}$-1] and Ag$_{36.14}$Cu$_{13.86}$(SC$_7$H$_7$O)$_{32}$ [(AgCu)$_{50}$-2].[254] This is the first report of C$_2$ production from CO$_2$ reduction in the application of metal NCs as CRR catalysts. Both (AgCu)$_{50}$ NCs also have a bimetallic M$_{50}$ (M = Ag/Cu) core with fcc topology protected by 32 ligands of 3-methoxythiophenol. The catalytic CRR activity of (AgCu)$_{50}$, as

well as Ag NPs of ~5 nm for comparison, was measured by flow cell in 2 M KOH electrolyte saturated with Ar and CO$_2$. In the same potential range, the maximum FE$_{C_2}$ for (AgCu)$_{50}$-1 and (AgCu)$_{50}$-2 reached 29.5% and 47.5%, respectively, indicating a conversion in catalytic selectivity due to Cu substitution (Fig. 30Aa). Comparing the C$_2$ and C$_1$ partial current densities of both NCs, (AgCu)$_{50}$-2 showed higher values (Fig. 30Aa). This improvement in FE was mainly due to ethanol production, with FE$_{CO}$ in (AgCu)$_{50}$-2 being 19% lower than that in (AgCu)$_{50}$-1, and more C$_2$ than CO was produced in (AgCu)$_{50}$-2 (Fig. 30Ab). Comparing the FE ratios of C$_2$/C$_1$ for both NCs, (AgCu)$_{50}$-2 reached a C$_2$/C$_1$ ratio of 1.2 at −0.57 V vs. RHE, indicating higher selectivity for the C$_2$ compound. Furthermore, (AgCu)$_{50}$-2 exhibited high stability, with FE remaining almost the same after long-term CRR activity at −0.57 V vs. RHE (Fig. 30B). DFT calculations showed that the Cu–Cu sites are thermodynamically more favorable than the Ag–Cu sites, such

Table 7 Representative references on CRR activity using Cu NCs (section 3.5)

Nanocluster/nanoparticle	Electrolytes	Electrolyzer	Main product	Selectivity (@V vs. RHE)	Current density (mA cm^{-2}@V vs. RHE)	Stability (@V vs. RHE)	Ref.
Cu$_4$Ti$_9$O$_9$(BC)$_{18}$(O^{i}Pr)$_3$(^{t}BuC≡C)(CH$_3$CN)	1.0 M KOH aq.	Flow cell	C$_2$H$_4$	~50%@−1.0	~200@−1.0	8 h@~−1.0	330
			H$_2$	~30%@−1.0	~120@−1.0		
			CO	~10%@−1.0	~40@−1.0		
			CH$_4$	~7%@−1.0	~28@−1.0		
			CH$_3$CH$_2$OH	~2%@−1.0	~8@−1.0		
			CH$_3$COO$^-$	~0.5%@−1.0	~2@−1.0		
			HCOO$^-$	~0.5%@−1.0	~2@−1.0		
[Cu$_8$(H)(L1)$_6$PF$_6$]$^+$	0.5 M KHCO$_3$ aq.	H-cell	HCOOH	50%@−1.0	7.5@−1.0	8 h@−0.9	273 [a]
[Cu$_8$(S^{t}Bu)$_4$(L1)$_4$]$^+$				92%@−1.0	15@−1.0	8 h@−0.9	
[Cu$_8$(S^{t}Bu)$_4$(L2)$_4$]$^+$				~80%@−1.0	21@−1.0	8 h@−1.0	
Cu$_{13}$(MBO)$_{12}$	0.1 M KOH aq.	N/A	H$_2$	72.6%@−1.05	N/A	N/A	326
			CO	13.2%@−1.05			
			CH$_4$	0.25%@−1.05			
Cu$_{25}$H$_{22}$((p-FPh)$_3$P)$_{12}$	0.1 M KHCO$_3$ aq.	H-cell	CO	N/A	N/A	N/A	329 [a]
			H$_2$	~47%@−0.8	N/A		
[Cu$_{26}$(CF$_3$CO$_2$)$_8$(CH$_3$O)$_2$(C≡C^{t}Bu)$_4$(DPPE)$_3$H$_{11}$]$^+$			CO	81%@−0.8	N/A	50 h@−0.8	
			H$_2$	~19%@−0.8	N/A		
[Cu$_{53}$(CF$_3$COO)$_{10}$(C≡C^{t}Bu)$_{20}$Cl$_2$H$_{18}$]$^+$			CO	~8%@−0.8	N/A	N/A	
			H$_2$	~92%@−0.8	N/A		
[Cu$_{61}$(S^{t}Bu)$_{26}$S$_6$Cl$_6$H$_{14}$]$^+$			CO	N/A	N/A	N/A	
			H$_2$	~98%@−0.8	N/A		
Cu$_{32}$H$_{20}$(S$_2$P(O^{i}Pr)$_2$)$_{12}$	0.1 M KHCO$_3$ and 0.4 M KCl aq.	H-cell	HCOOH	~90%@−0.55	~25@−0.55	N/A	325 [a]
[Cu$_{25}$H$_{22}$(PPh$_3$)$_{12}$]$^+$	0.5 M KHCO$_3$ aq.	H-cell	H$_2$	~90%@−0.8	~27@−1.2	12 h@−0.8	327 [b]
			CO	~1%@−0.8	~1@−1.2		
			HCOOH	~8.5%@−0.8	~1@−1.2		
[AuCu$_{24}$H$_{22}$(PPh$_3$)$_{12}$]$^+$			H$_2$	~48%@−0.8	~22@−1.2	12 h@−0.8	
			CO	~40%@−0.8	~8@−1.2		
			HCOOH	~12%@−0.8	~2@−1.2		
[Cu$_{25}$H$_{22}$(p-FPPh$_3$)$_{12}$]$^+$			H$_2$	~80%@−0.8	~45@−1.2	12 h@−0.8	
			CO	~18%@−0.8	~2@−1.2		
			HCOOH	~2%@−0.8	~2@−1.2		
[AuCu$_{24}$H$_{22}$(p-FPPh$_3$)$_{12}$]$^+$			H$_2$	~60%@−0.8	~25@−1.2	12 h@−0.8	
			CO	~12%@−0.8	~7@−1.2		
			HCOOH	~28%@−0.8	~2@−1.2		

BC = benzoic acid, ^{i}Pr = isopropyl, PPh$_3$ = triphenylphosphine, S^{t}Bu = tert-butylthiolate, L1 = 9H-carbazole-9-carbodithioate, L2 = O-ethyl carbonodithiolate, MBO = 2-mercaptobenzoxazole, DPPE = 1,2-bis(diphenylphosphino)ethane, p-FPPh$_3$ = tris(4-fluorophenyl)phosphine. [a] Vulcan XC-72. [b] Multi-walled carbon nanotube.

that $(AgCu)_{50}$-2 with more Cu–Cu sites has relatively high selectivity for C_2 products (Fig. 30C).

In 2022, Tang *et al.* investigated the effect of metal core alloying on CRR selectivity using C≡CR-protected bimetallic $[Au_7Ag_8(C≡C^tBu)_{12}]^+$ (Au_7Ag_8),[244] $[Au_9Ag_6(C≡C^tBu)_{12}]^+$ (Au_9Ag_6),[244] and trimetallic $[Au_2Ag_8Cu_5(C≡C^tBu)_{12}]^+$ $(Au_2Ag_8Cu_5)$.[245] Au_7Ag_8, Ag_9Cu_6, and $Au_2Ag_8Cu_5$ have a core–shell–shell structures ($M_{core}@M_{cube}@M_{octahedron}$), with core structures of $Au_1@Ag_8@Au_6$, $Ag_1@Ag_8@Cu_6$, and $Au_1@Au_1Ag_4Cu_3@Ag_4Cu_2$, respectively. Au_7Ag_8 only converted CO_2 to CO, but Ag_9Cu_6 and $Au_2Ag_8Cu_5$ converted CO and HCOOH, with maximum FE_{HCOOH} values of 47.0% and 28.3%, respectively. From DFT calculations, the desorption of surface ligands exposed active metal sites, improving the selectivity and activity of the CRRs. Furthermore, the formation of surface hydrides played an important role in the formation and stabilization of HCOO* at the Au–Cu active center. Thus, the inclusion of Cu in the core structure led to a high selectivity of HCOOH. This report indicated that the selectivity of CRR products can be adjusted by controlling the metal core of C≡CR-protected metal NCs at the atomic level.

As mentioned above, it was clarified that Au or Cu doping to Ag NCs can greatly change the activity and selectivity of CRR.

3.5 Electrocatalytic CO_2 reduction reactions using copper nanoclusters

Cu is attracting attention in electrocatalytic CRRs as a unique metal catalyst that can yield a variety of products by multi-electron reduction.[319,320] Several cases of CRRs for Cu NCs,[321–323] which are summarized in Table 7, have been reported.

In 2017, Liu, Lee, and Jiang *et al.* evaluated CRR activity using $Cu_{32}H_{20}(S_2P(O^iPr)_2)_{12}$ ($S_2P(O^iPr)_2$ = dithiophosphate ligand)[324] as an electrocatalyst.[325] From DFT calculations, they inferred a mechanism for HCOOH formation and subsequent hydride regeneration in $Cu_{32}H_{20}(S_2PH_2)_{12}$ (S_2PH_2 = dithiophosphine) (Fig. 31A and B). The two O atoms of the HCOO* intermediate bond strongly with Cu atoms on the surface to form a five-membered ring (Fig. 31B(a)). Then, HCOO* reacts to release HCOOH products (Fig. 31B(b)). The obtained $Cu_{32}H_{18}(S_2PH_2)_{12}$ with two hydride vacancies is expected to revert to $Cu_{32}H_{20}(S_2PH_2)_{12}$ *via* a proton reduction process (Fig. 31B(c and d)). To verify these theoretical predictions, electrocatalytic activity was examined by constant potential electrolysis (CPE) with $Cu_{32}H_{20}(S_2P(O^iPr)_2)_{12}$ in 0.1 M $KHCO_3$ and 0.4 M potassium chloride (KCl) solution (pH = 6.8) (Fig. 31C). From the cumulative FE of product formation after 90 min of CPE at various overvoltages, H_2, HCOOH, and CO, were detected as the main products, accounting for 90% of the FE. $Cu_{32}H_{20}(S_2P(O^iPr)_2)_{12}$ mainly produced HCOOH at low overvoltages (FE_{HCOOH} = 89% at 0.3 V *vs.* RHE). In contrast, when the overvoltage exceeded 0.5 V *vs.* RHE, H_2 was predominantly produced (FE_{H_2} = 94% at 0.6 V *vs.* RHE). These experimental results agree well with the predictions from the DFT calculations, implying that HCOOH formation occurred at low overvoltages and that HER was dominant at high overvoltages. The TOF of HCOOH formation was examined and found to
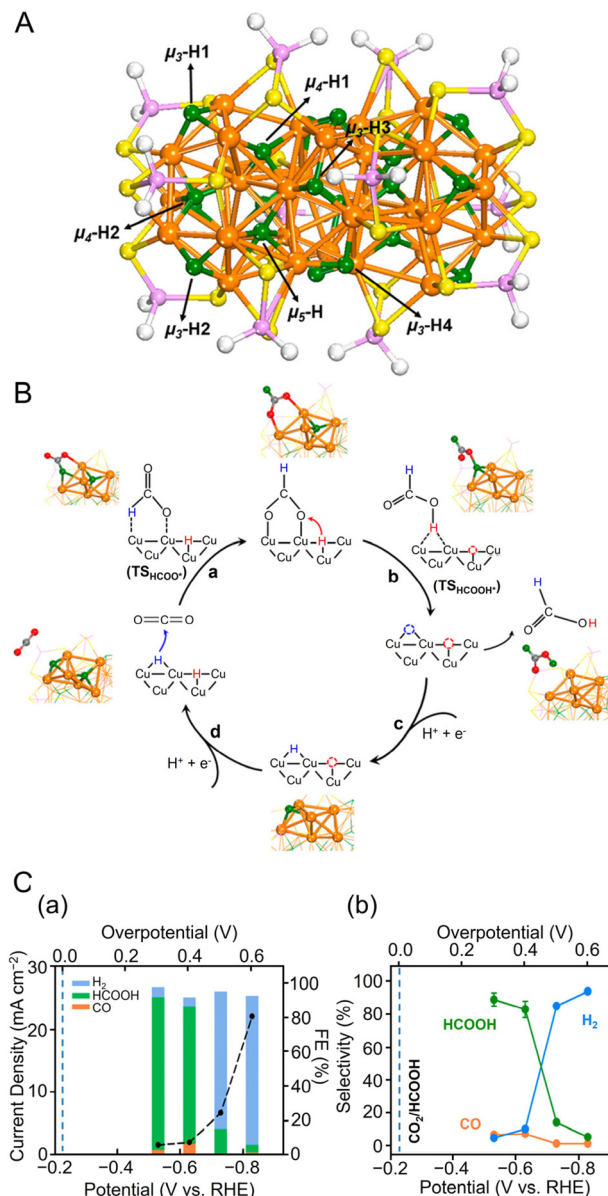

Fig. 31 (A) Geometric structure of the $Cu_{32}H_{18}(S_2PH_2)_{12}$. Color code: orange, Cu; green, hydride; yellow, S; purple, P; white, H on the dithiophosphate ligands. Different types of hydrides are indicated by the arrows. (B) (a–d) Overall mechanism of HCOOH formation from CO_2 reduction on $Cu_{32}H_{18}(S_2PH_2)_{12}$ *via* the lattice-hydride channel. (C) (a) Average current densities (black circles) and cumulative Faraday efficiencies and (b) product selectivity for H_2, HCOOH, and CO obtained at different overpotentials. Panels (A)–(C) are reproduced with permission from ref. 325. Copyright 2017 American Chemical Society.

yield 1740 mol of HCOOH per 1 mol of $Cu_{32}H_{20}(S_2P(O^iPr)_2)_{12}$ during 90 min of CPE. As a comparison, Cu NPs mainly produced CO at low overvoltages, and Cu foil mainly produced H_2 at low overvoltages. These results indicate that Cu NCs have the potential to be used as unique electrocatalysts with higher selectivity than conventional Cu NP catalysts.

In 2020, Robinson *et al.* reported the CRR activity of $Cu_{13}(MBO)_{12}$ (MBO = 2-mercaptobenzoxazole), which is com-

posed of 13 Cu atoms and 12 MBO ligands.[326] They reported that the valence of Cu atoms in $Cu_{13}(MBO)_{12}$ has an oxidation state between 0 and +1 and is highly resistant to oxidation. $Cu_{13}(MBO)_{12}$ produced 72.6% H_2, 13.2% CO, and 0.25% CH_4 as the main product at −1.04 V vs. RHE in CRR.

In 2022, Wang and Zang et al. evaluated the electrocatalytic activity of CRRs using three types of Cu_8 NCs with different cubic and tetrahedral core structures.[273] For $Cu_8(H)(L1)_6PF_6$ with a cubic core structure and $Cu_8(S^tBu)_4(L1)_4$ and $Cu_8(S^tBu)_4(L2)_4$ with tetrahedral core structures, $Cu_8(S^tBu)_4(L1)_4$ showed the highest catalytic activity, selectivity, and stability for the conversion of CO_2 to HCOOH, showing an FE_{HCOOH} of 92% at −1.0 V vs. RHE. From DFT calculations, the difference in CRR catalytic activity was attributed to the cubic form of $Cu_8(H)(L1)_6PF_6$ having an active site favorable for the competitive reaction HER, whereas the tetrahedral form of $Cu_8(S^tBu)_4(L1)_4$ had an active site favorable for the formation of *COOH in CO formation and *OOCH in formic acid for-

mation. This suggested that highly active and highly selective CRR catalysts can be created by controlling the core structure and surface morphology of Cu NCs.

Doping and ligand effects in Cu NCs have also been reported. In 2022, Ma, Song, and Wang et al. evaluated the CRR activity using $[M@Cu_{24}H_{22}(PR_3)_{12}]^+$ (M = Au or Cu; PR_3 = PPh_3 or P(p-FPh)$_3$),[275] which are protected by two phosphine ligands, as electrocatalysts.[327] $[M@Cu_{24}H_{22}(PR_3)_{12}]^+$ has a $M@Cu_{12}$ (M = Au or Cu) icosahedral kernel core, surrounded by a shell of four Cu_3P_3 units. The $M@Cu_{12}$ kernel is bonded to the Cu(ɪ) shell via a Cu–Cu metal bond. These $[M@Cu_{24}H_{22}(PR_3)_{12}]^+$ were loaded on multi-layered CNTs at 50 wt% to make CRR catalysts. From gas chromatography and ^{1}H-NMR spectroscopy, only CO, H_2, and HCOOH were observed as products. As shown in Fig. 32(a), $[Au@Cu_{24}H_{22}(PPh_3)_{12}]^+$ exhibited the highest FE_{CO} of 45.6% at −1.0 V vs. RHE, whereas $[Cu_{25}H_{22}(PPh_3)_{12}]^+$ mainly produced H_2 (FE_{H_2} > 80%). Differences in the results are due to Au doping, indicating that a single atom of Au doping can significantly change the selectivity of the CRRs. Moreover, the use of a different ligand, p-FPPh$_3$, decreased CO selectivity and increased HCOOH selectivity. As a result, for $[Au@Cu_{24}H_{22}(P(p-FPh)_3)_{12}]^+$ and $[Cu_{25}H_{22}(P(p-FPh)_3)_{12}]^+$, FE_{HCOOH} was 30.6% and 20.3%, respectively, more than three times higher than that of $[M@Cu_{24}H_{22}(PPh_3)_{12}]^+$ (Fig. 32(a)). When P(p-FPh)$_3$ was used as the ligand, similarly to PPh_3, the Au doping of one atom tended to increase the selectivity of C_1 products and decrease the selectivity of H_2 (Fig. 32(b)). The $FE_{CO+HCOOH}$ values at −0.8 V vs. RHE were 55.9%, 14.8%, 40.5%, and 20.3% for $[Au@Cu_{24}H_{22}(PPh_3)_{12}]^+$, $[Cu_{25}H_{22}(PPh_3)_{12}]^+$, $[Au@Cu_{24}H_{22}(P(p-FPh)_3)_{12}]^+$ and
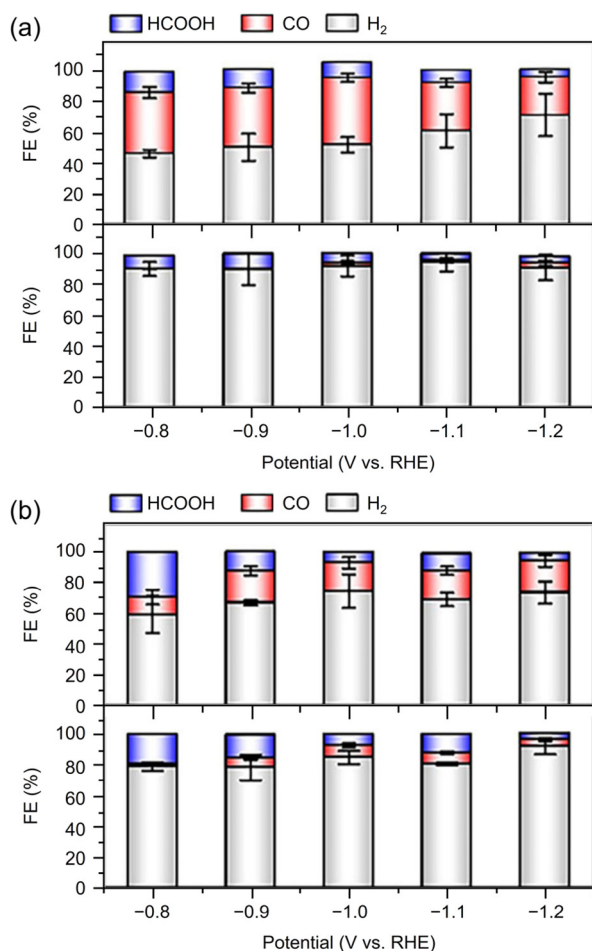
Fig. 32 Electrocatalytic performance of the four M@Cu$_{24}$ (M = Au/Cu) NCs in CRR. (a) $[M@Cu_{24}H_{22}(PPh_3)_{12}]^+$ (M = Au or Cu) and (b) $[M@Cu_{24}H_{22}(P(p-FPh)_3)_{12}]^+$ (M = Au or Cu). The error bars represent the standard deviation of three tests at the same test potential. (A) and (B) are reproduced with permission from ref. 327. Copyright 2022 Springer Nature.
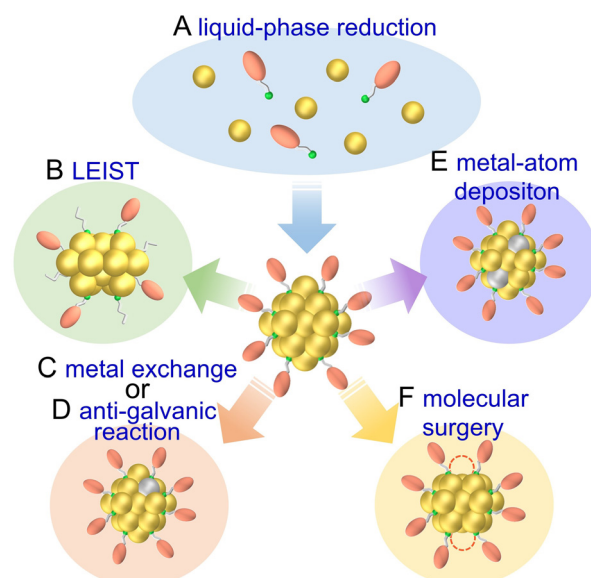
Fig. 33 Schematic of the synthesis methods of metal NCs using (A) liquid-phase reduction, (B) ligand-exchange-induced size/structure transformation (LEIST), (C) metal exchange, (D) anti-galvanic reaction, (E) metal-atom deposition, (F) molecular surgery.
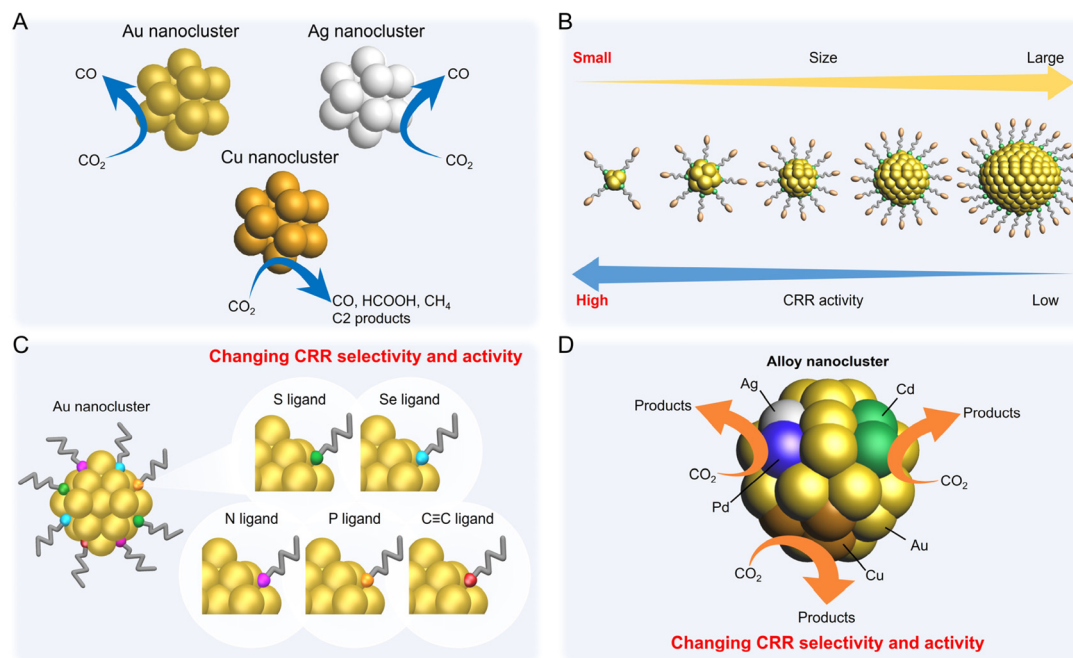
Fig. 34 Schematic of the relationship between (A) metal species, (B) size, (C) ligands, (D) alloying effect for electrocatalytic CRR performance using metal NCs.

$[Cu_{25}H_{22}(P(p\text{-}FPh)_3)_{12}]^+$, respectively (Fig. 32(b)). These results indicate that the metal core has a significant effect on the selectivity of the two competing reactions (CRR and HER) and that the type of ligand changes the selectivity of the C_1 product of CRR (HCOOH and CO). The change in selectivity may be due to the lower density of electron clouds for Cu atoms on the NC surface, caused by the electrophilic Au doping and the electrophilic ligand, $P(p\text{-}FPh)_3$. This report revealed that Au doping can reduce the selectivity of the HER in electrochemical CRRs of Cu NCs containing hydride, and the use of electrophilic ligands not only enhances the stability of Cu NCs but also promotes the selectivity of HCOOH in the CRR. Such high selectivity for HCOOH was also predicted from DFT calculations using $[Cu_{25}H_{22}(PH_3)_{12}]Cl$.[328] Furthermore, $[Cu_{26}(CF_3CO_2)_8(CH_3O)_2(C\equiv C^tBu)_4(DPPE)_3H_{11}]^+$ is also reported to be a catalyst exhibiting high CO selectivity.[329] Regarding the templated Cu NCs, $[Cu_4Ti_9O_9(BC)_{18}(O^iPr)_3(C\equiv C^tBu)(CH_3CN)]$ (BC = benzoic acid) exhibited high selectivity and good catalytic activity for the electrocatalytic reduction of CO_2 to C_2H_4 at 400 mA cm^{-2} ($FE_{C_2H_4}$: 47.6 ± 3.4%).[330]

From these reports, the CRR products of Cu NCs are often not only CO but also HCOOH, CH_4, and C2 compounds.

4. Conclusion

The conversion of CO_2 into useful compounds by electrochemical CRR is a promising strategy for achieving carbon neutrality by directly reducing CO_2 emissions. Unlike suppressing CO_2 emissions, electrochemical catalysis directly supports the sustainable development of an energy-independent society

that is considerate of the global environment. Against this background, research on electrochemical CRR has been actively studied by various groups in recent years. However, to date, most studies have focused on metal NPs with particle sizes larger than 2–3 nm. Conversely, the number of reported cases of electrocatalysts using ~1 nm metal NCs has been increasing since the 2010s and expanded rapidly around 2020 (Fig. 33). The previous studies summarized in this review have revealed the following insights into electrochemical CRRs using metal NCs (Fig. 34).

(1) Au, Ag, and Cu NCs can be synthesized as controlling the chemical composition and geometric electronic structure with atomic precision. In particular, there are many synthesis reports for Au and Ag NCs, and examples of synthesis for Cu NCs have also been reported. These can be synthesized with changing the size, geometric structure, type of ligand, and charge state (Fig. 1B).

(2) Au, Ag, and Cu NCs can be easily synthesized by a liquid-phase reduction method (Fig. 33A) in which a reducing agent is added to a solution containing metal salts and ligands.[32,35,37,38,40,41] Furthermore, metal NCs with different compositions and structures can be synthesized by the ligand exchange method (Fig. 33B) using metal NCs as precursors.[39,42,331] Moreover, these alloy NCs can also be obtained by metal exchange method[6] (Fig. 33C) or antigalvanic reaction[8] (Fig. 33D) using specific metal NCs as precursors. It is also possible to add metal atoms (Fig. 33E) by reacting with metal salts under conditions different from metal exchange.[332] There are also reports of molecular surgery (Fig. 33F), which removes some surface Au atoms while maintaining the core structure of the precursor metal NCs.[333] In these examples, it

has become possible to synthesize metal NCs using various methods. However, most of the reported examples using various synthesis methods are limited to Au NCs.

(3) In Au and Ag NCs, the primary CRR product is CO in many cases, and some have high selectivity for the HER, which is a competitive reaction (Fig. 34A).

(4) In Cu NCs and Cu-doped Au and Ag NCs, the CRR products are often not only CO but also HCOOH, CH_4, and C_2 compounds (Fig. 34A).

(5) Decreases in the size of $Au_n(SR)_m$ may promote increased CRR activity and selectivity (Fig. 34B). This is also the case with other electrocatalytic reaction systems such as HER, OER, and ORR.[120]

(6) Even in metal NCs with the same chemical composition, differences in geometric structure can cause changes in CRR activity.

(7) The CRR selectivity changes significantly depending on the type of protective ligand bound to the surface of the metal NCs (Fig. 34C).

(8) Exposure of metal atoms on metal NCs due to desorption of protective ligands may promote increased CRR activity and selectivity. DFT calculations suggest that CRR activity is associated with the desorption of organic ligands in many cases, and such desorption is presumably caused by electrochemical pretreatment or adsorption process on carbon supports.

(9) Doping of $Au_n(SR)_m$ using metal species, such as Ag and Pd, improves CRR selectivity in many cases (Fig. 34D). Such changes in activity and selectivity also depend on the doping position.

(10) Pd and Cd doping in $Au_{25}(SR)_{18}$ promote enhanced CRR activity, and Pt doping promotes enhanced HER activity in many cases (Fig. 34D).

(11) When the main CRR product is CO, the *COOH formation is the rate-determining step in many cases, and the lowering of the energy barrier is the factor of high activation.

5. Outlook

As summarized in section 4, further development of synthetic methods and evaluation of the activity of noble metal NCs may lead to highly active electrocatalysts that have not been discovered for NPs. In addition, the following initiatives are expected to be implemented in the future.

(1) Highly active and selective synthesis of useful compounds

In many reports, the main CRR products in Au, Ag, and Cu NCs is CO. CO can be used as a raw material for synthesis gas (mixture of CO and H_2), *etc.*, but it may not economically be worth considering the cost of CO_2 capture because of the price competition with CO made from fossil fuels.[75] Therefore, the development of NCs catalysts that can synthesize other useful compounds (C1 compounds such as HCOOH and CH_3OH or C2–C3 compounds) is required.[75] Although some metal NCs have been reported that can be synthesized useful compounds from CO_2,[245,254,273,325] their efficiency and selectivity is still

low, and the creation of NCs catalysts with higher activity and selectivity is required. In particular, the bond distance of atoms in Metal NCs is considered to have a great effect on the making C–C coupling to obtain C2–C3 compounds. The effect of the geometric/electronic structure of Metal NCs on the selectivity of CRR products will be further clarified, and it is expected that Metal NCs with highly selective CRR catalyst will be designed and created to obtain useful compounds.

(2) Increased durability

Without proper treatment, ligand-protected metal NCs easily agglomerate due to ligand elimination.[106] Electrochemical reduction has also been reported to desorb ligands from metal NCs, but the detailed mechanism remains unclear.[305] In addition, at present, in many cases, metal NCs are supported on a carbon black as a support having a high specific surface area, which prevents the aggregation of metal NCs even if some of the ligands are eliminated. Therefore, it has been reported that some metal NCs with stable structures have relatively high stability.[188,202,245,255,263,295,314] However, in order to improve the durability of less stable metal NCs, it is necessary to protect them by ligands with strong bonds, load metal NCs on supports with high specific surface area and high conductivity.

(3) Use of various non-precious metal nanoclusters

Precious metals are expensive and rare, and the discovery of base metals that can be substituted in metal NCs is important because it directly leads to lower costs. The use of metal NCs composed of inexpensive metal elements, such as manganese (Mn), Ni, Fe, cobalt (Co), and Cu, is expected to develop further. It has been suggested that these metal NCs may also exhibit high CRR activity due to their different electronic states from the bulk.[334–336] Especially in CRRs, Cu is expected to be a unique catalyst for obtaining various organic compounds. However, reports of Cu NCs applied in CRRs are limited. In the future, the development of highly stable Cu NCs may lead to the practical application of CO_2 recycling using electrocatalytic CRRs.

(4) Control of geometric structure of loaded nanoclusters

The true geometric/electronic structure of metal NCs after adsorption on carbon supports and after ligand desorption remains unclear. Therefore, further advancing the structural analysis/analytical techniques for loaded NCs and elucidating the desorption mechanism of ligands are necessary. If the structure of the loaded NCs is clarified, theoretical calculations using this information may provide an understanding of the reaction mechanism and reveal the key factors for high activity.

(5) Development of support and binder for metal nanoclusters

Electrocatalytic activity is also greatly affected by the support and the ionomer (such as Nafion), which functions as the binder. In the previous reports, there are few examples examining these dependencies for metal NCs. The geometric/electronic structure of metal NCs is significantly different from that of metal NPs, and support interactions and stability are also expected to be different from those of metal NPs.

Particularly, supports and binders with higher specific surface area and stronger binding to metal NCs should be developed for electrocatalytic applications. For example, metals NCs such as Au, Ag, and Cu have strong bonds with nonmetallic elements such as S, P (phosphorus), and N (nitrogen).[305] Therefore, it is expected that the stability can be improved by using a support and a binder to which these elements are included.

(6) Accurate analysis of liquid-phase CO_2 reduction reaction products

The improper evaluation of the liquid-phase components may lead to inaccurate assessments of the selectivity of the actual CRR products. For example, HCOOH produced by CRR is not identified by only analysis of gas-phase components. Furthermore, it might be present in the electrolytic solution as formate ($HCOO^-$), and appropriate quantitative analysis methods are needed. Therefore, standardized analytical methods must be developed.

(7) Verification of the products derived from CO_2

Many studies have not demonstrated that the CRR products are derived explicitly from the CO_2 that is being introduced. Therefore, it is necessary to show that the products are not derived from ligands desorbed from metal NCs or carbon supports (e.g., evaluation using the CO_2 isotope).

(8) Activity evaluation according to standards

The selectivity of CRR products varies greatly depending on the catalytic system, such as the structure of the CRR reaction cells (e.g., two-chamber cell or flow cell). Thus, standardized evaluation methods (using a standard electrolyte, Nafion membrane, counter electrode, carbon support type, etc.) are necessary for sharing and comparing data among researchers.

We hope that these issues will be overcome in the future and that efficient electrocatalysts can be developed for practical applications, which can potentially solve multiple energy and environmental problems.

Conflicts of interest

There are no conflicts to declare.

Acknowledgements

References

1 S. Hossain, D. Hirayama, A. Ikeda, M. Ishimi, S. Funaki, A. Samanta, T. Kawawaki and Y. Negishi, *Aggregate*, 2023, **4**, e255.
2 T. Higaki, Q. Li, M. Zhou, S. Zhao, Y. Li, S. Li and R. Jin, *Acc. Chem. Res.*, 2018, **51**, 2764.
3 S. Takano, S. Hasegawa, M. Suyama and T. Tsukuda, *Acc. Chem. Res.*, 2018, **51**, 3074.
4 N. A. Sakthivel and A. Dass, *Acc. Chem. Res.*, 2018, **51**, 1774.
5 B. Nieto-Ortega and T. Bürgi, *Acc. Chem. Res.*, 2018, **51**, 2811.
6 S. Wang, Q. Li, X. Kang and M. Zhu, *Acc. Chem. Res.*, 2018, **51**, 2784.
7 S. Hossain, Y. Niihori, L. V. Nair, B. Kumar, W. Kurashige and Y. Negishi, *Acc. Chem. Res.*, 2018, **51**, 3114.
8 Z. Gan, N. Xia and Z. Wu, *Acc. Chem. Res.*, 2018, **51**, 2774.
9 J. Yan, B. K. Teo and N. Zheng, *Acc. Chem. Res.*, 2018, **51**, 3084.
10 Q. Tang, G. Hu, V. Fung and D.-e. Jiang, *Acc. Chem. Res.*, 2018, **51**, 2793.
11 C. M. Aikens, *Acc. Chem. Res.*, 2018, **51**, 3065.
12 Y. Cao, T. Chen, Q. Yao and J. Xie, *Acc. Chem. Res.*, 2021, **54**, 4142.
13 M. Hesari and Z. Ding, *Acc. Chem. Res.*, 2017, **50**, 218.
14 J. F. Parker, C. A. Fields-Zinna and R. W. Murray, *Acc. Chem. Res.*, 2010, **43**, 1289.
15 K. Kwak and D. Lee, *Acc. Chem. Res.*, 2019, **52**, 12.
16 P. Chakraborty, A. Nag, A. Chakraborty and T. Pradeep, *Acc. Chem. Res.*, 2019, **52**, 2.
17 M. Agrachev, M. Ruzzi, A. Venzo and F. Maran, *Acc. Chem. Res.*, 2019, **52**, 44.
18 S. H. Yau, O. Varnavski and T. Goodson III, *Acc. Chem. Res.*, 2013, **46**, 1506.
19 A. Ghosh, O. F. Mohammed and O. M. Bakr, *Acc. Chem. Res.*, 2018, **51**, 3094.
20 T. Zhao, P. J. Herbert, H. Zheng and K. L. Knappenberger Jr., *Acc. Chem. Res.*, 2018, **51**, 1433.
21 Y. Pei, P. Wang, Z. Ma and L. Xiong, *Acc. Chem. Res.*, 2019, **52**, 23.
22 W. W. Xu, X. C. Zeng and Y. Gao, *Acc. Chem. Res.*, 2018, **51**, 2739.
23 Z. Lei, X.-K. Wan, S.-F. Yuan, Z.-J. Guan and Q.-M. Wang, *Acc. Chem. Res.*, 2018, **51**, 2465.
24 A. W. Cook and T. W. Hayton, *Acc. Chem. Res.*, 2018, **51**, 2456.
25 Q.-F. Zhang, X. Chen and L.-S. Wang, *Acc. Chem. Res.*, 2018, **51**, 2159.

26 B. Bhattarai, Y. Zaker, A. Atnagulov, B. Yoon, U. Landman and T. P. Bigioni, *Acc. Chem. Res.*, 2018, **51**, 3104.

27 S. Sharma, K. K. Chakrahari, J.-Y. Saillard and C. W. Liu, *Acc. Chem. Res.*, 2018, **51**, 2475.

28 R. L. Whetten, H.-C. Weissker, J. J. Pelayo, S. M. Mullins, X. López-Lozano and I. L. Garzón, *Acc. Chem. Res.*, 2019, **52**, 34.

29 Q. Yao, T. Chen, X. Yuan and J. Xie, *Acc. Chem. Res.*, 2018, **51**, 1338.

30 R. Jin, H. Qian, Z. Wu, Y. Zhu, M. Zhu, A. Mohanty and N. Garg, *J. Phys. Chem. Lett.*, 2010, **1**, 2903.

31 S. Jin, S. Wang and M. Zhu, *Chem. – Asian J.*, 2019, **14**, 3222.

32 Y. Jia and Z. Luo, *Coord. Chem. Rev.*, 2019, **400**, 213053.

33 S. Yamazoe and T. Tsukuda, *Bull. Chem. Soc. Jpn.*, 2019, **92**, 193.

34 E. Fernández and M. Boronat, *J. Phys.: Condens. Matter*, 2019, **31**, 013002.

35 B. Yin and Z. Luo, *Coord. Chem. Rev.*, 2021, **429**, 213643.

36 Y. Negishi, S. Hashimoto, A. Ebina, K. Hamada, S. Hossain and T. Kawawaki, *Nanoscale*, 2020, **12**, 8017.

37 T. Kawawaki, Y. Imai, D. Suzuki, S. Kato, I. Kobayashi, T. Suzuki, R. Kaneko, S. Hossain and Y. Negishi, *Chem. – Eur. J.*, 2020, **26**, 16150.

38 X. Kang, Y. Li, M. Zhu and R. Jin, *Chem. Soc. Rev.*, 2020, **49**, 6443.

39 Y. Wang and T. Bürgi, *Nanoscale Adv.*, 2021, **3**, 2710.

40 X. Kang and M. Zhu, *Chem. Mater.*, 2021, **33**, 39.

41 Y. Niihori, S. Miyajima, A. Ikeda, T. Kosaka and Y. Negishi, *Small Sci.*, 2023, **3**, 2300024.

42 X. Kang and M. Zhu, *Chem. Mater.*, 2019, **31**, 9939.

43 K. Sahoo and I. Chakraborty, *Nanoscale*, 2023, **15**, 3120.

44 Y.-e. Shi, J. Ma, A. Feng, Z. Wang and A. L. Rogach, *Aggregate*, 2021, **2**, e112.

45 H. Ma, J. Wang and X.-D. Zhang, *Coord. Chem. Rev.*, 2021, **448**, 214184.

46 M.-M. Zhang, K. Li and S.-Q. Zang, *Adv. Opt. Mater.*, 2020, **8**, 1902152.

47 X. Kang and M. Zhu, *Chem. Soc. Rev.*, 2019, **48**, 2422.

48 Y. Shichibu and K. Konishi, *ChemNanoMat*, 2022, **8**, e202200194.

49 J.-H. Huang, X.-Y. Dong, Y.-J. Wang and S.-Q. Zang, *Coord. Chem. Rev.*, 2022, **470**, 214729.

50 S. Hasegawa and T. Tsukuda, *Bull. Chem. Soc. Jpn.*, 2021, **94**, 1036.

51 T. Kawawaki, A. Ebina, Y. Hosokawa, S. Ozaki, D. Suzuki, S. Hossain and Y. Negishi, *Small*, 2021, **17**, 2005328.

52 T. Kawawaki, Y. Kataoka, M. Hirata, Y. Iwamatsu, S. Hossain and Y. Negishi, *Nanoscale Horiz.*, 2021, **6**, 409.

53 T. Imaoka and K. Yamamoto, *Bull. Chem. Soc. Jpn.*, 2019, **92**, 941.

54 C. Dong, Y. Li, D. Cheng, M. Zhang, J. Liu, Y.-G. Wang, D. Xiao and D. Ma, *ACS Catal.*, 2020, **10**, 11011.

55 Q. Zhu, X. Huang, Y. Zeng, K. Sun, L. Zhou, Y. Liu, L. Luo, S. Tian and X. Sun, *Nanoscale Adv.*, 2021, **3**, 6330.

56 R. S. Dhayal, W. E. van Zyl and C. W. Liu, *Dalton Trans.*, 2019, **48**, 3531.

57 D. Yang, J. Wang, Q. Wang, Z. Yuan, Y. Dai, C. Zhou, X. Wan, Q. Zhang and Y. Yang, *ACS Nano*, 2022, **16**, 15681.

58 T. Kawawaki, N. Shimizu, Y. Mitomi, D. Yazaki, S. Hossain and Y. Negishi, *Bull. Chem. Soc. Jpn.*, 2021, **94**, 2853.

59 Y. Niihori, K. Yoshida, S. Hossain, W. Kurashige and Y. Negishi, *Bull. Chem. Soc. Jpn.*, 2019, **92**, 664.

60 T. Kawawaki, Y. Negishi and H. Kawasaki, *Nanoscale Adv.*, 2020, **2**, 17.

61 Y. Xiao, Z. Wu, Q. Yao and J. Xie, *Aggregate*, 2021, **2**, 114.

62 W. Kurashige, Y. Niihori, S. Sharma and Y. Negishi, *Coord. Chem. Rev.*, 2016, **320–321**, 238.

63 I. Chakraborty and T. Pradeep, *Chem. Rev.*, 2017, **117**, 8208.

64 R. Jin, C. Zeng, M. Zhou and Y. Chen, *Chem. Rev.*, 2016, **116**, 10346.

65 C. Cesari, J.-H. Shon, S. Zacchini and L. A. Berben, *Chem. Soc. Rev.*, 2021, **50**, 9503.

66 M. Brust, M. Walker, D. Bethell, D. J. Schiffrin and R. Whyman, *J. Chem. Soc., Chem. Commun.*, 1994, 801.

67 R. S. Ingram, M. J. Hostetler, R. W. Murray, T. G. Schaaff, J. T. Khoury, R. L. Whetten, T. P. Bigioni, D. K. Guthrie and P. N. First, *J. Am. Chem. Soc.*, 1997, **119**, 9279.

68 T. G. Schaaff, M. N. Shafigullin, J. T. Khoury, I. Vezmar, R. L. Whetten, W. G. Cullen, P. N. First, C. Gutiérrez-Wing, J. Ascensio and M. J. Jose-Yacamán, *J. Phys. Chem. B*, 1997, **101**, 7885.

69 R. L. Whetten, J. T. Khoury, M. M. Alvarez, S. Murthy, I. Vezmar, Z. L. Wang, P. W. Stephens, C. L. Cleveland, W. D. Luedtke and U. Landman, *Adv. Mater.*, 1996, **8**, 428.

70 Y. Negishi, Y. Takasugi, S. Sato, H. Yao, K. Kimura and T. Tsukuda, *J. Am. Chem. Soc.*, 2004, **126**, 6518.

71 Y. Negishi, K. Nobusada and T. Tsukuda, *J. Am. Chem. Soc.*, 2005, **127**, 5261.

72 Y. Negishi, *Phys. Chem. Chem. Phys.*, 2022, **24**, 7569.

73 P. D. Jadzinsky, G. Calero, C. J. Ackerson, D. A. Bushnell and R. D. Kornberg, *Science*, 2007, **318**, 430.

74 S. Manabe and R. T. Wetherald, *J. Atmos. Sci.*, 1967, **24**, 241.

75 S. Nitopi, E. Bertheussen, S. B. Scott, X. Liu, A. K. Engstfeld, S. Horch, B. Seger, I. E. L. Stephens, K. Chan, C. Hahn, J. K. Nørskov, T. F. Jaramillo and I. Chorkendorff, *Chem. Rev.*, 2019, **119**, 7610.

76 G. Wang, J. Chen, Y. Ding, P. Cai, L. Yi, Y. Li, C. Tu, Y. Hou, Z. Wen and L. Dai, *Chem. Soc. Rev.*, 2021, **50**, 4993.

77 S. Rönsch, J. Schneider, S. Matthischke, M. Schlüter, M. Götz, J. Lefebvre, P. Prabhakaran and S. Bajohr, *Fuel*, 2016, **166**, 276.

78 P. Sabatier and J. B. Senderens, *C. R. Hebd. Seances Acad. Sci.*, 1902, **134**, 689.

79 R. P. Underwood and C. O. Bennett, *J. Catal.*, 1984, **86**, 245.

80 Y. Liu, Y. Li, Y. Chen, T. Qu, C. Shu, X. Yang, H. Zhu, S. Guo, S. Zhao, T. Asefa and Y. Liu, *J. Mater. Chem. A*, 2020, **8**, 8329.

81 T. E. Teeter and P. Van Rysselberghe, *J. Chem. Phys.*, 2004, **22**, 759.

82 Y. Hori, K. Kikuchi and S. Suzuki, *Chem. Lett.*, 1985, **14**, 1695.

83 Y. Hori, K. Kikuchi, A. Murata and S. Suzuki, *Chem. Lett.*, 1986, **15**, 897.

84 Y. Hori, A. Murata, R. Takahashi and S. Suzuki, *J. Chem. Soc., Chem. Commun.*, 1988, 17.

85 Y. Hori, H. Wakebe, T. Tsukamoto and O. Koga, *Electrochim. Acta*, 1994, **39**, 1833.

86 Y. Hori, A. Murata and R. Takahashi, *J. Chem. Soc., Faraday Trans. 1*, 1989, **85**, 2309.

87 S. Jin, Z. Hao, K. Zhang, Z. Yan and J. Chen, *Angew. Chem., Int. Ed.*, 2021, **60**, 20627.

88 N. Han, P. Ding, L. He, Y. Li and Y. Li, *Adv. Energy Mater.*, 2020, **10**, 1902338.

89 L. Wang, W. Chen, D. Zhang, Y. Du, R. Amal, S. Qiao, J. Wu and Z. Yin, *Chem. Soc. Rev.*, 2019, **48**, 5310.

90 Y. T. Guntern, V. Okatenko, J. Pankhurst, S. B. Varandili, P. Iyengar, C. Koolen, D. Stoian, J. Vavra and R. Buonsanti, *ACS Catal.*, 2021, **11**, 1248.

91 J. A. Trindell, Z. Duan, G. Henkelman and R. M. Crooks, *Chem. Rev.*, 2020, **120**, 814.

92 M. K. Birhanu, M.-C. Tsai, A. W. Kahsay, C.-T. Chen, T. S. Zeleke, K. B. Ibrahim, C.-J. Huang, W.-N. Su and B.-J. Hwang, *Adv. Mater. Interfaces*, 2018, **5**, 1800919.

93 Y. Cheng, S. Yang, S. P. Jiang and S. Wang, *Small Methods*, 2019, **3**, 1800440.

94 Z.-X. Wei, Y.-T. Zhu, J.-Y. Liu, Z.-C. Zhang, W.-P. Hu, H. Xu, Y.-Z. Feng and J.-M. Ma, *Rare Met.*, 2021, **40**, 767.

95 Q. Zhang and J. Guan, *Adv. Funct. Mater.*, 2020, **30**, 2000768.

96 Y.-S. Wei, M. Zhang, R. Zou and Q. Xu, *Chem. Rev.*, 2020, **120**, 12089.

97 Y. Wang, H. Su, Y. He, L. Li, S. Zhu, H. Shen, P. Xie, X. Fu, G. Zhou, C. Feng, D. Zhao, F. Xiao, X. Zhu, Y. Zeng, M. Shao, S. Chen, G. Wu, J. Zeng and C. Wang, *Chem. Rev.*, 2020, **120**, 12217.

98 J.-M. Saveant, *ChemElectroChem*, 2016, **3**, 1967.

99 L. Sun, V. Reddu, A. C. Fisher and X. Wang, *Energy Environ. Sci.*, 2020, **13**, 374.

100 A. Wagner, C. D. Sahm and E. Reisner, *Nat. Catal.*, 2020, **3**, 775.

101 Y. Du, H. Sheng, D. Astruc and M. Zhu, *Chem. Rev.*, 2020, **120**, 526.

102 T. Kawawaki, Y. Kataoka, S. Ozaki, M. Kawachi, M. Hirata and Y. Negishi, *Chem. Commun.*, 2021, **57**, 417.

103 T. Kawawaki, Y. Mori, K. Wakamatsu, S. Ozaki, M. Kawachi, S. Hossain and Y. Negishi, *J. Mater. Chem. A*, 2020, **8**, 16081.

104 D. Yazaki, T. Kawawaki, D. Hirayama, M. Kawachi, K. Kato, S. Oguchi, Y. Yamaguchi, S. Kikkawa, Y. Ueki, S. Hossain, D. J. Osborn, F. Ozaki, S. Tanaka, J. Yoshinobu, G. F. Metha, S. Yamazoe, A. Kudo, A. Yamakata and Y. Negishi, *Small*, 2023, 2208287.

105 T. Kawawaki, M. Kawachi, D. Yazaki, Y. Akinaga, D. Hirayama and Y. Negishi, *Nanomaterials*, 2022, **12**, 344.

106 T. Kawawaki, Y. Kataoka, M. Hirata, Y. Akinaga, R. Takahata, K. Wakamatsu, Y. Fujiki, M. Kataoka, S. Kikkawa, A. S. Alotabi, S. Hossain, D. J. Osborn, T. Teranishi, G. G. Andersson, G. F. Metha, S. Yamazoe and Y. Negishi, *Angew. Chem., Int. Ed.*, 2021, **60**, 21340.

107 Y. H. Li, J. Xing, Z. J. Chen, Z. Li, F. Tian, L. R. Zheng, H. F. Wang, P. Hu, H. J. Zhao and H. G. Yang, *Nat. Commun.*, 2013, **4**, 2500.

108 Q. Wu, S. Xiong, P. Shen, S. Zhao, Y. Li, D. Su and A. Orlov, *Catal. Sci. Technol.*, 2015, **5**, 2059.

109 X. L. Du, X. L. Wang, Y. H. Li, Y. L. Wang, J. J. Zhao, L. J. Fang, L. R. Zheng, H. Tong and H. G. Yang, *Chem. Commun.*, 2017, **53**, 9402.

110 C. Wang, P. Lv, D. Xue, Y. Cai, X. Yan, L. Xu, J. Fang and Y. Yang, *ACS Sustainable Chem. Eng.*, 2018, **6**, 8447.

111 L. Tian, Y. Luo, K. Chu, D. Wu, J. Shi and Z. Liang, *Chem. Commun.*, 2019, **55**, 12976.

112 C. M. Pelicano, M. Saruyama, R. Takahata, R. Sato, Y. Kitahama, H. Matsuzaki, T. Yamada, T. Hisatomi, K. Domen and T. Teranishi, *Adv. Funct. Mater.*, 2022, **32**, 2202987.

113 L. Qin, G. Ma, L. Wang and Z. Tang, *J. Energy Chem.*, 2021, **57**, 359.

114 Y. Sun, X. Cai, W. Hu, X. Liu and Y. Zhu, *Sci. China: Chem.*, 2021, **64**, 1065.

115 M. H. Naveen, R. Khan and J. H. Bang, *Chem. Mater.*, 2021, **33**, 7595.

116 T. Kawawaki and Y. Negishi, *Nanomaterials*, 2020, **10**, 238.

117 A. Dass, D. Lee and F. Maran, *ChemElectroChem*, 2016, **3**, 1191.

118 K. Kwak, W. Choi, Q. Tang, M. Kim, Y. Lee, D.-e. Jiang and D. Lee, *Nat. Commun.*, 2017, **8**, 14723.

119 G. Hu, Q. Tang, D. Lee, Z. Wu and D.-e. Jiang, *Chem. Mater.*, 2017, **29**, 4840.

120 B. Kumar, T. Kawawaki, N. Shimizu, Y. Imai, D. Suzuki, S. Hossain, L. V. Nair and Y. Negishi, *Nanoscale*, 2020, **12**, 9969.

121 D. Eguchi, M. Sakamoto and T. Teranishi, *Chem. Sci.*, 2018, **9**, 261.

122 Y. Du, J. Xiang, K. Ni, Y. Yun, G. Sun, X. Yuan, H. Sheng, Y. Zhu and M. Zhu, *Inorg. Chem. Front.*, 2018, **5**, 2948.

123 S. Zhao, R. Jin, Y. Song, H. Zhang, S. D. House, J. C. Yang and R. Jin, *Small*, 2017, **13**, 1701519.

124 X. Zhao, P. Gao, Y. Yan, X. Li, Y. Xing, H. Li, Z. Peng, J. Yang and J. Zeng, *J. Mater. Chem. A*, 2017, **5**, 20202.

125 S. Zhao, R. Jin, H. Abroshan, C. Zeng, H. Zhang, S. D. House, E. Gottlieb, H. J. Kim, J. C. Yang and R. Jin, *J. Am. Chem. Soc.*, 2017, **139**, 1077.

126 S. Funaki, T. Kawawaki, T. Okada, K. Takemae, S. Hossain, Y. Niihori, T. Naito, M. Takagi, T. Shimazaki, S. Kikkawa, S. Yamazoe, M. Tachikawa and Y. Negishi, *Nanoscale*, 2023, **15**, 5201.

127 W. Chen and S. Chen, *Angew. Chem., Int. Ed.*, 2009, **48**, 4386.

128 T. Kawawaki, N. Shimizu, K. Funai, Y. Mitomi, S. Hossain, S. Kikkawa, D. J. Osborn, S. Yamazoe, G. F. Metha and Y. Negishi, *Nanoscale*, 2021, **13**, 14679.

129 T. Kawawaki, Y. Mitomi, N. Nishi, R. Kurosaki, K. Oiwa, T. Tanaka, H. Hirase, S. Miyajima, Y. Niihori, D. J. Osborn, T. Koitaya, G. F. Metha, T. Yokoyama, K. Iida and Y. Negishi, *Nanoscale*, 2023, **15**, 7272.

130 T. Imaoka, H. Kitazawa, W.-J. Chun, S. Omura, K. Albrecht and K. Yamamoto, *J. Am. Chem. Soc.*, 2013, **135**, 13089.

131 H. Tsunoyama, A. Ohnuma, K. Takahashi, A. Velloth, M. Ehara, N. Ichikuni, M. Tabuchi and A. Nakajima, *Chem. Commun.*, 2019, **55**, 12603.

132 B. Garlyyev, K. Kratzl, M. Rück, J. Michalička, J. Fichtner, J. M. Macak, T. Kratky, S. Günther, M. Cokoja, A. S. Bandarenka, A. Gagliardi and R. A. Fischer, *Angew. Chem., Int. Ed.*, 2019, **58**, 9596.

133 H. Yin, H. Tang, D. Wang, Y. Gao and Z. Tang, *ACS Nano*, 2012, **6**, 8288.

134 Y. Lu, Y. Jiang, X. Gao and W. Chen, *Chem. Commun.*, 2014, **50**, 8464.

135 M. Zhou, C. Zeng, Y. Chen, S. Zhao, M. Y. Sfeir, M. Zhu and R. Jin, *Nat. Commun.*, 2016, **7**, 13240.

136 Y. Lu, C. Zhang, X. Li, A. R. Frojd, W. Xing, A. Z. Clayborne and W. Chen, *Nano Energy*, 2018, **50**, 316.

137 Z. Zhuang and W. Chen, *J. Colloid Interface Sci.*, 2019, **538**, 699.

138 G. Ma, L. Qin, Y. Liu, H. Fan, L. Qiao, C. Yu and Z. Tang, *Surf. Interfaces*, 2023, **36**, 102555.

139 F. Lü, H. Bao, Y. Mi, Y. Liu, J. Sun, X. Peng, Y. Qiu, L. Zhuo, X. Liu and J. Luo, *Sustainable Energy Fuels*, 2020, **4**, 1012.

140 Q. Guo, T. Lan, Z. Su, F. Zheng and W. Chen, *Mater. Rep.: Energy*, 2023, **3**, 100172.

141 L. Chen, L. Wang, Q. Shen, Y. Liu and Z. Tang, *Mater. Chem. Front.*, 2023, **7**, 1482.

142 D. Alfonso, *Catalysts*, 2022, **12**, 505.

143 A. V. Nagarajan, D. J. Loevlie, M. J. Cowan and G. Mpourmpakis, *Curr. Opin. Chem. Eng.*, 2022, **36**, 100784.

144 H. Yan, H. Xiang, J. Liu, R. Cheng, Y. Ye, Y. Han and C. Yao, *Small*, 2022, **18**, 2200812.

145 D. Yang, Y. Sun, X. Cai, W. Hu, Y. Dai, Y. Zhu and Y. Yang, *CCS Chem.*, 2021, **4**, 66.

146 C. Li, O. J. H. Chai, Q. Yao, Z. Liu, L. Wang, H. Wang and J. Xie, *Mater. Horiz.*, 2021, **8**, 1657.

147 W. Lai, Z. Ma, J. Zhang, Y. Yuan, Y. Qiao and H. Huang, *Adv. Funct. Mater.*, 2022, **32**, 2111193.

148 Z.-J. Guan, J.-J. Li, F. Hu and Q.-M. Wang, *Angew. Chem., Int. Ed.*, 2022, **61**, e202209725.

149 S. Li, W. Tian and Y. Liu, *Nanoscale*, 2021, **13**, 16847.

150 X. Cai, G. Li, W. Hu and Y. Zhu, *ACS Catal.*, 2022, **12**, 10638.

151 R. L. Donkers, D. Lee and R. W. Murray, *Langmuir*, 2004, **20**, 1945.

152 T. G. Schaaff, G. Knight, M. N. Shafigullin, R. F. Borkman and R. L. Whetten, *J. Phys. Chem. B*, 1998, **102**, 10643.

153 X. Kang, H. Chong and M. Zhu, *Nanoscale*, 2018, **10**, 10758.

154 M. Zhu, E. Lanni, N. Garg, M. E. Bier and R. Jin, *J. Am. Chem. Soc.*, 2008, **130**, 1138.

155 Z. Wu, J. Suhan and R. Jin, *J. Mater. Chem.*, 2009, **19**, 622.

156 M. Zhu, W. T. Eckenhoff, T. Pintauer and R. Jin, *J. Phys. Chem. C*, 2008, **112**, 14221.

157 M. Zhu, C. M. Aikens, M. P. Hendrich, R. Gupta, H. Qian, G. C. Schatz and R. Jin, *J. Am. Chem. Soc.*, 2009, **131**, 2490.

158 M. Zhu, C. M. Aikens, F. J. Hollander, G. C. Schatz and R. Jin, *J. Am. Chem. Soc.*, 2008, **130**, 5883.

159 M. W. Heaven, A. Dass, P. S. White, K. M. Holt and R. W. Murray, *J. Am. Chem. Soc.*, 2008, **130**, 3754.

160 S. Antonello, N. V. Perera, M. Ruzzi, J. A. Gascón and F. Maran, *J. Am. Chem. Soc.*, 2013, **135**, 15585.

161 A. Venzo, S. Antonello, J. A. Gascón, I. Guryanov, R. D. Leapman, N. V. Perera, A. Sousa, M. Zamuner, A. Zanella and F. Maran, *Anal. Chem.*, 2011, **83**, 6355.

162 G. Li, H. Abroshan, C. Liu, S. Zhuo, Z. Li, Y. Xie, H. J. Kim, N. L. Rosi and R. Jin, *ACS Nano*, 2016, **10**, 7998.

163 D.-e. Jiang and S. Dai, *Inorg. Chem.*, 2009, **48**, 2720.

164 C. Kumara, C. M. Aikens and A. Dass, *J. Phys. Chem. Lett.*, 2014, **5**, 461.

165 R. Jin, S. Zhao, C. Liu, M. Zhou, G. Panapitiya, Y. Xing, N. L. Rosi, J. P. Lewis and R. Jin, *Nanoscale*, 2017, **9**, 19183.

166 Y. Negishi, T. Iwai and M. Ide, *Chem. Commun.*, 2010, **46**, 4713.

167 J.-P. Choi, C. A. Fields-Zinna, R. L. Stiles, R. Balasubramanian, A. D. Douglas, M. C. Crowe and R. W. Murray, *J. Phys. Chem. C*, 2010, **114**, 15890.

168 W. Kurashige, K. Munakata, K. Nobusada and Y. Negishi, *Chem. Commun.*, 2013, **49**, 5447.

169 E. Gottlieb, H. Qian and R. Jin, *Chem. – Eur. J.*, 2013, **19**, 4238.

170 W. Li, C. Liu, H. Abroshan, Q. Ge, X. Yang, H. Xu and G. Li, *J. Phys. Chem. C*, 2016, **120**, 10261.

171 Y. Negishi, K. Munakata, W. Ohgake and K. Nobusada, *J. Phys. Chem. Lett.*, 2012, **3**, 2209.

172 S. Yamazoe, W. Kurashige, K. Nobusada, Y. Negishi and T. Tsukuda, *J. Phys. Chem. C*, 2014, **118**, 25284.

173 S. Hossain, D. Suzuki, T. Iwasa, R. Kaneko, T. Suzuki, S. Miyajima, Y. Iwamatsu, S. Pollitt, T. Kawawaki, N. Barrabés, G. Rupprechter and Y. Negishi, *J. Phys. Chem. C*, 2020, **124**, 22304.

174 H. Qian, D.-e. Jiang, G. Li, C. Gayathri, A. Das, R. R. Gil and R. Jin, *J. Am. Chem. Soc.*, 2012, **134**, 16159.

175 S. Tian, L. Liao, J. Yuan, C. Yao, J. Chen, J. Yang and Z. Wu, *Chem. Commun.*, 2016, **52**, 9873.

176 M. Suyama, S. Takano, T. Nakamura and T. Tsukuda, *J. Am. Chem. Soc.*, 2019, **141**, 14048.

177 S. Hossain, Y. Imai, D. Suzuki, W. Choi, Z. Chen, T. Suzuki, M. Yoshioka, T. Kawawaki, D. Lee and Y. Negishi, *Nanoscale*, 2019, **11**, 22089.

178 S. Xie, H. Tsunoyama, W. Kurashige, Y. Negishi and T. Tsukuda, *ACS Catal.*, 2012, **2**, 1519.

179 C. A. Fields-Zinna, M. C. Crowe, A. Dass, J. E. F. Weaver and R. W. Murray, *Langmuir*, 2009, **25**, 7704.

180 Y. Negishi, W. Kurashige, Y. Niihori, T. Iwasa and K. Nobusada, *Phys. Chem. Chem. Phys.*, 2010, **12**, 6219.

181 M. A. Tofanelli, T. W. Ni, B. D. Phillips and C. J. Ackerson, *Inorg. Chem.*, 2016, **55**, 999.

182 L. Liao, S. Zhou, Y. Dai, L. Liu, C. Yao, C. Fu, J. Yang and Z. Wu, *J. Am. Chem. Soc.*, 2015, **137**, 9511.

183 W. Fei, S. Antonello, T. Dainese, A. Dolmella, M. Lahtinen, K. Rissanen, A. Venzo and F. Maran, *J. Am. Chem. Soc.*, 2019, **141**, 16033.

184 S. Wang, Y. Song, S. Jin, X. Liu, J. Zhang, Y. Pei, X. Meng, M. Chen, P. Li and M. Zhu, *J. Am. Chem. Soc.*, 2015, **137**, 4018.

185 C. Yao, Y.-j. Lin, J. Yuan, L. Liao, M. Zhu, L.-h. Weng, J. Yang and Z. Wu, *J. Am. Chem. Soc.*, 2015, **137**, 15350.

186 S. Bhat, A. Baksi, S. K. Mudedla, G. Natarajan, V. Subramanian and T. Pradeep, *J. Phys. Chem. Lett.*, 2017, **8**, 2787.

187 K. Kwak, Q. Tang, M. Kim, D.-e. Jiang and D. Lee, *J. Am. Chem. Soc.*, 2015, **137**, 10833.

188 Y. Sun, X. Liu, K. Xiao, Y. Zhu and M. Chen, *ACS Catal.*, 2021, **11**, 11551.

189 Q. Li, S. Wang, K. Kirschbaum, K. J. Lambright, A. Das and R. Jin, *Chem. Commun.*, 2016, **52**, 5194.

190 H. Seong, M. Choi, S. Park, H.-w. Kim, J. Kim, W. Kim, J. S. Yoo and D. Lee, *ACS Energy Lett.*, 2022, **7**, 4177.

191 C. P. Joshi, M. S. Bootharaju, M. J. Alhilaly and O. M. Bakr, *J. Am. Chem. Soc.*, 2015, **137**, 11578.

192 J.-W. Yuan, M.-M. Zhang, X.-Y. Dong and S.-Q. Zang, *Nanoscale*, 2022, **14**, 1538.

193 H. Qian, W. T. Eckenhoff, Y. Zhu, T. Pintauer and R. Jin, *J. Am. Chem. Soc.*, 2010, **132**, 8280.

194 H. Qian, Y. Zhu and R. Jin, *ACS Nano*, 2009, **3**, 3795.

195 S. Tian, Y.-Z. Li, M.-B. Li, J. Yuan, J. Yang, Z. Wu and R. Jin, *Nat. Commun.*, 2015, **6**, 8667.

196 I. Dolamic, S. Knoppe, A. Dass and T. Bürgi, *Nat. Commun.*, 2012, **3**, 798.

197 I. Dolamic, B. Varnholt and T. Bürgi, *Nat. Commun.*, 2015, **6**, 7117.

198 N. Barrabés, B. Zhang and T. Bürgi, *J. Am. Chem. Soc.*, 2014, **136**, 14361.

199 X. Liu, E. Wang, M. Zhou, Y. Wan, Y. Zhang, H. Liu, Y. Zhao, J. Li, Y. Gao and Y. Zhu, *Angew. Chem., Int. Ed.*, 2022, **61**, e202207685.

200 M. Kim, Q. Tang, A. V. N. Kumar, K. Kwak, W. Choi, D.-e. Jiang and D. Lee, *J. Phys. Chem. Lett.*, 2018, **9**, 982.

201 E. Ito, S. Takano, T. Nakamura and T. Tsukuda, *Angew. Chem., Int. Ed.*, 2021, **60**, 645.

202 S. Zhuang, D. Chen, W. Fan, J. Yuan, L. Liao, Y. Zhao, J. Li, H. Deng, J. Yang, J. Yang and Z. Wu, *Nano Lett.*, 2022, **22**, 7144.

203 S. Chen, S. Wang, J. Zhong, Y. Song, J. Zhang, H. Sheng, Y. Pei and M. Zhu, *Angew. Chem., Int. Ed.*, 2015, **54**, 3145.

204 C. Zeng, C. Liu, Y. Chen, N. L. Rosi and R. Jin, *J. Am. Chem. Soc.*, 2014, **136**, 11922.

205 L. Xiong, S. Yang, X. Sun, J. Chai, B. Rao, L. Yi, M. Zhu and Y. Pei, *J. Phys. Chem. C*, 2018, **122**, 14898.

206 A. Das, T. Li, K. Nobusada, C. Zeng, N. L. Rosi and R. Jin, *J. Am. Chem. Soc.*, 2013, **135**, 18264.

207 A. Das, T. Li, G. Li, K. Nobusada, C. Zeng, N. L. Rosi and R. Jin, *Nanoscale*, 2014, **6**, 6458.

208 C. Zeng, T. Li, A. Das, N. L. Rosi and R. Jin, *J. Am. Chem. Soc.*, 2013, **135**, 10011.

209 D. Crasto, S. Malola, G. Brosofsky, A. Dass and H. Häkkinen, *J. Am. Chem. Soc.*, 2014, **136**, 5000.

210 C. Zeng, H. Qian, T. Li, G. Li, N. L. Rosi, B. Yoon, R. N. Barnett, R. L. Whetten, U. Landman and R. Jin, *Angew. Chem., Int. Ed.*, 2012, **51**, 13114.

211 C. Zeng, Y. Chen, K. Iida, K. Nobusada, K. Kirschbaum, K. J. Lambright and R. Jin, *J. Am. Chem. Soc.*, 2016, **138**, 3950.

212 C. Zeng, Y. Chen, C. Liu, K. Nobusada, N. L. Rosi and R. Jin, *Sci. Adv.*, 2015, **1**, e1500425.

213 C. Zeng, C. Liu, Y. Chen, N. L. Rosi and R. Jin, *J. Am. Chem. Soc.*, 2016, **138**, 8710.

214 Y. Chen, C. Zeng, C. Liu, K. Kirschbaum, C. Gayathri, R. R. Gil, N. L. Rosi and R. Jin, *J. Am. Chem. Soc.*, 2015, **137**, 10076.

215 H. Qian and R. Jin, *Nano Lett.*, 2009, **9**, 4083.

216 N. Yan, N. Xia, L. Liao, M. Zhu, F. Jin, R. Jin and Z. Wu, *Sci. Adv.*, 2018, **4**, eaat7259.

217 K. Kwak, V. D. Thanthirige, K. Pyo, D. Lee and G. Ramakrishna, *J. Phys. Chem. Lett.*, 2017, **8**, 4898.

218 K. Konishi, in *Gold Clusters, Colloids and Nanoparticles I*, ed. D. M. P. Mingos, Springer International Publishing, Cham, 2014, p. 49.

219 R. H. Adnan, J. M. L. Madridejos, A. S. Alotabi, G. F. Metha and G. G. Andersson, *Adv. Sci.*, 2022, **9**, 2105692.

220 K. Konishi, M. Iwasaki and Y. Shichibu, *Acc. Chem. Res.*, 2018, **51**, 3125.

221 X.-K. Wan, Z.-W. Lin and Q.-M. Wang, *J. Am. Chem. Soc.*, 2012, **134**, 14750.

222 J. Chen, Q.-F. Zhang, P. G. Williard and L.-S. Wang, *Inorg. Chem.*, 2014, **53**, 3932.

223 M. McPartlin, R. Mason and L. Malatesta, *J. Chem. Soc. D*, 1969, 334.

224 J. W. A. van der Velden, F. A. Vollenbroek, J. J. Bour, P. T. Beurskens, J. M. M. Smits and W. P. Bosnian, *Recl. Trav. Chim. Pays-Bas*, 1981, **100**, 148.

225 F. A. Vollenbroek, J. J. Bour and J. W. A. van der Veden, *Recl. Trav. Chim. Pays-Bas*, 1980, **99**, 137.

226 F. A. Vollenbroek, W. P. Bosman, J. J. Bour, J. H. Noordik and P. T. Beurskens, *J. Chem. Soc., Chem. Commun.*, 1979, 387.

227 K. P. Hall and D. M. P. Mingos, *Prog. Inorg. Chem.*, 1984, **32**, 237.

228 C. E. Briant, B. R. C. Theobald, J. W. White, L. K. Bell, D. M. P. Mingos and A. J. Welch, *J. Chem. Soc., Chem. Commun.*, 1981, 201.

229 K. P. Hall, B. R. C. Theoblad, D. I. Gilmour, D. M. P. Mingos and A. J. Welch, *J. Chem. Soc., Chem. Commun.*, 1982, 528.

230 Y. Shichibu and K. Konishi, *Small*, 2010, **6**, 1216.

231 Z.-H. Gao, K. Wei, T. Wu, J. Dong, D.-e. Jiang, S. Sun and L.-S. Wang, *J. Am. Chem. Soc.*, 2022, **144**, 5258.

232 L. Tang, Y. Luo, X. Ma, B. Wang, M. Ding, R. Wang, P. Wang, Y. Pei and S. Wang, *Angew. Chem., Int. Ed.*, 2023, **62**, e202300553.

233 X.-K. Wan, J.-Q. Wang and Q.-M. Wang, *Angew. Chem., Int. Ed.*, 2021, **60**, 20748.

234 X. Ma, Y. Tang, G. Ma, L. Qin and Z. Tang, *Nanoscale*, 2021, **13**, 602.

235 Z. Lei, X.-K. Wan, S.-F. Yuan, J.-Q. Wang and Q.-M. Wang, *Dalton Trans.*, 2017, **46**, 3427.

236 M.-M. Zhang, X.-Y. Dong, Y.-J. Wang, S.-Q. Zang and T. C. W. Mak, *Coord. Chem. Rev.*, 2022, **453**, 214315.

237 Z. Lei, M. Endo, H. Ube, T. Shiraogawa, P. Zhao, K. Nagata, X.-L. Pei, T. Eguchi, T. Kamachi, M. Ehara, T. Ozawa and M. Shionoya, *Nat. Commun.*, 2022, **13**, 4288.

238 M. R. Narouz, K. M. Osten, P. J. Unsworth, R. W. Y. Man, K. Salorinne, S. Takano, R. Tomihara, S. Kaappa, S. Malola, C.-T. Dinh, J. D. Padmos, K. Ayoo, P. J. Garrett, M. Nambo, J. H. Horton, E. H. Sargent, H. Häkkinen, T. Tsukuda and C. M. Crudden, *Nat. Chem.*, 2019, **11**, 419.

239 Z. Lei, X.-L. Pei, H. Ube and M. Shionoya, *Bull. Chem. Soc. Jpn.*, 2021, **94**, 1324.

240 P. Luo, S. Bai, X. Wang, J. Zhao, Z.-N. Yan, Y.-F. Han, S.-Q. Zang and T. C. W. Mak, *Adv. Opt. Mater.*, 2021, **9**, 2001936.

241 H. Shen, S. Xiang, Z. Xu, C. Liu, X. Li, C. Sun, S. Lin, B. K. Teo and N. Zheng, *Nano Res.*, 2020, **13**, 1908.

242 S.-F. Yuan, W.-D. Liu, C.-Y. Liu, Z.-J. Guan and Q.-M. Wang, *Chem. – Eur. J.*, 2022, **28**, e202104445.

243 Y. Wang, X.-K. Wan, L. Ren, H. Su, G. Li, S. Malola, S. Lin, Z. Tang, H. Häkkinen, B. K. Teo, Q.-M. Wang and N. Zheng, *J. Am. Chem. Soc.*, 2016, **138**, 3278.

244 X. Ma, L. Xiong, L. Qin, Y. Tang, G. Ma, Y. Pei and Z. Tang, *Chem. Sci.*, 2021, **12**, 12819.

245 X. Ma, F. Sun, L. Qin, Y. Liu, X. Kang, L. Wang, D.-e. Jiang, Q. Tang and Z. Tang, *Chem. Sci.*, 2022, **13**, 10149.

246 P. de Frémont, N. Marion and S. P. Nolan, *J. Organomet. Chem.*, 2009, **694**, 551.

247 P. de Frémont, N. M. Scott, E. D. Stevens and S. P. Nolan, *Organometallics*, 2005, **24**, 2411.

248 S. Orbisaglia, B. Jacques, P. Braunstein, D. Hueber, P. Pale, A. Blanc and P. de Frémont, *Organometallics*, 2013, **32**, 4153.

249 V. K. Kulkarni, B. N. Khiarak, S. Takano, S. Malola, E. L. Albright, T. I. Levchenko, M. D. Aloisio, C.-T. Dinh, T. Tsukuda, H. Häkkinen and C. M. Crudden, *J. Am. Chem. Soc.*, 2022, **144**, 9000.

250 S.-F. Yuan, R.-L. He, X.-S. Han, J.-Q. Wang, Z.-J. Guan and Q.-M. Wang, *Angew. Chem., Int. Ed.*, 2021, **60**, 14345.

251 H. Yang, Y. Wang, H. Huang, L. Gell, L. Lehtovaara, S. Malola, H. Häkkinen and N. Zheng, *Nat. Commun.*, 2013, **4**, 2422.

252 A. Desireddy, B. E. Conn, J. Guo, B. Yoon, R. N. Barnett, B. M. Monahan, K. Kirschbaum, W. P. Griffith, R. L. Whetten, U. Landman and T. P. Bigioni, *Nature*, 2013, **501**, 399.

253 Y. Song, K. Lambright, M. Zhou, K. Kirschbaum, J. Xiang, A. Xia, M. Zhu and R. Jin, *ACS Nano*, 2018, **12**, 9318.

254 J. Zha, X. Meng, W. Fan, Q. You, N. Xia, W. Gu, Y. Zhao, L. Hu, J. Li, H. Deng, H. Wang, N. Yan and Z. Wu, *ACS Appl. Mater. Interfaces*, 2023, **15**, 3985.

255 X. Lin, W. Ma, K. Sun, B. Sun, X. Fu, X. Ren, C. Liu and J. Huang, *J. Phys. Chem. Lett.*, 2021, **12**, 552.

256 X.-H. Ma, Y. Si, L.-L. Luo, Z.-Y. Wang, S.-Q. Zang and T. C. W. Mak, *ACS Nano*, 2022, **16**, 5507.

257 M. Qu, H. Li, L.-H. Xie, S.-T. Yan, J.-R. Li, J.-H. Wang, C.-Y. Wei, Y.-W. Wu and X.-M. Zhang, *J. Am. Chem. Soc.*, 2017, **139**, 12346.

258 L. Qin, F. Sun, X. Ma, G. Ma, Y. Tang, L. Wang, Q. Tang, R. Jin and Z. Tang, *Angew. Chem., Int. Ed.*, 2021, **60**, 26136.

259 X. Ma, G. Ma, L. Qin, G. Chen, S. Chen and Z. Tang, *Sci. China: Chem.*, 2020, **63**, 1777.

260 L. Chen, F. Sun, Q. Shen, L. Qin, Y. Liu, L. Qiao, Q. Tang, L. Wang and Z. Tang, *Nano Res.*, 2022, **15**, 8908.

261 Y. Wang, H. Su, L. Ren, S. Malola, S. Lin, B. K. Teo, H. Häkkinen and N. Zheng, *Angew. Chem., Int. Ed.*, 2016, **55**, 15152.

262 H. Shen and T. Mizuta, *Chem. – Eur. J.*, 2017, **23**, 17885.

263 G. Deng, J. Kim, M. S. Bootharaju, F. Sun, K. Lee, Q. Tang, Y. J. Hwang and T. Hyeon, *J. Am. Chem. Soc.*, 2023, **145**, 3401.

264 Y. Horita, M. Ishimi and Y. Negishi, *Sci. Technol. Adv. Mater.*, 2023, 2203832.

265 R. Ge, X.-X. Li and S.-T. Zheng, *Coord. Chem. Rev.*, 2021, **435**, 213787.

266 S.-Q. Li, L.-F. Dai, Y.-Q. Tian, Y.-X. Yi, J. Yan and C. Liu, *Chem. Commun.*, 2023, **59**, 575.

267 C. Sun, B. K. Teo, C. Deng, J. Lin, G.-G. Luo, C.-H. Tung and D. Sun, *Coord. Chem. Rev.*, 2021, **427**, 213576.

268 K. K. Chakrahari, J.-H. Liao, S. Kahlal, Y.-C. Liu, M.-H. Chiang, J.-Y. Saillard and C. W. Liu, *Angew. Chem., Int. Ed.*, 2016, **55**, 14704.

269 A. J. Edwards, R. S. Dhayal, P.-K. Liao, J.-H. Liao, M.-H. Chiang, R. O. Piltz, S. Kahlal, J.-Y. Saillard and C. W. Liu, *Angew. Chem., Int. Ed.*, 2014, **53**, 7214.

270 R. P. B. Silalahi, K. K. Chakrahari, J.-H. Liao, S. Kahlal, Y.-C. Liu, M.-H. Chiang, J.-Y. Saillard and C. W. Liu, *Chem. – Asian J.*, 2018, **13**, 500.

271 A. Baghdasaryan and T. Bürgi, *Nanoscale*, 2021, **13**, 6283.

272 P.-K. Liao, B. Sarkar, H.-W. Chang, J.-C. Wang and C. W. Liu, *Inorg. Chem.*, 2009, **48**, 4089.

273 L.-J. Liu, Z.-Y. Wang, Z.-Y. Wang, R. Wang, S.-Q. Zang and T. C. W. Mak, *Angew. Chem., Int. Ed.*, 2022, **61**, e202205626.

274 T.-A. D. Nguyen, Z. R. Jones, B. R. Goldsmith, W. R. Buratto, G. Wu, S. L. Scott and T. W. Hayton, *J. Am. Chem. Soc.*, 2015, **137**, 13319.

275 A. Chen, X. Kang, S. Jin, W. Du, S. Wang and M. Zhu, *J. Phys. Chem. Lett.*, 2019, **10**, 6124.

276 B.-L. Han, Z. Liu, L. Feng, Z. Wang, R. K. Gupta, C. M. Aikens, C.-H. Tung and D. Sun, *J. Am. Chem. Soc.*, 2020, **142**, 5834.

277 X.-K. Wan, X.-L. Cheng, Q. Tang, Y.-Z. Han, G. Hu, D.-e. Jiang and Q.-M. Wang, *J. Am. Chem. Soc.*, 2017, **139**, 9451.

278 P. Sabatier, *Ber. Dtsch. Chem. Ges.*, 1911, **44**, 1984.

279 Z. W. Seh, J. Kibsgaard, C. F. Dickens, I. Chorkendorff, J. K. Nørskov and T. F. Jaramillo, *Science*, 2017, **355**, eaad4998.

280 H. Häkkinen, *Chem. Soc. Rev.*, 2008, **37**, 1847.

281 V. R. Jupally, R. Kota, E. V. Dornshuld, D. L. Mattern, G. S. Tschumper, D.-e. Jiang and A. Dass, *J. Am. Chem. Soc.*, 2011, **133**, 20258.

282 Y. Gao, N. Shao, Y. Pei, Z. Chen and X. C. Zeng, *ACS Nano*, 2011, **5**, 7818.

283 O. Lopez-Acevedo, K. A. Kacprzak, J. Akola and H. Häkkinen, *Nat. Chem.*, 2010, **2**, 329.

284 C. M. Aikens, *J. Phys. Chem. Lett.*, 2010, **1**, 2594.

285 J. F. Parker, K. A. Kacprzak, O. Lopez-Acevedo, H. Häkkinen and R. W. Murray, *J. Phys. Chem. C*, 2010, **114**, 8276.

286 C. M. Aikens, *J. Phys. Chem. C*, 2008, **112**, 19797.

287 Y. Pei, R. Pal, C. Liu, Y. Gao, Z. Zhang and X. C. Zeng, *J. Am. Chem. Soc.*, 2012, **134**, 3015.

288 J. W. Vickers, D. Alfonso and D. R. Kauffman, *Energy Technol.*, 2017, **5**, 775.

289 C. Kim, F. Dionigi, V. Beermann, X. Wang, T. Möller and P. Strasser, *Adv. Mater.*, 2019, **31**, 1805617.

290 A. A. Peterson and J. K. Nørskov, *J. Phys. Chem. Lett.*, 2012, **3**, 251.

291 D. R. Kauffman, D. Alfonso, C. Matranga, H. Qian and R. Jin, *J. Am. Chem. Soc.*, 2012, **134**, 10237.

292 D. R. Kauffman, D. Alfonso, C. Matranga, P. Ohodnicki, X. Deng, R. C. Siva, C. Zeng and R. Jin, *Chem. Sci.*, 2014, **5**, 3151.

293 D. R. Kauffman, J. Thakkar, R. Siva, C. Matranga, P. R. Ohodnicki, C. Zeng and R. Jin, *ACS Appl. Mater. Interfaces*, 2015, **7**, 15626.

294 V. R. Jupally, A. C. Dharmaratne, D. Crasto, A. J. Huckaba, C. Kumara, P. R. Nimmala, N. Kothalawala, J. H. Delcamp and A. Dass, *Chem. Commun.*, 2014, **50**, 9895.

295 H. Seong, V. Efremov, G. Park, H. Kim, J. S. Yoo and D. Lee, *Angew. Chem., Int. Ed.*, 2021, **60**, 14563.

296 S. Li, A. V. Nagarajan, X. Du, Y. Li, Z. Liu, D. R. Kauffman, G. Mpourmpakis and R. Jin, *Angew. Chem., Int. Ed.*, 2022, **61**, e202211771.

297 S. K. Sharma, H. T. Ahangari, B. Johannessen, V. B. Golovko and A. T. Marshall, *Electrocatalysis*, 2023, **14**, 611.

298 C. Zhang, M. Ding, Y. Ren, A. Ma, Z. Yin, X. Ma and S. Wang, *Nanoscale Adv.*, 2023, **5**, 3287.

299 S. Zhao, N. Austin, M. Li, Y. Song, S. D. House, S. Bernhard, J. C. Yang, G. Mpourmpakis and R. Jin, *ACS Catal.*, 2018, **8**, 4996.

300 S. Zhuang, D. Chen, W.-P. Ng, L.-J. Liu, M.-Y. Sun, D. Liu, T. Nawaz, Q. Xia, X. Wu, Y.-L. Huang, S. Lee, J. Yang, J. Yang and J. He, *Angew. Chem., Int. Ed.*, 2023, **62**, e202306696.

301 S. Li, A. V. Nagarajan, Y. Li, D. R. Kauffman, G. Mpourmpakis and R. Jin, *Nanoscale*, 2021, **13**, 2333.

302 J. Wang, Z.-Y. Wang, S.-J. Li, S.-Q. Zang and T. C. W. Mak, *Angew. Chem., Int. Ed.*, 2021, **60**, 5959.

303 J. Wang, F. Xu, Z.-Y. Wang, S.-Q. Zang and T. C. W. Mak, *Angew. Chem., Int. Ed.*, 2022, **61**, e202207492.

304 M. R. Narouz, S. Takano, P. A. Lummis, T. I. Levchenko, A. Nazemi, S. Kaappa, S. Malola, G. Yousefalizadeh, L. A. Calhoun, K. G. Stamplecoskie, H. Häkkinen, T. Tsukuda and C. M. Crudden, *J. Am. Chem. Soc.*, 2019, **141**, 14997.

305 S. Chen, M. Li, S. Yu, S. Louisia, W. Chuang, M. Gao, C. Chen, J. Jin, M. B. Salmeron and P. Yang, *J. Chem. Phys.*, 2021, **155**, 051101.

306 S. Zhuang, D. Chen, L. Liao, Y. Zhao, N. Xia, W. Zhang, C. Wang, J. Yang and Z. Wu, *Angew. Chem., Int. Ed.*, 2020, **59**, 3073.

307 Q. Li, K. J. Lambright, M. G. Taylor, K. Kirschbaum, T.-Y. Luo, J. Zhao, G. Mpourmpakis, S. Mokashi-Punekar, N. L. Rosi and R. Jin, *J. Am. Chem. Soc.*, 2017, **139**, 17779.

308 S. Li, A. V. Nagarajan, D. R. Alfonso, M. Sun, D. R. Kauffman, G. Mpourmpakis and R. Jin, *Angew. Chem., Int. Ed.*, 2021, **60**, 6351.

309 W. Choi, H. Seong, V. Efremov, Y. Lee, S. Im, D.-H. Lim, J. S. Yoo and D. Lee, *J. Chem. Phys.*, 2021, **155**, 014305.

310 S. Tang, J. Xu, X. Liu and Y. Zhu, *Chem. – Eur. J.*, 2022, **28**, e202201262.

311 S. Li, D. Alfonso, A. V. Nagarajan, S. D. House, J. C. Yang, D. R. Kauffman, G. Mpourmpakis and R. Jin, *ACS Catal.*, 2020, **10**, 12011.

312 E. Andrews, S. Katla, C. Kumar, M. Patterson, P. Sprunger and J. Flake, *J. Electrochem. Soc.*, 2015, **162**, F1373.

313 B. Kim, H. Seong, J. T. Song, K. Kwak, H. Song, Y. C. Tan, G. Park, D. Lee and J. Oh, *ACS Energy Lett.*, 2020, **5**, 749.

314 M. de Jesus Gálvez-Vázquez, P. Moreno-García, H. Xu, Y. Hou, H. Hu, I. Z. Montiel, A. V. Rudnev, S. Alinejad, V. Grozovski, B. J. Wiley, M. Arenz and P. Broekmann, *ACS Catal.*, 2020, **10**, 13096.

315 J. Xu, L. Xiong, X. Cai, S. Tang, A. Tang, X. Liu, Y. Pei and Y. Zhu, *Chem. Sci.*, 2022, **13**, 2778.

316 J. Hu, M. Zhou, K. Li, A. Yao, Y. Wang, Q. Zhu, Y. Zhou, L. Huang, Y. Pei, Y. Du, S. Jin and M. Zhu, *Small*, 2023, 2301357.

317 X.-K. Wan, J.-Q. Wang, Z.-A. Nan and Q.-M. Wang, *Sci. Adv.*, 2017, **3**, e1701823.

318 X. Li, S. Takano and T. Tsukuda, *J. Phys. Chem. C*, 2021, **125**, 23226.

319 T. K. Todorova, M. W. Schreiber and M. Fontecave, *ACS Catal.*, 2020, **10**, 1754.

320 L. L.-M. Zhang and W.-Y. Wong, *Aggregate*, 2023, **4**, e266.

321 B. Das, M. Bhadbhade, A. Thapper, C. D. Ling and S. B. Colbran, *Dalton Trans.*, 2019, **48**, 3576.

322 Y.-F. Bu, M. Zhao, G.-X. Zhang, X. Zhang, W. Gao and Q. Jiang, *ChemElectroChem*, 2019, **6**, 1831.

323 A. A. B. Padama, J. D. Ocon, H. Nakanishi and H. Kasai, *J. Phys.: Condens. Matter*, 2019, **31**, 415201.

324 R. S. Dhayal, J.-H. Liao, S. Kahlal, X. Wang, Y.-C. Liu, M.-H. Chiang, W. E. van Zyl, J.-Y. Saillard and C. W. Liu, *Chem. – Eur. J.*, 2015, **21**, 8369.

325 Q. Tang, Y. Lee, D.-Y. Li, W. Choi, C. W. Liu, D. Lee and D.-e. Jiang, *J. Am. Chem. Soc.*, 2017, **139**, 9728.

326 H. Han, Y. Yao, A. Bhargava, Z. Wei, Z. Tang, J. Suntivich, O. Voznyy and R. D. Robinson, *J. Am. Chem. Soc.*, 2020, **142**, 14495.

327 M. Ding, L. Tang, X. Ma, C. Song and S. Wang, *Commun. Chem.*, 2022, **5**, 172.

328 F. Li and Q. Tang, *J. Catal.*, 2020, **387**, 95.

329 S. Li, X. Yan, J. Tang, D. Cao, X. Sun, G. Tian, X. Tang, H. Guo, Q. Wu, J. Sun, J. He and H. Shen, *Chem. Mater.*, 2023, **35**, 6123.

330 X. Fan, J. Cheng, M. Qiu, Y. Zhang, S. Chen, Z. Zhang, Y. Peng, J. Zhang and L. Zhang, *ACS Mater. Lett.*, 2023, **5**, 1527.

331 C. Zeng, Y. Chen, A. Das and R. Jin, *J. Phys. Chem. Lett.*, 2015, **6**, 2976.

332 C. Yao, J. Chen, M.-B. Li, L. Liu, J. Yang and Z. Wu, *Nano Lett.*, 2015, **15**, 1281.

333 Q. Li, T.-Y. Luo, M. G. Taylor, S. Wang, X. Zhu, Y. Song, G. Mpourmpakis, N. L. Rosi and R. Jin, *Sci. Adv.*, 2017, **3**, e1603193.

334 S.-Y. Wu and H.-T. Chen, *ACS Appl. Energy Mater.*, 2019, **2**, 1544.

335 C. Liu, H. He, P. Zapol and L. A. Curtiss, *Phys. Chem. Chem. Phys.*, 2014, **16**, 26584.

336 R. K. Raju, P. Rodriguez and E. N. Brothers, *Phys. Chem. Chem. Phys.*, 2023, **25**, 11630.